

# AN ANALYSIS OF RADIO-FREQUENCY GEOLOCATION TECHNIQUES FOR SATELLITE SYSTEMS DESIGN

#### THESIS

Daniel R. Barnes, 2d Lt, USAF AFIT-ENY-MS-17-M-241

# DEPARTMENT OF THE AIR FORCE AIR UNIVERSITY

# AIR FORCE INSTITUTE OF TECHNOLOGY

Wright-Patterson Air Force Base, Ohio



# AN ANALYSIS OF RADIO-FREQUENCY GEOLOCATION TECHNIQUES FOR SATELLITE SYSTEMS DESIGN

#### THESIS

Presented to the Faculty

Department of Aeronatics and Astronautics

Graduate School of Engineering and Management

Air Force Institute of Technology

Air University

Air Education and Training Command

in Partial Fulfillment of the Requirements for the

Daniel R. Barnes, BS 2d Lt, USAF

Degree of Master of Science

March 2017

**DISTRIBUTION STATEMENT A**APPROVED FOR PUBLIC RELEASE; DISTRIBUTION UNLIMITED

# AN ANALYSIS OF RADIO-FREQUENCY GEOLOCATION TECHNIQUES FOR SATELLITE SYSTEMS DESIGN

## THESIS

Daniel R. Barnes, BS 2d Lt, USAF

Committee Membership:

Richard G. Cobb, Ph.D. Chair

Eric D. Swenson, Ph.D. Member

T. Alan Lovell, Ph.D. Member

### Abstract

Radio-frequency geolocation has become critical for applications such as electronic reconnaissance, emergency response or interference mitigation. While geolocation systems have been employed from ground and air-based platforms, CubeSats are currently being evaluated as low-cost solutions for space-based RF geolocation. This research 1) evaluates the effectiveness of CubeSat geolocation and 2) analyzes the sensitivity of different algorithms to system parameters.

This research evaluates the accuracy of AOA, TDOA, and T/FDOA geolocation implemented with 1-4 CubeSats in low Earth orbit (LEO) in the presence of receiver location and measurement errors. The sensitivity of each algorithm to altitude, orbit and cluster geometry, measurement error, and receiver location error is analyzed. This research also includes the geolocation performance analysis of a 500 km altitude CubeSat cluster based on system parameters representative of commercially available hardware.

A MATLAB® simulation is developed to assess geolocation accuracy given variable system designs, such as varied number of space vehicles (SVs), orbit, cluster geometry, technique (AOA, TDOA, T/FDOA), and other system level constraints. The simulation contains the Initial Transmitter Localization (ITL) algorithms as well as the application of an unconstrained maximum likelihood estimator (MLE), which improves upon ITL accuracy by more than 90% in some cases, and a DTED grid search, which improves upon MLE accuracy by up to 40%. For the scenarios investigated, sub-kilometer geolocation accuracy was achievable when AOA, TDOA, and FDOA error was less than 0.05°, 50ns, and 100Hz, respectively.

# Acknowledgements

I would like to thank God for giving me the strength and focus throughout the research process. I'd also like to thank Dr. Richard Cobb, my research advisor and committee chair, for challenging me and guiding me in the right direction. I extend gratitude to Dr. Alan Lovell for introducing me to RF geolocation and mentoring me throughout undergraduate and graduate research. I also extend thanks to Dr. Andrew Sinclair for his continued insights.

I'm thankful for the AFIT faculty members who have aided me in my research, including Dr. Eric Swenson for his continued mentorship, Dr. Richard Martin, Dr. William Weisel, Lt Col Kirk Johnson, and Capt Joshuah Hess.

I'm also thankful for former AFIT students, Capt Nicholas Schmidt and Capt Eric Bailey, for their mentorship. And lastly, thanks to all my ENY-colleagues who have contributed to my success, including 2d Lt John Brick, 2d Lt Anthony Callaham, and 2d Lt Patrick Dunkel.

Daniel R. Barnes

# Table of Contents

	Pag	e,
Absti	act	V
Ackn	owledgements	V
List	f Figures	X
List	f Tables	ii
List	f Abbreviations	X
Nome	nclature xx	ii
1.	Introduction	1
	1.1 Motivation 1.2 Research Objective 1.3 Methodology 1.4 Scope of Research 1.5 Assumptions 1.6 Research Outcomes 1.7 Thesis Organization	2 3 4 4
2.	Background	6
	2.1 CubeSats	9 1 2
	2.4 Initial Transmitter Localization       2         2.4.1 Angle of Arrival       2         2.4.2 Time Difference of Arrival       2         2.4.3 Time/Frequency Difference of Arrival       2         2.4.4 Altitude Assumption       2	4 5 7
	2.5       Estimation       .2         2.5.1       Principle of Maximum Likelihood       .3         2.5.2       Least Squares Estimation       .3         2.5.3       Gauss-Newton Algorithm       .3         2.5.4       Estimate Confidence       .3	0 1 3 5
	2.6 Digital Elevation Models    3      2.7 Summary    3	

			Page
3.	Me	ethodology	39
	3.1	Overview	39
	3.2		
		3.2.1 Transmitter Characterization	
		3.2.2 Orbit Selection	
		3.2.3 Cluster Design	
	3.3	e e e e e e e e e e e e e e e e e e e	
	3.4	1 0	
		3.4.1 True Measurements	
		3.4.2 Corrupted Measurements	58
	3.5	-	
		3.5.1 Corrupt SV Position and Velocity	61
		3.5.2 ITL Methods	
	3.6		
	3.7	Application of DEM	64
	3.8		
		3.8.1 Monte Carlo Simulation	70
	3.9	Summary	72
4.	Sen	nsitivity Analysis	73
	4.1	Overview	73
	1.1	4.1.1 Initial Noise-Free Test	
	4.2	ITL Sensitivity to Altitude	
		4.2.1 AOA Sensitivity to Altitude	
		4.2.2 TDOA Sensitivity to Altitude	
		4.2.3 T/FDOA Sensitivity to Altitude	
		4.2.4 Altitude Sensitivity Summary	
	4.3		
		4.3.1 AOA Sensitivity to Pass Geometry	
		4.3.2 TDOA Sensitivity to Pass Geometry	
		4.3.3 TFDOA2 Sensitivity to Pass Geometry	
		4.3.4 Pass Geometry Sensitivity Summary	
	4.4		
		ITL Sensitivity to the Number of Signal Collects	
		4.5.1 ITL Sensitivity to Collection Geometry	
		4.5.2 Case 1: Addition of "Better" Signal Collects	
		4.5.3 Case 2: Addition of "Worse" Signal Collects	
		4.5.4 Number of Collects Sensitivity Summary	
	4.6		
	-	4.6.1 Absolute Position Knowledge Error	
		4.6.2 Absolute Velocity Knowledge Error	
		4.6.3 Relative Position Knowledge Error	

				Page
	4.7	4.6.5 SV Location Err ITL Sensitivity to Meas	Knowledge Error	114
		Measurement Er 4.7.2 ITL Sensitivity t 4.7.3 ITL Sensitivity t	ror	115
	10			
	4.0	Summary		121
5.	Sys	tem Level Performance .		123
		Effectiveness of MLE an	te Constraint on Accuracy	126
			MLE and DTED1 Grid Search me	
	5.3	-		
	0.0	v	wed	
		5.3.2 TDOA Error All	lowed	135
			owed	
			alysis Summary	
	5.4	System Design		140
6.	Cor	clusions		146
	6.1	Initial Transmitter Loca	alization	146
	6.2	•	nce	
	6.3		8	
			Future Study	
	6.5	Final Conclusion		151
App	endiz	A. ITL Methods		152
	A.2		val	
	1.0		······································	
	A.3		ifference of Arrival	
App	endi		ls	
	B.1			
		B.1.2 DTED Levels I a	and 2	182

		Page
Appendix C.	Additional Results	. 184
Bibliography		. 193

# List of Figures

Figure	Page
1	1U, 1.5U, 2U, and 3U CubeSats [1]7
2	Local-vertical local-horizontal (LVLH) frame [2]10
3	Line of bearing $\hat{\mathbf{d}}$ represents signal $s(t)$ direction of arrival (sensor coordinate frame)
4	Theoretical diagram of a single baseline phase interferometer [3]
5	Uniform circular array geometry in the sensor frame. $A$ antenna elements lie in $s_1s_2$ plane. Angles of arrival $\alpha$ and $\epsilon$ can be measured for the received signal $s(t)$ (adapted from [4])
6	Example MUSIC spectrum for a 4 element UCA with 2 impinging signals [4]
7	1 TDOA measurement yields a hyperbola of possible transmitter locations
8	Sketch of the dual-satellite TDOA-FDOA combined geolocation principle [3]
9	Example output of CAF surface [5]
10	LOB can be represented in ECEF coordinates after being transformed from azimuth, elevation, and range in the body frame
11	Multiple LOBs can be generated in a passs over the transmitter. Sparse LOB geometry leads to more accurate transmitter location estimates
12	The geoid, a reference ellipsoid, and terrain [6]
13	Overview of STK-MATLAB Geolocation Simulation
14	Defining the true transmitter altitude using DTED2 posts
15	SV Pass Geometry for Isotropic Transmitter44

Figure		Page
16	SV Pass Geometry for Radar	45
17	Cluster formation in HCW frame (not to scale)	47
18	4 SVs orbiting within range of a sweeping radar with finite beamwidth	48
19	Relative SV Geometry in HCW Frame for Tx 1, Pass 1, Baseline 15km	50
20	The relationship between various Earth surfaces (highly exaggerated) and a depiction of the ellipsoidal parameters [7]	54
21	Two types of ECEF coordinates and their interrelationship [7]	54
22	Two types of ECEF coordinates and their interrelationship [7]	55
23	$oldsymbol{lpha}$ and $oldsymbol{\epsilon}$ defined in the local East-North-Up coordinate frame	56
24	$lpha$ and $\epsilon$ defined in the SV body frame	56
25	North angle $\phi$ referenced from the local ENU frame to SV body frame	56
26	DTED1 grid search for post that minimizes FOM $\psi$	67
27	Example of DEM iterative grid search when chosen post is near grid boundary ([8])	
28	Geolocation error due to resolution of DTED1	
29	Method of increasing SV altitude for sensitivity analysis (Not to scale)	77
30	AOA algorithm sensitivity to SV altitude (Tx 1, Pass 1, 1 collect, 2000 trials, $\sigma_{\alpha} = \sigma_{\epsilon} = CRLB$ )	78
31	MUSIC $(\sigma_{\alpha}, \sigma_{\epsilon})$ CRLB at different altitudes (See Eqs. 2.3 and 2.4)	78
32	Constant AOA error leads to large estimate uncertainty in presence of large slant range, due to geometry	79

F'igure		Page
33	TDOA3 algorithm sensitivity to SV altitude (Tx 1, Pass 1, 1 collect, 2000 trials, $\sigma_{\tau} = CRLB$ )	80
34	TDOA4 algorithm sensitivity to SV altitude (Tx 1, Pass 1, 1 collect, 2000 trials, $\sigma_{\tau} = CRLB$ )	80
35	Complex Ambiguity Function (CAF) differential time offset CRLB $\sigma_{\tau}$ at different altitudes (See (2.12))	81
36	TFDOA2 algorithm sensitivity to SV altitude (Tx 1, Pass 1, 1 collect, 2000 trials, $\sigma_{\tau} = CRLB$ , $\sigma_{\dot{\tau}} = CRLB$ )	82
37	T/FDOA algorithm sensitivity to SV altitude (Tx 1, Pass 1, 1 collect, 2000 trials, $\sigma_{\tau} = CRLB$ , $\sigma_{\dot{\tau}} = CRLB$ )	82
38	Complex Ambiguity Function (CAF) differential frequency offset CRLB $\sigma_f$ at different altitudes (See (2.12))	83
39	Effect of increasing SV altitude on slant range and elevation of SVs w.r.t. transmitter for non-overhead passes (Not to scale)	84
40	AOA algorithm sensitivity to pass geometry (Tx 1, 2000 trials, $\sigma_{\alpha} = \sigma_{\epsilon} = CRLB$ )	86
41	TDOA3 algorithm sensitivity to pass geometry (Tx 1, 2000 trials, $\sigma_{\tau} = CRLB$ )	87
42	TDOA4 algorithm sensitivity to pass geometry (Tx 1, 2000 trials, $\sigma_{\tau} = CRLB$ )	88
43	TFDOA2 algorithm sensitivity to pass geometry (Tx 1, 2000 trials, $\sigma_{\tau} = CRLB$ , $\sigma_{\dot{\tau}} = CRLB$ )	89
44	TFDOA3 algorithm sensitivity to pass geometry (Tx 1, 2000 trials, $\sigma_{\tau} = CRLB$ , $\sigma_{\dot{\tau}} = CRLB$ )	90
45	TFDOA4 algorithm sensitivity to pass geometry (Tx 1, 2000 trials, $\sigma_{\tau} = CRLB$ , $\sigma_{\dot{\tau}} = CRLB$ )	90
46	TDOA and T/FDOA algorithm sensitivity to baseline distance between SVs (2000 trials)	92

Figure		Page
47	10 ITL solutions obtained from 10 collects with good geometry (TFDOA4 algorithm, Tx 1, Pass 3)	93
48	10 ITL solutions obtained from 10 collects with poor geometry. (TFDOA4 algorithm, Tx 1, Pass 3)	94
49	Collection geometry for Case 1. (Tx 1, Pass 3, 10 Collects)	94
50	Collection geometry for Case 2. (Tx 1, Pass 3, 10 Collects)	95
51	Effect of increasing the number of signal collects on AOA and TDOA4 accuracy for Case 1 (Tx 1, Pass 3, 2000 trials, $\sigma = CRLB$ )	96
52	Effect of increasing the number of signal collects on TDOA3, TFDOA2, TFDOA3, and TFDOA4 accuracy for Case 1 (Tx 1, Pass 3, 2000 trials, $\sigma = CRLB$ )	96
53	Effect of increasing the number of signal collects on AOA and TDOA4 accuracy for Case 2 (Tx 1, Pass 3, 2000 trials, $\sigma = CRLB$ )	97
54	Effect of increasing the number of signal collects on TDOA3, TFDOA2, TFDOA3, and TFDOA4 accuracy for Case 2 (Tx 1, Pass 3, 2000 trials, $\sigma = CRLB$ )	98
55	AOA algorithm sensitivity to absolute position error (Tx 1, Pass 3, 10 collects, 10,000 trials)	100
56	TDOA3 algorithm sensitivity to absolute position error (Tx 1, Pass 3, 1 collect, 10,000 trials)	101
57	AOA algorithm sensitivity to absolute position error (Tx 1, Pass 3, 30 collects, 10,000 trials)	102
58	TDOA3 algorithm sensitivity to Absolute Position Error (Tx 1, Pass 3, 30 collects, 10,000 trials)	102
59	TDOA4 algorithm sensitivity to absolute position error (Tx 1, Pass 3, 30 collects, 10,000 trials)	103
60	TFDOA2 algorithm sensitivity to absolute position error (Tx 1, Pass 3, 30 collects, 10,000 trials)	104

Figure		Page
61	TFDOA3 algorithm sensitivity to absolute position error (Tx 1, Pass 3, 30 collects, 10,000 trials)	. 104
62	TFDOA4 algorithm sensitivity to absolute position error (Tx 1, Pass 3, 30 collects, 10,000 trials)	. 105
63	TFDOA2 algorithm sensitivity to absolute velocity error (Tx 1, Pass 3, 30 collects, 10,000 trials)	. 106
64	TFDOA3 algorithm sensitivity to absolute velocity error (Tx 1, Pass 3, 30 collects, 10,000 trials)	. 107
65	TFDOA4 algorithm sensitivity to absolute velocity error (Tx 1, Pass 3, 30 collects, 10,000 trials)	. 107
66	TDOA3 algorithm sensitivity to relative position error (Tx 1, Pass 3, 30 collects, 10,000 trials)	. 109
67	TDOA4 algorithm sensitivity to relative position error (Tx 1, Pass 3, 30 collects, 10,000 trials)	. 110
68	TFDOA2 algorithm sensitivity to relative position error (Tx 1, Pass 3, 30 collects, 10,000 trials)	. 110
69	TFDOA3 algorithm sensitivity to relative position error (Tx 1, Pass 3, 30 collects, 10,000 trials)	. 111
70	TFDOA4 algorithm sensitivity to relative position error (Tx 1, Pass 3, 30 collects, 10,000 trials)	. 111
71	TFDOA2 algorithm sensitivity to relative velocity error (Tx 1, Pass 3, 30 collects, 10,000 trials)	. 112
72	TFDOA3 algorithm sensitivity to relative velocity error (Tx 1, Pass 3, 30 collects, 10,000 trials)	. 113
73	TFDOA4 algorithm sensitivity to relative velocity error (Tx 1, Pass 3, 30 collects, 10,000 trials)	. 113
74	AOA algorithm sensitivity to angle measurement error (Tx 1, Pass 3, 2000 trials, $\sigma_{\alpha} = \sigma_{\epsilon}$ )	. 115
75	TDOA3 algorithm sensitivity to DTO error (Tx 1, Pass 3, 2000 trials, $\sigma_f = 0Hz$ )	

Figure		Page
76	TDOA4 algorithm sensitivity to DTO error (Tx 1, Pass 3, 2000 trials, $\sigma_f = 0Hz$ )	117
77	TFDOA2 algorithm sensitivity to DTO error (Tx 1, Pass 3, 2000 trials, $\sigma_f = 0Hz$ )	117
78	TFDOA3 algorithm sensitivity to DTO error (Tx 1, Pass 3, 2000 trials, $\sigma_f = 0Hz$ )	118
79	TFDOA4 algorithm sensitivity to DTO error(Tx 1, Pass 3, 2000 trials, $\sigma_f = 0Hz$ )	118
80	TFDOA2 algorithm sensitivity to DFO error (Tx 1, Pass 3, 2000 trials, $\sigma_{\tau} = 0s$ )	119
81	TFDOA3 algorithm sensitivity to DFO error (Tx 1, Pass 3, 2000 trials, $\sigma_{\tau} = 0s$ )	120
82	TFDOA4 algorithm sensitivity to DFO error (Tx 1, Pass 3, 2000 trials, $\sigma_{\tau} = 0s$ )	120
83	TDOA3 final $h_u$ error for three different surface of the Earth constraints (Tx 4 with true WGS84 height = 1.39 km, Pass 3)	125
84	TDOA3 geolocation error for three different surface of the Earth constraints (Tx 4 with true WGS84 height = 1.39 km, Pass 3)	125
85	Effect of AOA measurement error on AOA geolocation accuracy with application of DTED1 Earth constraint (2000 trials)	135
86	Effect of TDOA measurement error on TDOA3 geolocation accuracy with application of DTED1 Earth constraint (500 trials)	136
87	Effect of TDOA measurement error on TDOA4 geolocation accuracy with application of DTED1 Earth constraint (500 trials, Passes 1-4)	136
88	Effect of TDOA measurement error on TFDOA3 geolocation accuracy with application of DTED1 Earth constraint (500 trials, $\sigma_f = 10Hz$ )	137

Figure	Page
89	Effect of TDOA measurement error on TFDOA4 geolocation accuracy with application of DTED1 Earth constraint (500 trials, $\sigma_f=10Hz$ )
90	Effect of FDOA measurement error on TFDOA3 geolocation accuracy with application of DTED1 Earth constraint (500 trials)
91	Effect of FDOA measurement error on TFDOA4 geolocation accuracy with application of DTED1 Earth constraint (500 trials)
92	Effect of TDOA measurement error on TFDOA3 geolocation accuracy with application of DTED1 Earth constraint (500 trials, $\sigma_f = 10Hz$ )
93	Effect of FDOA measurement error on TFDOA3 geolocation accuracy with application of DTED1 Earth constraint (500 trials, $\sigma_{\tau} = 50ns$ )
94	AOA Algorithm Overview
95	An impinging signal as shown in the sensor frame
96	The line of bearing unit vector $\hat{\mathbf{d}}$ for a single $\alpha$ and $\epsilon$
97	LOB can be represented in ECEF coordinates after being transformed from azimuth, elevation, and range in the body frame
98	TDOA4 Algorithm Overview
99	Root Disambiguation Process
100	TDOA3 Algorithm Overview
101	Altitude Iteration Process
102	TFDOA2 Algorithm Overview
103	TFDOA3 Algorithm Overview
104	Solving for $\rho_1$ using Newton Method
105	TDOA4 algorithm sensitivity to absolute position error (Tx 1, Pass 3, 1 collect, 10,000 trials)

Figure		Page
106	TFDOA2 algorithm sensitivity to absolute position error (Tx 1, Pass 3, 1 collect, 10,000 trials)	185
107	TFDOA3 algorithm sensitivity to absolute position error (Tx 1, Pass 3, 1 collect, 10,000 trials)	185
108	TFDOA4 algorithm sensitivity to absolute position error (Tx 1, Pass 3, 1 collect, 10,000 trials)	186
109	TFDOA2 algorithm sensitivity to absolute velocity error (Tx 1, Pass 3, 1 collect, 10,000 trials)	186
110	TFDOA3 algorithm sensitivity to absolute velocity error (Tx 1, Pass 3, 1 collect, 10,000 trials)	187
111	TFDOA4 algorithm sensitivity to absolute velocity error (Tx 1, Pass 3, 1 collect, 10,000 trials)	187
112	TDOA3 algorithm sensitivity to relative position error (Tx 1, Pass 3, 1 collect, 10,000 trials)	188
113	TDOA4 algorithm sensitivity to relative position error (Tx 1, Pass 3, 1 collect, 10,000 trials)	188
114	TFDOA2 algorithm sensitivity to relative position error (Tx 1, Pass 3, 1 collect, 10,000 trials)	189
115	TFDOA3 algorithm sensitivity to relative position error (Tx 1, Pass 3, 1 collect, 10,000 trials)	189
116	TFDOA4 algorithm sensitivity to relative position error (Tx 1, Pass 3, 1 collect, 10,000 trials)	190
117	TFDOA2 algorithm sensitivity to relative velocity error (Tx 1, Pass 3, 1 collect, 10,000 trials)	190
118	TFDOA3 algorithm sensitivity to relative velocity error (Tx 1, Pass 3, 1 collect, 10,000 trials)	191
119	TFDOA4 algorithm sensitivity to relative velocity error (Tx 1, Pass 3, 1 collect, 10,000 trials)	191
120	Effect of TDOA measurement error on TDOA4 geolocation accuracy with application of DTED1 Earth constraint (500 trials)	192

# List of Tables

Table		Page
2	Overview of ITL Methods Utilized	25
3	DTED Post Sizes (Adapted from [8,9])	36
4	Simulation Input Parameters	40
5	ARSR-4 Signal Characteristics [10]	41
6	Transmitter Locations	42
7	Chief SV Orbital Elements for All Passes	46
8	Baseline Data for All Passes $(\Delta b = 15km)$	51
9	Link Budget Parameters and Assumptions	59
10	Measures of Performance	69
11	Sensitivity Analysis Trade Space	74
12	ITL Method Accuracy and Computation Time in Noise-Free Case	76
13	Parameters for Effectiveness of MLE/DTED1 Test	. 128
14	Geolocation accuracy with the application of MLE and a DTED1 grid search	. 129
15	Percent improvement of geolocation accuracy due to MLE and DTED1 application	. 130
16	Computation time for MLE and DTED1 grid search	. 133
17	Performance Analysis Parameters	. 134

# List of Abbreviations

ADCS Attitude, Determination, and Control Subsystem

**AFIT** Air Force Institute of Technology

AMD Average Miss Distance

**AOA** Angle of Arrival

ARSR-4 Air Route Surveillance Radar Series 4

CanX Canadian Advanced Nanospace eXperiment

C&DH Command and Data Handling

**CAF** Complex Ambiguity Function

CRLB Cramér-Rao Lower Bound

**DEM** Digital Elevation Model

**DF** Direction Finding

**DFO** Differential Frequency Offset

**DOA** Direction of Arrival

**DTED** Digital Terrain Elevation Data

**DTED0** Level 0 Digital Terrain Elevation Data

**DTED1** Level 1 Digital Terrain Elevation Data

**DTED2** Level 2 Digital Terrain Elevation Data

**DTO** Differential Time Offset

**ENU** East-North-Up

**ECEF** Earth-centered Earth-fixed

EGM96 Earth Gravitational Model 1996

FDOA Frequency Difference of Arrival

**FOM** Figure of Merit

GDOP Geometric Dilution of Precision

GMTED2010 Global Multi-resolution Terrain Elevation Data 2010

GNC Guidance, Navigation and Control

**GPS** Global Positioning System

**HCW** Hill-Clohessy-Wiltshire

ITL Initial Transmitter Localization

LAN Longitude of the Ascending Node

**LEO** Low Earth Orbit

LOB Line of Bearing

LS Least-squares

LVLH Local-vertical Local-horizontal

MCS Monte Carlo Simulation

MLE Maximum Likelihood Estimation

MOP Measure of Performance

MUSIC Multiple Signals Classification Algorithm

NCO Non-coplanar Oscillator

NGA National Geospatial-Intelligence Agency

NMC Natural Motion Circumnavigation

NWLS Nonlinear Weighted Least Squares

PDF Probability Density Function

P-POD Poly-Picosatellite Orbital Deployer

**RAAN** Right Ascension of the Ascending Node

**RF** Radio-frequency

RMSE Root Mean Square Error

Rx Receiver

SMA Semi-major Axis

SNR Signal-to-noise Ratio (C/N)

SRTM Shuttle Radar Topography Mission

STK Systems Tool Kit

Space Vehicle

**TDOA** Time Difference of Arrival

**TDOA3** 3-SV Time Difference of Arrival

TDOA4 4-SV Time Difference of Arrival

TRL Technology Readiness Level

T/FDOA Combined Time and Frequency Difference of Arrival

**TFDOA2** 2-SV Time and Frequency Difference of Arrival

**TFDOA3** 3-SV Time and Frequency Difference of Arrival

**TFDOA4** 4-SV Time and Frequency Difference of Arrival

Tx Transmitter

UAV Unmanned Aerial Vehicle

UCA Uniform Circular Array

USGS U.S. Geological Survey

WGS84 World Geodetic System 84

WLS Weighted Least Squares

# Nomenclature

Note: Positions and velocities in ECEF unless otherwise stated

- a Vector (lowercase, bold)
- A Matrix (uppercase, bold)
- a Scalar variable or magnitude of a vector
- A Constant (uppercase)
- $\tilde{a}$  Noise corrupted (tilde)
- C Estimate covariance or confidence
- I Identity matrix
- L Number of measurement parameters in a signal collect
- **m** Measurement vector (e.g.  $[\alpha, \epsilon]^T$ )
- M Total number of measurements
- p Location of terrain post
- P Total number of terrain posts
- Q Covariance matrix of noise inputs
- $\boldsymbol{\rho}_i$  Range vector from transmitter to  $i^{th}$  satellite,  $[\mathbf{s}_i \mathbf{u}]$
- $\rho_i$  Euclidean distance from transmitter to  $i^{th}$  satellite,  $||\boldsymbol{\rho}_i||$
- $\dot{\rho}_i$  Time rate of change of  $\rho_i$
- $r_{i1}$  Range difference between  $i^{th}$  and reference satellite,  $\rho_i \rho_1$
- $\dot{r}_{i1}$  Range rate difference between  $i^{th}$  and reference satellite,  $\dot{\rho}_i \dot{\rho}_1$
- $\mathbf{s}_i$  Satellite position  $[x, y, z]^T$
- $\dot{\mathbf{s}}_i$  Satellite velocity  $[v_x, v_y, v_z]^T$
- S Number of satellites
- $au_{21}$  Time difference of arrival of received signal between satellite 2 and 1
- $\dot{\tau}_{21}$  –TDOA time rate of change / nondimensionalized FDOA,  $(f_{di}-f_{d1})/f_c$
- u Transmitter position
- W Weighting matrix of T/FDOA equation error

# AN ANALYSIS OF RADIO-FREQUENCY GEOLOCATION TECHNIQUES FOR SATELLITE SYSTEMS DESIGN

## 1. Introduction

The 21<sup>st</sup> century has seen rapid development in spacecraft technology and the number of satellites has increased exponentially. Geolocation of radio-frequency (RF) transmitters is not a new concept, but with the increase of satellite capabilities and the advent of CubeSats the military and commercial world have found utility in geolocating transmitters from space [3].

Space-based RF geolocation involves estimating the location of a transmitter based on its signal received at one or more satellites. Space-based geolocation has many military and commercial applications. Geolocation techniques could be useful for search and rescue missions, locating RF sources attempting to jam communication satellites, or estimating the location of an unknown enemy transmitter [3, 11, 12]. There are multiple algorithms that can be applied in space-based geolocation, each of which utilize the frequency, angle of arrival, or time of arrival of an RF signal to determine an estimate for the location of the transmitter. The choice of geolocation technique depends on many different factors, including whether the transmitter is cooperative or not, i.e. whether its characteristics are known, how many satellite receivers are available, orbit design, and other system level constraints. This research focuses on the Angle of Arrival (AOA), Time Difference of Arrival (TDOA), and combined Time and Frequency Difference of Arrival (T/FDOA) methods applied from CubeSats in Low Earth Orbit (LEO).

#### 1.1 Motivation

Geolocation is by no means a novel subject of research, but within the last few decades there has been an increased amount of research applying geolocation from new platforms, namely satellites and unmanned aerial vehicles (UAVs) [13–15]. Nanosatellites, commonly referred to as CubeSats because of their standardized cube-like form factor, have become increasingly popular due to their accessibility and low cost [16]. The number of CubeSat missions has skyrocketed as space mission designers have explored CubeSat operational capabilities that were once exclusive to large satellites [17–19]. Several small satellite RF geologation missions have emerged in the last few years. The SAMSON mission consists of a cluster of autonomous 3U Cube-Sats employing TDOA and FDOA geolocation of a cooperative RF transmitter [20]. Pathfinder, developed by HawkEye 360 [12], is a 3-Microsatellite cluster in a 575 km circular orbit designed to execute T/FDOA geolocation. The Air Force Institute of Technology (AFIT) has been investigating the feasibility of CubeSat geolocation for several years, and multiple theses have been dedicated to the topic [4,8,21,22]. As small satellite geolocation missions are being realized, the need to implement RF geolocation theory for system design and performance analysis is increasing.

#### 1.2 Research Objective

The goal of this thesis is to explore two questions. The first question is, how sensitive are the AOA, TDOA, and T/FDOA geolocation techniques to system parameters, such as measurement or space vehicle (SV) positioning error? The second question is, how accurately can a CubeSat in LEO geolocate an RF transmitter based on system parameters representative of commercially available hardware? The method of answering the first question will be to conduct a sensitivity analysis for six common RF localization algorithms that utilize AOA, TDOA, and FDOA mea-

surements. A system level performance analysis will be conducted to investigate the second research question. These analyses require the development of an end-to-end geolocation simulation, which will be discussed in the next section.

### 1.3 Methodology

A MATLAB® simulation will be developed to determine the geolocation accuracy achievable for a variety of geolocation scenarios and system parameters. A geolocation scenario will be simulated in Systems Tool Kit (STK®) where a ground transmitter and satellite receivers in LEO will be defined. Imported data from the STK scenario will be combined with user defined system parameters in MATLAB to simulate angle, time, and frequency measurements. Previously developed [4,23–25] geolocation algorithms will be utilized to conduct initial transmitter localization (ITL). The MATLAB simulation will also apply maximum likelihood estimation and a new technique for implementing digital terrain elevation data for a surface of the Earth constraint. This geolocation tool will be utilized to conduct the sensitivity and performance analyses, as well as provide a framework for further geolocation analysis.

#### 1.4 Scope of Research

Simulation of a space-based geolocation scenario involves several steps. It includes characterizing the RF transmitter of interest, defining the number of satellites, satellite orbits and receiver characteristics, modeling the signal propagation, detection and processing, executing a geolocation algorithm, then using an estimation technique to derive a location estimate and covariance. The front end of the simulation spans from RF transmitter definition to a stored angle, frequency, or time measurement. The back end of the simulation is considered to be the process of obtaining a single location estimate and covariance from an angle, frequency, or time measurement. This thesis

is primarily focused on the back end of the geolocation scenario, with some thought given to the front end only for the purposes of setting up a realistic scenario. The investigation of signal measurement algorithms are outside the scope of this research, however signal measurement errors are considered.

### 1.5 Assumptions

There are also other underlying assumptions present in this research. It is assumed that the RF signal of interest is from a single, stationary, terrestrial transmitter. The relative velocity of the satellite receiver compared with the velocity of a moving terrestrial transmitter makes the stationary transmitter assumption favorable for this research. Although a scenario of multiple transmitters is possible, only a single-transmitter scenario is considered. The only information known about the RF transmitter is its carrier frequency. Co-channel interference and multipath effects are neglected and it is assumed that the signal of interest can be detected, segregated from other in-band signals, and processed. Furthermore, it is assumed the satellites receiving the signals are CubeSats in LEO. For this scenario the CubeSats are taken to be 12U ( $24 \times 36 \times 24$   $cm^3$ ) and their altitude is 500 km. It is assumed that the CubeSats are able to perform orbit maintenance and are operationally available during the time they have line of sight to the transmitter.

#### 1.6 Research Outcomes

In addition to the sensitivity and performance analyses previously discussed, a guide for utilizing the geolocation tool set will be produced. The geolocation tool set produced in this effort will benefit future AFIT students involved in the space vehicle design sequence. The simulation can be utilized to answer two different questions. Firstly, given a required geolocation accuracy, which system design parameters would

be needed for each geolocation algorithm? And on the contrary, given a set of system parameters, what is the best accuracy that can be achieved?

This research will provide a framework for future geolocation analyses and Cube-Sat preliminary design. Future students or system designers will be able to leverage the tool in determining the best constellation design and hardware requirements for accomplishing a geolocation mission using CubeSats. Additional analyses pertaining to the mission concept of operations can be conducted using the simulation. Optimal cluster geometries for CubeSat geolocation can be investigated. Furthermore, trade studies can be performed to determine the usefulness of platforms capable of employing multiple geolocation algorithms at once, or the performance risk due to on-orbit CubeSat failure.

#### 1.7 Thesis Organization

Chapter 2 discusses existing geolocation techniques. Chapter 3 outlines the methodology used to simulate a geolocation scenario for 1-4 CubeSats. Chapter 4 discusses the results for the sensitivity analysis. Chapter 5 discusses the system level performance of a LEO CubeSat. Chapter 6 presents the conclusions of the research along with recommendations for future research.

# 2. Background

Geolocation is simply the process of determining the geographical location of an object. Space-based RF geolocation is the process of locating an RF transmitter using satellite sensors. RF geolocation can be divided into two steps: measurement and estimation [13]. The effectiveness of a geolocation system depends on its ability to sense the RF signal of interest, obtain a measurement, and estimate the location of the transmitter based on the measurements received. As an RF signal arrives at a satellite sensor it has at least three attributes which yield useful measurement information: its frequency, phase, and time of arrival. There has been significant research on methods of processing measurements and determining an RF transmitter's location based on these measurements [3,11].

#### 2.1 CubeSats

Advent of CubeSats A CubeSat is a small satellite made up of roughly  $10 \times 10 \times 10 \ cm^3$  cubes [16]. A 1U CubeSat is therefore a  $10 \times 10 \times 10 \ cm^3$  cube and a 3U CubeSat is approximately  $10 \times 10 \times 30 \ cm^3$ .

The design of CubeSats originated at California Polytechnic University (Cal Poly) and Stanford University in 1999 [16]. The CubeSat is ideal because it is small, relatively inexpensive, and standardized, allowing it to be versatile in supporting a variety of applications and accommodating a shorter development cycle than large satellite programs [16]. Thus CubeSat development has not only served the needs of the DoD, but has become accessible to university research worldwide.

Cal Poly has published specifications that govern the design of CubeSats [26]. CubeSats are standardized to fit within and deploy from Poly-Picosatellite Orbital Deployers (P-POD), which were also developed by Cal Poly and Stanford. The ability

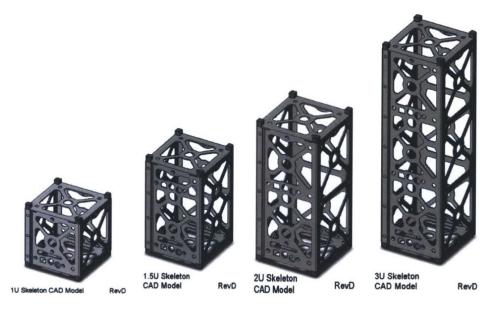


Figure 1. 1U, 1.5U, 2U, and 3U CubeSats [1]

for payload engineers to design their payloads to fit within a standard bus provides flexibility, reduces cost, and greatly decreases the time from design to launch [16].

CubeSat Geolocation Missions The Air Force Institute of Technology (AFIT) space vehicle design course has featured various CubeSat geolocation mission designs. GeoLoco [27] was a 3-CubeSat design employing TDOA and AOA geolocation from LEO. Anubis [28] and ERIC [10] each involved single-CubeSat AOA geolocation from LEO. In addition to AFIT SV design studies, the Technion-Israel Institute of Technology has developed a geolocation mission called the Satellite Mission for Swarming and Geolocation (SAMSON). SAMSON consists of a 3-CubeSat LEO constellation designed to conduct TDOA geolocation [20]. Another geolocation mission, Pathfinder, has been developed by HawkEye 360 [12]. Pathfinder features a 3-Microsatellite cluster in a 575 km circular orbit designed to execute T/FDOA geolocation [12].

Guidance, Navigation, and Control Employing CubeSats to conduct RF geolocation presents many SV design challenges due to the size, weight, and power constraints. In addition, geolocation using a CubeSat cluster presents command and data handling (C&DH) challenges associated with cross linking and synchronizing received signals. However, the most notable design challenge is the the guidance, navigation, and control (GNC) subsystem. The GNC subsystem of a spacecraft contains the components used for absolute and relative position determination and for the attitude determination and control system (ADCS) [18]. RF Geolocation requires precise position and attitude determination, so CubeSat GNC limitations have a significant impact on mission success.

Attitude Determination For AOA geolocation, precise attitude determination is vital. Typical components included in the ADCS are reaction wheels, magnetometers, magnetorquers, and star trackers [18]. NASA Small Spacecraft Technology Program's 2015 report [18] presented three star trackers of technology readiness level (TRL) 9 which can yield between 0.02° and 0.007° attitude determination accuracy.

Absolute Positioning On-board Global Positioning System (GPS) receivers are the primary method used by small satellites in LEO for absolute orbit determination [18]. According to NASA [18] the state of the art for absolute position accuracy is currently 1.5 m in each axis. Canadian Advanced Nanospace eXperiment (CanX), a dual nanosatellite mission of the University of Toronto launched in June 2014, employed GPS receivers for orbit determination in a formation flying demonstration. In November 2014, CanX accomplished its mission goals, including the achievement of absolute position and velocity determination accurate to within 10 m and 20 cm/s, respectively [29]. As expected, a 2 m bias was incorporated in the error due to the geometric distribution of GPS satellites.

Relative Positioning Relative navigation of small satellites has been an area of increasing interest. Bandyopadhay et al. [19] reviews recent small satellite formation flying missions which have either been completed or are still in development. Relative navigation is more precise than absolute navigation due to the use of differential GPS. Differential GPS uses the GPS measurements obtained at multiple receivers to eliminate errors common to all receivers [30], thereby reducing relative position and velocity estimation error. The CanX satellites demonstrated relative position and velocity determination accurate to within 10 cm and 3 cm/s, respectively [29].

## 2.2 Formation Flying

As previously mentioned, there have been several developed or completed small satellite formation flying missions, including Pathfinder [12], SAMSON [20], CPOD [31], AeroCube-4 [32], and CanX [29]. CanX accomplished formation maneuvers with two 20-cm cube satellites spaced less than 1 km apart [29]. NASA's CubeSat Proximity Operations Demonstration (CPOD) [31] features the formation of two 3U CubeSats spaced up to 25 km apart. The HawkEye 360 Pathfinder mission, featuring a 3-microsatellite cluster designed for RF geolocation, intends to have a baseline distance of 125-250 km [14]. The technological advancement of autonomy and relative navigation has paved the way for CubeSat formation flying missions. Multi-satellite geolocation is just one of many possibilities.

Hill-Clohessy-Wiltshire Equations In formation flying, the relative satellite motion is commonly described in a non-inertial coordinate frame called the local-vertical local-horizontal (LVLH) frame, seen in Fig. 2. The LVLH frame reference is the chief SV orbit, and the reference orbit does not have to be occupied by a phys-

ical SV. In the LVLH frame, x, y, and z are referred to as the radial, in-track, and cross-track directions, respectively. As seen in Fig. 2, y is perpendicular to x and z completes the right-handed coordinate system, and is perpendicular to the orbital plane. Curtis [33] discusses the dynamics of relative satellite motion. When the orbit

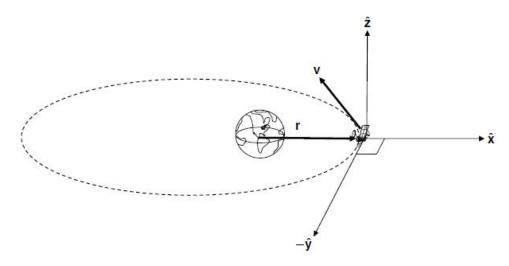


Figure 2. Local-vertical local-horizontal (LVLH) frame [2]

of the chief SV is circular, then y is in the direction of the chief SV velocity vector, and the frame can be referred to as the Hill-Clohessy-Wiltshire (HCW) frame [33]. The HCW equations describe the motion of a SV with respect to a reference SV in a circular orbit [33].

$$\delta \ddot{x} - 3n^2 \delta x - 2n \delta \dot{y} = 0$$

$$\delta \ddot{y} + 2n \delta \dot{x} = 0$$

$$\delta \ddot{z} + n^2 \delta z = 0$$
(2.1)

In Eq. 2.1 n is the chief SV's mean motion. Since all of the orbits discussed in this research are circular, the LVLH frame will be referred to as the HCW frame. Alfriend et al. [2] manipulate the HCW equations to express the x, y, z position of a deputy SV in the HCW frame at an instant in time. The deputy position is expressed in

terms of the chief SV's orbital elements and the deviation  $\delta$  in orbital elements [2]:

$$x = \delta r$$

$$y = r_1(\delta \theta + \delta \Omega \cos i_1)$$

$$z = r_1(\delta i \sin \theta_1 - \delta \Omega \sin i_1 \cos \theta_1)$$
(2.2)

 $i_1$ ,  $\theta_1$ , and  $r_1$  are the inclination, argument of latitude, and radius from the Earth's center of the chief SV, respectively.  $\delta\Omega$  is the difference in longitude of the ascending node (LAN) between the two SVs ( $\delta\Omega = \Omega_2 - \Omega_1$ ). These equations are approximations for an reference time  $t_0$ , because x, y, z change as the deputy orbits around the chief SV.

Formations The satellite formation certainly has an impact on the geolocation accuracy of the system [14]. CaJacob et al. [14] discuss a few formations considered for their CubeSat geolocation cluster. In general, geometric diversity of the formation yields better geolocation accuracy but sacrifices simplicity [14]. The Non-Coplanar Oscillator (NCO) formation, features two satellites in the same orbital plane but shifted in phase, and the third satellite in an offset plane defined by some change in inclination or right ascension of the ascending node (RAAN) [14]. This formation is less complex than a Natural Motion Circumnavigation (NMC) formation and more geometrically diverse than a Co-Planar arrangement [14]. A formation similar to NCO is utilized in this research. The exploration of optimal formations for geolocation is left for future work.

#### 2.3 Signal Measurement

The first step in geolocating an RF transmitter is to measure the angle, time, and/or frequency of its signal as sensed by the receiver. There are different techniques

and hardware required for measuring angle, time, and frequency of arrival. Gentile et al. [11] discuss multiple geolocation measurement techniques, including the conditions under which they are utilized. While signal measurement techniques were not utilize in this research, a discussion is necessary to give the reader a perspective of the challenges associated with the different geolocation methods. This thesis will examine three different passive geolocation measurement techniques: angle of arrival (AOA), time difference of arrival (TDOA), and combined time and frequency difference of arrival (T/FDOA). Each section contains the measurement model, common methods for signal measurement, sources of error, and advantages and disadvantages.

#### 2.3.1 Angle of Arrival

#### 2.3.1.1 Measurement Model

When an RF signal is sensed by a satellite receiver, the direction of arrival (DOA) can be measured. In three-dimensional space, the signal's DOA can be fully described by two angles, known as the AOA. Similarly, if a DOA or AOA is obtained, a line of bearing can be generated with the receiver as its reference point.

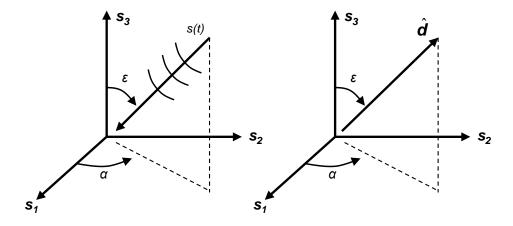


Figure 3. Line of bearing  $\hat{\mathbf{d}}$  represents signal s(t) direction of arrival (sensor coordinate frame)

If using space-based receivers, the intersection of this line of bearing (LOB) with

the surface of the Earth or with other LOBs can give the estimated location of the unknown RF transmitter. AOA measurements can be obtained using a single satellite receiver. The process of determining the AOA of an RF signal is commonly known as direction finding (DF) [3]. The most common technique of transmitter DF is the use the amplitude or phase measurements of the RF signal at multiple antennas to determine an AOA [3].

#### 2.3.1.2 Phase interferometry

The method of measuring the direction of incoming waves based on their phase difference at different antennas is referred to as phase interferometry [3]. At least two antennas are required to determine a single angle of arrival. Fig. 4 shows the general concept of the angle measurement and estimation. Once the signals are processed there must be phase correlation to produce an AOA.

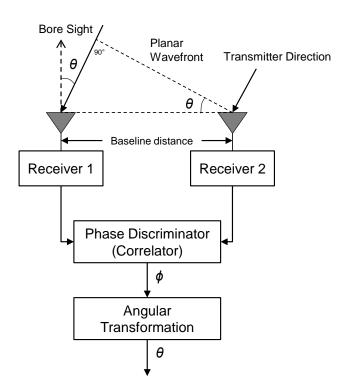


Figure 4. Theoretical diagram of a single baseline phase interferometer [3]

In order to achieve 2D angle estimation, or in other words, an azimuth and elevation of arrival, an antenna array is needed [3]. Antenna arrays are effective because they provide a variation in baseline length, and minimize the likelihood of phase ambiguity and poor AOA measurement accuracy, depending on the RF signal direction of arrival. There is significant literature evaluating the efficacy of different antenna array configurations, most commonly linear and circular arrays [34,35]. Tan [35] investigated the application of a wireless location system using a uniform circular array (UCA, see Fig. 5). Bailey [4] explored the implementation of a UCA hoisted on a 6U CubeSat.

# 2.3.1.3 Multiple Signals Classification Algorithm

A new direction finding technique is known as space spectrum estimation, or the process of estimating the spatial frequency and determining other parameters according to the output signal from multiple antenna elements [3]. The Multiple Signals Classification (MUSIC) algorithm is a common spectrum estimation technique developed by Schmidt in 1979 [36]. It utilizes the eigenstructure of the spatial covariance matrix of signals received by A antenna elements to determine the AOA of each impinging signal [36]. Bailey [4] investigated how the MUSIC algorithm could be applied with a UCA. One limitation of utilizing a UCA is the array elements must be no more than  $\frac{\lambda}{2}$  apart,  $\lambda$  being the wavelength of the received signal in order for the phase difference to be distinguished. This constrains the minimum signal frequency that can be detected due to the limited surface area available on a CubeSat.

The MUSIC algorithm has the ability to resolve multiple signals at the same time [36]. If A is the number of antennas it is generally able to segregate A-1 impinging signals. Once executed, the peak values of the MUSIC spectrum can be extracted to obtain the AOA (Fig. 6).

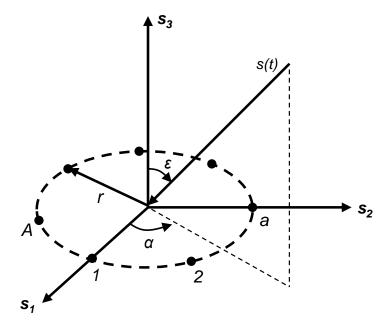


Figure 5. Uniform circular array geometry in the sensor frame. A antenna elements lie in  $s_1s_2$  plane. Angles of arrival  $\alpha$  and  $\epsilon$  can be measured for the received signal s(t) (adapted from [4]).

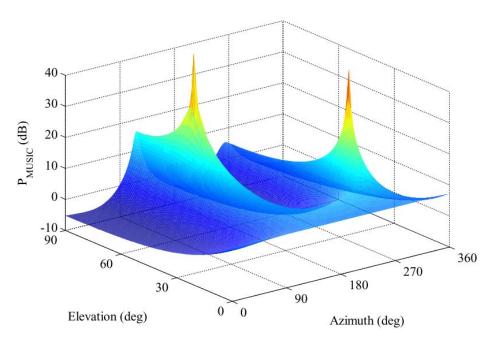


Figure 6. Example MUSIC spectrum for a 4 element UCA with 2 impinging signals [4]

MUSIC has several advantages over traditional DF techniques. Its incorporation of digital signal processing technology gives it higher accuracy and super-resolution, and it has been widely researched and implemented [3].

#### 2.3.1.4 Accuracy

In general, the accuracy of angle measurement techniques depends on the signal processing capability of the receiver, the antenna array used, the RF environment, and the signal characteristics. Thus the AOA measurement problem is relatively complex. With respect to signal processing, the phase and frequency measurement error at the receiver contribute to overall AOA error [3]. The phase of the signals must be properly measured and discriminated. In addition, the geometry of the antenna array limits the capability of the AOA measurement and effects its maximum accuracy. A smaller distance between the antennas, or small baseline length, leads to a greater AOA measurement error [3]. On the other hand, if the baseline is too large baseline distance relative to the signal's wavelength, the problem of phase ambiguity could occur [3].

Bailey [4] analyzed the MUSIC algorithm in depth and investigated its theoretical performance for a 4-antenna UCA on a 6U CubeSat. In general, the accuracy of the AOA measurement depends on the signal-to-noise ratio (SNR)  $\gamma$  of the received signal, the number of samples of the signal N, the number of antenna elements A, the radius of the UCA r, and the wavelength of the received signal  $\lambda_r$  [4]. He showed that for a 4-antenna UCA receiving a narrow-band signal the MUSIC theoretical AOA error approached the 2D angle Cramér-Rao Lower Bound (CRLB) in scenarios where the signal-to-noise ratio  $\gamma$  and the number of samples N is sufficiently high. The CRLB on the variance of 2D angle estimates is given in Eq. 2.4 and Eq. 2.3, respectively [4].

$$\sigma_{\alpha}^{2} = \frac{\gamma^{-1} + A}{\gamma N A^{2} (2\pi r/\lambda_{r})^{2} \sin^{2}(\epsilon)}$$
(2.3)

$$\sigma_{\epsilon}^{2} = \frac{\gamma^{-1} + A}{\gamma N A^{2} (2\pi r/\lambda_{r})^{2} \cos^{2}(\epsilon)}$$
(2.4)

It can be observed that the theoretical error is negligibly impacted by the azimuth of arrival. However as elevation of arrival approaches 90 degrees as defined by (Fig. 5), the elevation variance increases and the azimuth variance decreases. In other words, if the direction of the incoming signal is parallel to the plane of the array the system is prone to higher elevation measurement error.

#### 2.3.1.5 Advantages and Disadvantages

AOA geolocation has several advantages. Firstly, it can be employed with a single satellite, removing the complexity of a cluster of satellites. Therefore time synchronization and cluster maintenance do not need to be considered. It is also typically fast and favorable to signal sorting [3]. However, the payloads for AOA geolocation platforms are more complex because they require multiple antennas on a single satellite. Single-SV AOA requires precise receiver attitude measurement, and as SV attitude knowledge error and SV altitude increase, the AOA geolocation estimate error increases. Another challenge is obtaining accurate angle estimation, as with the MUSIC algorithm [11]. As a result, AOA geolocation error is typically large compared to TDOA or T/FDOA measurements taken from a similar altitude [3].

# 2.3.2 Time and Frequency Difference of Arrival

The time difference of arrival (TDOA) and frequency difference of arrival (FDOA) of an RF signal can be determined with more than one satellite. There has been

significant research on the application of geolocation using only TDOA measurements and the combination of TDOA and FDOA measurements [13, 23, 37]. Most satellite systems utilize TDOA measurements for geolocation, however FDOA measurements can also be obtained if relative motion exists between the transmitter and the receivers [23]. Since the relative velocity between LEO satellites and a stationary transmitter is nearly 7 km/s, using FDOA measurements is a valid approach. The following Sections 2.3.2.1 and 2.3.2.2, discuss how TDOA and T/FDOA measurements are useful for obtaining transmitter position estimates.

#### 2.3.2.1 TDOA Measurement Model

The time difference  $\tau_{i1}$  measured between the  $i^{th}$  SV receiver and the reference SV receiver (1) can be related to the range difference  $r_{i1}$  between each SV and the transmitter, respectively.

$$\tau_{i1} = t_i - t_1 = \frac{\rho_i - \rho_1}{c} = \frac{r_{i1}}{c} \qquad i = 2, 3..., S$$

$$\rho_i \equiv ||\boldsymbol{\rho}_i|| = ||\mathbf{s}_i - \mathbf{u}||$$
(2.5)

Note that  $t_i$  is the time the signal was received at SV i,  $\rho_i$  is the range from the transmitter to the  $i^{th}$  SV,  $\mathbf{s}_i$  is the ECEF position of the  $i^{th}$  SV, and  $\mathbf{u}$  is the true ECEF transmitter position. There are multiple transmitter locations that could satisfy this equation. A hyperbola can be defined as a set of points in a plane whose distances to two fixed points have a constant difference. In 2D space, multiple hyperbolas from multiple independent TDOA measurements can be intersected to determine a transmitter location [24].

Therefore in 3D space, for a single TDOA, the transmitter could lie on the surface of a hyperboloid. Two TDOA measurements yield two hyperboloids, and the intersection of these hyperboloids leads to a curve of interest. In order to determine

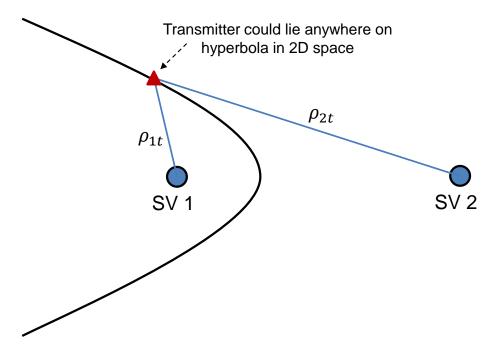


Figure 7. 1 TDOA measurement yields a hyperbola of possible transmitter locations

a single point estimate a third surface must be intersected. A third TDOA measurement could provide another surface, or if the transmitter is known to lie on the Earths surface, then a surface of the Earth constraint could be used. There are multiple techniques of obtaining 3 independent TDOA measurements. In order to obtain an instantaneous transmitter location estimate, only 3 TDOA measurements (from 4 satellite receivers) would be needed [3]. If the surface of the Earth constraint is used, only 2 TDOAs from 3 receivers would be necessary. Ho and Chan enumerate a method for conducting TDOA geolocation with multiple satellites [3].

# 2.3.2.2 Combined T/FDOA Measurement Model

While passive TDOA geolocation requires at least 3 satellites to obtain an instantaneous solution, combined T/FDOA geolocation can be implemented using a dual-satellite system [3]. Once each satellite receiver intercepts the transmitter's signal, the signal can be cross-linked to the reference satellite. Ho and Chan [23]

developed an algebraic solution for the dual-satellite T/FDOA as well as a general solution for T/FDOA when more than 2 satellite receivers are present.

As discussed in the previous section, each TDOA measurement produces a hyperboloid describing the transmitter's possible location. In the combined T/FDOA scenario, if the TDOA and FDOA measurements are taken simultaneously, the TDOA hyperboloid and FDOA revolution surface can be intersected with the Earth's surface to retrieve two possible transmitter solutions [3].

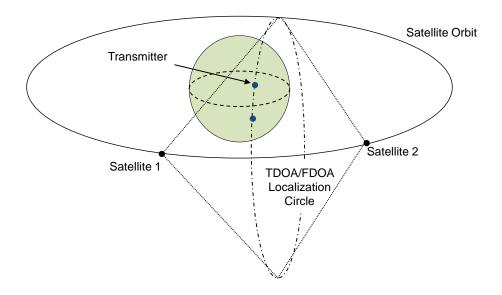


Figure 8. Sketch of the dual-satellite TDOA-FDOA combined geolocation principle [3]

The FDOA measurement equation can be obtained by taking the time derivative of the TDOA equation, Eq. 2.5.

$$\dot{\tau}_{i1} = \frac{\dot{r}_{i1}}{c} = \frac{\dot{\rho}_i - \dot{\rho}_1}{c} \qquad i = 2, 3..., S$$
 (2.6)

Here  $\dot{\rho}_i$  is the time derivative of  $\rho_i$  which is also the relative velocity of the  $i^{th}$  satellite

with respect to the transmitter in the direction of  $\rho_i$ . S is the number of SVs.

$$\dot{\rho}_i = \frac{\partial \rho_i}{\partial t} = \dot{\mathbf{s}}_i^T \frac{\boldsymbol{\rho}_i}{\rho_i} = (\dot{\mathbf{s}}_i - \dot{\mathbf{u}})^T \frac{(\mathbf{s}_i - \mathbf{u})}{\rho_i} \qquad i = 2, 3..., S$$
 (2.7)

The change rate of the TDOA  $\dot{\tau}$  can be obtained from frequency measurements. First consider the Doppler shift due to the relative velocity of satellite i with respect to the transmitter  $\mathbf{u}$  (assuming  $\dot{\mathbf{u}} = \mathbf{0}$ ), where  $f_c$  is the signal carrier frequency.

$$f_{di} = \frac{f_c}{c} \left[ \dot{\mathbf{s}}_i^T \frac{(\mathbf{s}_i - \mathbf{u})}{\rho_i} \right] = \frac{f_c}{c} \dot{\rho}_i$$
 (2.8)

Thus Eq. 2.6 can be rewritten in terms of the difference in Doppler shift between the  $i^{th}$  and reference satellite.

$$c\dot{\tau}_{i1} = \frac{c}{f_c} [f_{di} - f_{d1}]$$
 (2.9)

Thus in practice  $\dot{\tau}$  can be obtained by the difference in Doppler shift (also the difference in received frequency) nondimensionalized by the signal carrier frequency.

$$\dot{\tau}_{i1} = \frac{1}{f_c} \left[ f_{di} - f_{d1} \right] \tag{2.10}$$

Then Eq. 2.6 and Eq. 2.8 can be combined to get the range rate difference  $\dot{r}_{i1}$  between two receivers as a function of the FDOA f and the assumed, known carrier frequency  $f_c$ . This research will refer to the FDOA as both f (Hz) and  $\dot{\tau}$ , its nondimensionalized counterpart. The next section discusses how received signals are correlated to receive TDOA and FDOA measurements.

# 2.3.2.3 Complex Ambiguity Function

A suitable method for correlating signals to estimate the time and frequency difference was proposed by Stein [38]. Stein's method of joint time/frequency difference estimation is based off of the complex ambiguity function (CAF), seen in Eq. 2.11, which describes the correlation of two complex signals  $s_1(t)$  and  $s_2(t)$ .

$$A(\tau, f) = \int_0^T s_1(t) s_2^*(t+\tau) e^{-j2\pi f t} dt$$
 (2.11)

From this function, the differential time offset (DTO)  $\tau$  and differential frequency offset (DFO) f can be determined for a given time of integration T. The integration time refers to the length of the sample signal. Stein also found that greater integration time leads to greater measurement accuracy [38]. The CAF can be integrated and plotted over the integration time for two signals from the same source [3,38].

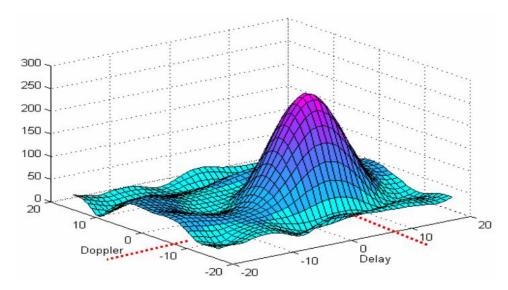


Figure 9. Example output of CAF surface [5]

A 2D search can be performed to obtain the TDOA and FDOA that corresponds to the peak CAF value. In order to ensure a distinguishable peak the input signals must have a SNR of at least 10 dB [38]. Guo et al. [3] discusses possible methods to increase computational efficiency of the cross ambiguity process and techniques to resolve signals from multiple sources.

# 2.3.2.4 Accuracy

The accuracy of the T/FDOA measurement depends on the integration time T, signal bandwidth  $B_s$ , and noise bandwidth  $B_n$  at receiver input [38]. Stein [38] states that "the estimates for this method [CAF] are unbiased and have a variance that achieves the Cramér-Rao bounds when any of several reasonable techniques is used for identifying the apparent location of the peak." The Cramér-Rao Lower Bound (CRLB) for the TDOA and FDOA measurements was stated by Stein [38] as 2.12 and 2.13, respectively.

$$\sigma_{\tau} = \frac{0.55}{B_s} \frac{1}{\sqrt{B_n T \gamma_e}} \tag{2.12}$$

$$\sigma_f = \frac{0.55}{T} \frac{1}{\sqrt{B_n T \gamma_e}} \tag{2.13}$$

This approximation is valid for a signal integrated over time T that has a rectangular signal power density spectrum over T. The effective input signal-to-noise ratio  $\gamma$  is a function of the input SNRs of the two receivers.

$$\frac{1}{\gamma_e} = \frac{1}{2} \left[ \frac{1}{\gamma_1} + \frac{1}{\gamma_2} + \frac{1}{\gamma_1 \gamma_2} \right] \tag{2.14}$$

The TDOA measurement error  $\sigma_{\tau}$  is inversely proportional to the signal bandwidth  $B_s$  and the FDOA measurement error  $\sigma_f$  is inversely proportional to the integration time T.

#### 2.3.2.5 Advantages and Disadvantages

While TDOA and FDOA geolocation involve the complexity of a satellite cluster, it has its advantages over AOA. The International Communications Union produced a report in 2011 comparing TDOA and AOA geolocation methods [39]. In the past

poor time synchronization has been a barrier to the employment of TDOA geolocation systems, but the invention of satellite navigation systems like GPS have made it possible to obtain more accurate time synchronization and as a result accurate TDOA measurements [39]. Compared with AOA, T/FDOA geolocation has simpler payload requirements. T/FDOA receivers may employ a single monopole or dipole (patch antenna) and they do not require test and calibration [39]. Furthermore, T/FDOA performs well for new and emerging signals that have complex modulations, wide bandwidths, and short durations, and the processing gain from correlation allows T/FDOA to pick up lower SNR signals [39]. On the other hand, T/FDOA has some disadvantages compared with AOA. Firstly, narrow-band signals are difficult to locate in a T/FDOA geolocation system [39]. As shown in Eq. 2.12 and Eq. 2.13, T/FDOA performance is sensitive to decreases in signal bandwidth. And as previously mentioned, high cross link data rate and time synchronization requirements are present in T/FDOA systems. One common characteristic of AOA and T/FDOA is that they perform better on higher SNR signals with longer integration time. The reader should see [3], [39], or [11] for a more detailed comparison.

#### 2.4 Initial Transmitter Localization

Initial Transmitter Localization (ITL) is defined by Sinclair and Lovell [40] as the "process of solving for the transmitter location using the minimum number of measurements." This research explores 6 geolocation algorithms: AOA, 3-SV TDOA (TDOA3), 4-SV TDOA (TDOA4), 2-SV T/FDOA (TFDOA2), 3-SV T/FDOA (TFDOA3), and 4-SV T/FDOA (TFDOA4). These 6 algorithms are seen in Table 2. Note that TFDOA3 and TFDOA4 are actually the same algorithm, the only difference is the number of SVs, or in other words number of inputs.

Each algorithm requires a different number and type of measurements to estimate

Table 2. Overview of ITL Methods Utilized

ITL Method	# Sats	Inputs	Tx Altitude	Iteration	Reference
AOA	1	$\alpha_s,  \epsilon_s,  \mathbf{s}_1$	Not Required	No	Bailey [4]
TDOA3	3	$ au,  \mathbf{s}_1,  \mathbf{s}_2, \ \mathbf{s}_3$	Required	No	Ho and Chan [37]
TDOA4	4	$ au, \mathbf{s}_1, \mathbf{s}_2, \\ \mathbf{s}_3, \mathbf{s}_4  ag{3}$	Not Required	No	Kulumani [24], Ho and Chan [37]
TFDOA2	2	$egin{array}{c}  au,\dot{ au},\mathbf{s}_1,\ \mathbf{s}_2,\dot{\mathbf{s}}_1,\dot{\mathbf{s}}_2 \end{array}$	Required	No	Ho and Chan [23]
TFDOA3	3	$\left  egin{array}{l}  au,\dot{ au},\mathbf{s}_i,\dot{\mathbf{s}}_i,\ \sigma_{dto},\sigma_{dfo} \end{array}  ight $	Preferred	Yes	Ho and Chan [23]
TFDOA4	4	$ au,  \dot{ au},  \mathbf{s}_i,  \dot{\mathbf{s}}_i, \\  au_{dto},  \sigma_{dfo}  ag{}$	Preferred	Yes	Ho and Chan [23]

a single initial transmitter location. These 6 ITL algorithms do not take into account measurement accuracy, and with the exception of AOA, they use the minimum number of measurements required to produce an ITL solution. These ITL algorithms are not necessarily the most computationally efficient and accurate. However they were accessible and popular in the geolocation literature [3, 4, 8, 23, 25, 41]. Table 2 is an overview of the ITL methods used.

ITL can be conducted for each set of measurements, and ITL solutions can be used to initialize other estimators, as discussed in Sec. 2.5 and 3.6.

# 2.4.1 Angle of Arrival

Once the azimuth  $\alpha$  and elevation  $\epsilon$  of arrival are measured, an LOB can be produced describing the RF signal path from the unknown transmitter to the receiver, ignoring atmospheric effects (Fig. 3). A single ITL solution can be achieved with a

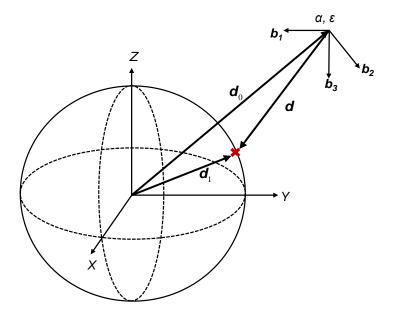


Figure 10. LOB can be represented in ECEF coordinates after being transformed from azimuth, elevation, and range in the body frame

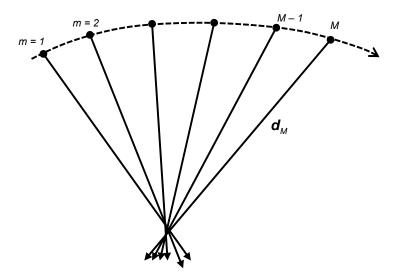


Figure 11. Multiple LOBs can be generated in a passs over the transmitter. Sparse LOB geometry leads to more accurate transmitter location estimates.

single measurement by intersecting the LOB  $\mathbf{d}$  with the Earth's surface, as seen in Fig. 97.

However, in a single pass over the transmitter of interest, the satellite can typically obtain multiple signal measurements, depending on the scenario. For each azimuth and elevation of arrival measured an LOB can be generated (Fig. 11). Recent AFT research [4,8,41] has shown how LS intersection can be performed to obtain a transmitter location  $\hat{\mathbf{u}}$  from M LOBs. (Sec. A.1) explains the process in detail.

#### 2.4.2 Time Difference of Arrival

There have been many different methods proposed to solve the nonlinear TDOA geolocation problem, including those which require multidimensional searches or iteration by linearization ( [42], [43]). However, Ho and Chan developed a closed-form solution to the 3 and 4 satellite TDOA geolocation problem [37]. Their algorithm is an algebraic solution which utilizes the transmitter altitude as a constraint to improve the location estimate. Both algorithms involve solving a polynomial equation to obtain multiple solutions for the range  $\rho_1$  from the reference satellite to the transmitter, then choosing the valid  $\rho_1$  to derive the transmitter location  $\hat{\mathbf{u}}$ . These algorithms are derived in [37] and [23]. Kulumani [24] adapted the TDOA4 algorithm found in [37] to avoid using Newton's method, which Ho and Chan proposed for applying the altitude constraint. The in-depth implementation of TDOA3 and TDOA4 for this research is described in App. A.2.

# 2.4.3 Time/Frequency Difference of Arrival

In 1997, Ho and Chan [23] developed an algebraic, closed-form solution to the combined TDOA and FDOA geolocation problem. Like the TDOA method discussed in Sec. 2.4.2, the T/FDOA algorithm utilizes the transmitter altitude as a constraint.

Ho and Chan [23] derive the T/FDOA solution for the case of 2 satellite geolocation as well as a general solution for 3 or more satellites. As with Ho and Chan's TDOA method [37], this T/FDOA method is more computationally efficient than an exhaustive grid search and does not face convergence issues present in iterative linearization methods [23]. Unlike the TDOA3, TDOA4, and TFDOA2, the T/FDOA solution presented in [23] for the general case  $(S \geq 3)$  involves iteration, as applying the altitude constraint requires a 1D Newton method search.

# 2.4.4 Altitude Assumption

All of the algorithms discussed incorporate some assumptions about the transmitter's position and velocity. The Ho and Chan algorithms utilized [23] are based on the assumption of a stationary transmitter ( $\dot{\mathbf{u}} = \mathbf{0}$ ) constrained to the Earth's surface ( $\mathbf{u}^T\mathbf{u} = r_e^2$ ). Ho et al. [44] propose a closed-form and computationally efficient solution for non-stationary transmitter localization. There are also variations of these TDOA and T/FDOA methods that relax the known altitude and stationary transmitter assumptions [25, 45–47].

As seen in Table 2, the transmitter altitude constraint is used by all algorithms except AOA and TDOA4 (Sec. 2.4.1). Therefore it is important to ask: which altitude should be chosen and how does error in the altitude chosen affect the geolocation estimate? Guo [3] and Ho and Chan [23] explore the ITL solution bias caused by altitude error. Ho and Chan [23] give an analytical ITL solution based on the World Geodetic System 84 Ellipsoid (WGS84) [48], and Guo [3] proposes spherical and Newton iteration methods to obtain the appropriate transmitter altitude  $r_e$  based on WGS84.

The spherical iteration method uses the TDOA or T/FDOA algebraic solution based on the spherical Earth model to obtain an initial transmitter location. Then

the latitude of estimate and the WGS84 model are used to obtain a more accurate altitude  $r_e$  [3]. However, using the WGS84 Ellipsoid still includes the assumption that the transmitter has zero altitude, which is not always true (See Sec. 2.6).

# 2.5 Estimation

Batch vs. Sequential Once geolocation measurements and corresponding ITL solutions are obtained as discussed in Sec. 2.4, further methods can be used to obtain a more optimal estimate based on the data set available. Sequential methods like the Kalman filter have been applied to geolocation [49,50], but batch estimation is utilized in this research to maintain continuity with recent AFIT research [4,10]. Batch estimation was determined to be sufficient to post-process M measurements taken during access to the transmitter(s) and down-link geolocation coordinates [10].

**Probability Density Function** Each independent measurement set m taken instantaneously at 1-4 satellites is assumed to be normally distributed with variance  $\sigma_m^2$  due to instrument and measurement algorithm (CAF, MUSIC) errors. Let  $\tilde{\mathbf{m}}$  be an arbitrary measurement vector containing M real measurements taken over a pass.

$$\tilde{\mathbf{m}} = \mathbf{m}(\mathbf{u}) + \mathbf{e}_m$$

$$\mathbf{e}_m \equiv [e_1, ..., e_M]^T \qquad e_m \sim N(0, \sigma_m)$$
(2.15)

In Sec. 2.3 the measurement models describe how  $\mathbf{m}$  is a nonlinear function of the transmitter location  $\mathbf{u}$ .

$$\mathbf{m}(\mathbf{u}) = \begin{bmatrix} m_1 & \dots & m_M \end{bmatrix}^T = \begin{bmatrix} \alpha_1 & \epsilon_1 & \dots & \alpha_M & \epsilon_M \end{bmatrix}^T (AOA)$$

$$= \begin{bmatrix} \tau_1 & \tau_2 & \dots & \tau_M \end{bmatrix}^T (TDOA3)$$

$$= \begin{bmatrix} \tau_1 & \dot{\tau}_1 & \dots & \tau_M & \dot{\tau}_M \end{bmatrix}^T (TFDOA2)$$
(2.16)

Observe that  $\mathbf{m}(\mathbf{u})$  is the expected value of  $\tilde{\mathbf{m}}$ .

$$E[\tilde{\mathbf{m}}] = E[\mathbf{m}(\mathbf{u})] + E[\mathbf{e}_m] = \mathbf{m}(\mathbf{u})$$
(2.17)

The joint probability density function (PDF) shown in Eq. 2.18 describes the probability of having obtained the M measurements given the transmitter location  $\mathbf{u}$  [51].

$$f(\tilde{\mathbf{m}}|\mathbf{u}) = (2\pi)^{-M/2} \left[ \prod_{i=1}^{M} \sigma_i^{-1} \right] \exp \left\{ -\sum_{i=1}^{M} \frac{\left[\tilde{m}_i - m(\mathbf{u})\right]^2}{2\sigma_i^2} \right\}$$
(2.18)

#### 2.5.1 Principle of Maximum Likelihood

The optimal estimate  $\hat{\mathbf{u}}$  is the one that maximizes the PDF in Eq. 2.18, or in other words, the one that maximizes the probability of having obtained the actual measurements. This concept is called the Principle of Maximum Likelihood [51]. Maximum Likelihood Estimation (MLE), introduced and popularized by R. A. Fisher in 1912, is the most widely used method of estimation in statistics [52]. Bailey [4] utilized MLE for the single-satellite AOA geolocation problem. Ren et al. [53] and Hale [15] show how MLE can be applied to the T/FDOA problem. This  $\hat{\mathbf{u}}_{MLE}$  is unconstrained, meaning it does not constrain the estimate to the Earth's surface. Cao et al. [46] utilize a constrained MLE algorithm for T/FDOA which minimizes

the receiver location and measurement error. This research applies an unconstrained MLE to AOA, TDOA, and T/FDOA geolocation which minimizes the measurement error, as done by Bailey [4], Ren et al. [53] and Hale [15].

To understand how the ML estimate is conceived, first consider the conditional probability density function  $f(\tilde{\mathbf{m}}|\mathbf{u})$  from Eq. 2.18.  $f(\tilde{\mathbf{m}}|\mathbf{u})$  is maximized when the magnitude of the term within the exponential operator is minimized.

$$\hat{\mathbf{u}}_{MLE} = \arg\max_{\mathbf{u}} \left\{ f(\tilde{\mathbf{m}}|\mathbf{u}) \right\} = \arg\min_{\mathbf{u}} \left\{ \sum_{i=1}^{M} \frac{(\tilde{m}_i - m(\mathbf{u}))^2}{\sigma_i^2} \right\}$$
(2.19)

This equation for the ML estimator can be rewritten in matrix form.

$$\hat{\mathbf{u}}_{MLE} = \underset{\mathbf{u}}{\operatorname{arg min}} \left\{ [\tilde{\mathbf{m}} - \mathbf{m}(\mathbf{u})]^T \mathbf{Q}_m^{-1} [\tilde{\mathbf{m}} - \mathbf{m}(\mathbf{u})] \right\}$$

$$\mathbf{Q}_m \equiv \operatorname{diag}[\sigma_1^2, ..., \sigma_M^2]$$
(2.20)

Due to the nonlinearity of  $\mathbf{m}(\mathbf{u})$  and the weighting matrix  $\mathbf{Q}_m^{-1}$ , Eq. 2.20 is called a nonlinear weighted least squares minimization problem, which is an extension of basic least squares estimation.

#### 2.5.2 Least Squares Estimation

The method of least squares involves minimizing the squared differences between the observed measurements and the expected values [54]. The least squares estimate  $\hat{\mathbf{u}}_{LS}$  can be defined as the value which minimizes Eq. 2.21.

$$\sum_{i=1}^{M} \left[ \tilde{m}_i - m(\mathbf{u}) \right]^2 \tag{2.21}$$

**Linear Least Squares** If the function  $m(\mathbf{u})$  is linear, then there is a matrix **A** that maps  $\mathbf{u}$  into the measurement space, and the new least squares estimate can

be defined as

$$\hat{\mathbf{u}}_{LS} = \underset{\mathbf{u}}{\operatorname{arg min}} \left\{ \sum_{i=1}^{M} (\tilde{m}_i - \mathbf{A}\mathbf{u})^2 \right\}$$
 (2.22)

Strang [55] derives the solution for this linear least squares problem Eq. 2.23.  $(\mathbf{A}^T \mathbf{A})^{-1} \mathbf{A}^T$  is known as the Moore-Penrose pseudoinverse of  $\mathbf{A}$  [55].

$$\hat{\mathbf{u}}_{LS} = (\mathbf{A}^T \mathbf{A})^{-1} \mathbf{A}^T \tilde{\mathbf{m}}$$
 (2.23)

Weighted Least Squares In reality, not all measurements have the same amount of uncertainty. In the linear least squares method shown above, each measurement carries an equal weight. Weighted least squares (WLS) attempts to weight each measurement according to its corresponding variance  $\sigma_m^2$  [51]. The weighted least squares estimator is given by [54]

$$\hat{\mathbf{u}}_{WLS} = \arg\min_{\mathbf{u}} \left\{ \sum_{i=1}^{M} \frac{(\tilde{m}_i - \mathbf{A}\mathbf{u})^2}{\sigma_i^2} \right\}$$
 (2.24)

Equation Eq. 2.24 can be written in matrix form, similar to Eq. 2.20.

$$\hat{\mathbf{u}}_{WLS} = \arg\min_{x} \left\{ \left[ \tilde{\mathbf{m}} - \mathbf{A} \mathbf{u} \right]^{T} \mathbf{Q}_{m}^{-1} \left[ \tilde{\mathbf{m}} - \mathbf{A} \mathbf{u} \right] \right\}$$
(2.25)

The solution to the weighted least squares problem Eq. 2.25 is [56]

$$\hat{\mathbf{u}}_{WLS} = (\mathbf{A}^T \mathbf{Q}_m^{-1} \mathbf{A})^{-1} \mathbf{A}^T \mathbf{Q}_m^{-1} \tilde{\mathbf{m}}$$
(2.26)

Nonlinear Weighted Least Squares The only difference between weighted least squares and nonlinear weighted least squares (NWLS) is that the function  $m(\mathbf{u})$  is nonlinear, thus

$$m(\mathbf{u}) \neq \mathbf{A}\mathbf{u} \tag{2.27}$$

Therefore Eq. 2.24 becomes

$$\hat{\mathbf{u}}_{NWLS} = \arg\min_{\mathbf{u}} \left\{ \sum_{i=1}^{M} \frac{\left[\tilde{m}_{i} - m(\mathbf{u})\right]^{2}}{\sigma_{i}^{2}} \right\}$$
(2.28)

which resembles the maximum likelihood estimate shown in Eq. 2.19.

# 2.5.3 Gauss-Newton Algorithm

The Gauss-Newton algorithm is an iterative method useful for solving the non-linear least squares problem shown in Eqs. 2.19 and 2.28 [57]. First note that the nonlinear function  $m(\mathbf{u})$  can be approximated with the first-order Taylor series, where  $\hat{\mathbf{u}}_k$  is a known value close to  $\mathbf{u}$ .

$$m(\mathbf{u}) \approx m(\hat{\mathbf{u}}_k) + m'(\hat{\mathbf{u}}_k)(\mathbf{u} - \hat{\mathbf{u}}_k)$$
 (2.29)

If the difference between  $\mathbf{u}$  and  $\hat{\mathbf{u}}_k$  is sufficiently small, then the first order approximate is accurate. In the NWLS problem,  $\mathbf{u}$  is unknown. The Gauss-Newton method involves redefining the unknown  $\mathbf{u}$  as the new estimate  $\hat{\mathbf{u}}_{k+1}$  and iterating to a specified tolerance [57].

$$m(\mathbf{u}_{k+1}) \approx m(\hat{\mathbf{u}}_k) + m'(\hat{\mathbf{u}}_k)(\hat{\mathbf{u}}_{k+1} - \hat{\mathbf{u}}_k)$$

$$||\hat{\mathbf{u}}_{k+1} - \hat{\mathbf{u}}_k|| \le tol$$

$$m'(\mathbf{u}) \equiv \frac{\partial m}{\partial \mathbf{u}} = \mathbf{J}_m(\mathbf{u}) = \mathbf{J}$$
(2.30)

J describes how the true measurement changes with respect to change in transmitter location. The Gauss-Newton method is capable of quadratic convergence in the best case, given an initial condition  $\hat{\mathbf{u}}_0$  that is relatively close to the truth. If Eq. 2.29 is converted to vector form and substituted into Eq. 2.20 for  $\mathbf{m}(\mathbf{u})$  then the expanded

equation is

$$\hat{\mathbf{u}}_{MLE} = \arg\min_{\mathbf{u}} \left\{ \left[ \tilde{\mathbf{m}} - \left( \mathbf{m}(\hat{\mathbf{u}}_k) + \mathbf{J}(\mathbf{u} - \hat{\mathbf{u}}_k) \right) \right]^T \mathbf{Q}_m^{-1} \left[ \tilde{\mathbf{m}} - \left( \mathbf{m}(\hat{\mathbf{u}}_k) + \mathbf{J}(\mathbf{u} - \hat{\mathbf{u}}_k) \right) \right] \right\}$$
(2.31)

To simplify further,

$$\hat{\mathbf{u}}_{MLE} = \arg\min_{\mathbf{u}} \left\{ \left[ \tilde{\mathbf{m}} - \mathbf{m}(\hat{\mathbf{u}}_k) + \mathbf{J}\hat{\mathbf{u}}_k - \mathbf{J}\mathbf{u} \right]^T \mathbf{Q}_m^{-1} \left[ \tilde{\mathbf{m}} - \mathbf{m}(\hat{\mathbf{u}}_k) + \mathbf{J}\hat{\mathbf{u}}_k - \mathbf{J}\mathbf{u} \right] \right\}$$
(2.32)

For simplicity combine known parameters into y:

$$\mathbf{y} = \tilde{\mathbf{m}} - \mathbf{m}(\hat{\mathbf{u}}_k) + \mathbf{J}\hat{\mathbf{u}}_k \tag{2.33}$$

$$\hat{\mathbf{u}}_{MLE} = \arg\min_{\mathbf{u}} \left\{ \left[ \mathbf{y} - \mathbf{J} \mathbf{u} \right]^T \mathbf{Q}_m^{-1} \left[ \mathbf{y} - \mathbf{J} \mathbf{u} \right] \right\}$$
(2.34)

This equation resembles the weighted linear least squares problem (Eq. 2.25) whose solution (Eq. 2.26) can be rewritten as [56]

$$\hat{\mathbf{u}}_{MLE} = (\mathbf{J}^T \mathbf{Q}_m^{-1} \mathbf{J})^{-1} \mathbf{J}^T \mathbf{Q}_m^{-1} \mathbf{y}$$
(2.35)

Now  $\hat{\mathbf{u}}_{MLE}$  is conveniently described by known parameters.  $\hat{\mathbf{u}}_{MLE}$  can be defined as the updated estimate  $\hat{\mathbf{u}}_{k+1}$ , and the new iterative equation with  $\mathbf{y}$  expanded becomes

$$\hat{\mathbf{u}}_{k+1} = (\mathbf{J}^T \mathbf{Q}_m^{-1} \mathbf{J})^{-1} \mathbf{J}^T \mathbf{Q}_m^{-1} (\tilde{\mathbf{m}} - \mathbf{m}(\hat{\mathbf{u}}_k) + \mathbf{J} \hat{\mathbf{u}}_k)$$
(2.36)

After multiplying the terms out and simplifying, the final iterative equation is

$$\hat{\mathbf{u}}_{k+1} = \hat{\mathbf{u}}_k + (\mathbf{J}^T \mathbf{Q}_m^{-1} \mathbf{J})^{-1} \mathbf{J}^T \mathbf{Q}_m^{-1} [\tilde{\mathbf{m}} - \mathbf{m}(\hat{\mathbf{u}}_k)]$$

$$||\hat{\mathbf{u}}_{k+1} - \hat{\mathbf{u}}_k|| < tol$$
(2.37)

The final  $\hat{\mathbf{u}}_{k+1}$  after convergence is the estimate for the transmitter location that minimizes the collective geolocation measurement error.

#### 2.5.4 Estimate Confidence

For Gaussian distributed estimates, the covariance or confidence is described as the inverse of the Fisher Information Matrix  $\mathbf{F}$  [58].

$$\mathbf{C}_{MLE} = \mathbf{F}^{-1} = (\mathbf{J}^T \mathbf{Q}_m^{-1} \mathbf{J})^{-1}$$
(2.38)

The confidence region can be expressed graphically as an ellipsoid for the 3D problem. The ellipsoid is centered at  $\hat{\mathbf{u}}_{MLE}$ . The eigenvectors of  $\mathbf{C}_{MLE}$  determine the direction of the ellipsoid axes and the eigenvalues  $\lambda_i$  represent the lengths of the axes.

It is important to achieve a desired confidence level for  $\hat{\mathbf{u}}_{MLE}$ , and the ellipsoid should be scaled appropriately to reflect that level of confidence. The scale factor  $\chi$  is multiplied by the square of the eigenvalues of  $\mathbf{C}_{MLE}$  to appropriately resize  $\mathbf{C}_{MLE}$ . This can be expressed as

$$\lambda_i' = \chi^2 \lambda_i \tag{2.39}$$

If the number of degrees of freedom and the desired level of confidence is known, a Chi-squared distribution can be used to calculate  $\chi^2$ . In the 3D case, to achieve 95% confidence that  $\hat{\mathbf{u}}_{MLE}$  is within the ellipsoid,  $\chi^2 = 7.815$ .

#### 2.6 Digital Elevation Models

Finally, accurate geolocation requires a robust definition of the surface of the Earth. The Spherical Earth and WGS84 Ellipsoid models were discussed in Sec. 2.4.4. The last type of surface used in this research, Digital Elevation Models (DEM), is discussed in this section. Digital Elevation Model (DEM) refers to any digital terrain

or surface model, regardless of the complexity. Thanks to modern geoscience, more accurate DEMs have been produced, benefiting a variety of civilian and military sectors [59].

Shuttle Radar Topography Mission The first near-global set of land elevations was enabled by the Shuttle Radar Topography Mission (SRTM) [60]. SRTM [59], a joint effort of NASA, the National Geospatial-Intelligence Agency (NGA), and the Italian and German Space Agencies, was an 11-day mission flown aboard the space shuttle Endeavor in February 2000 that used radar to gather information about the Earth's environment [59,60]. SRTM "produced the most complete, highest-resolution digital elevation model of the Earth" [59].

Digital Terrain Elevation Data The NGA used data obtained by SRTM to develop a standard of digital datasets referred to as Digital Terrain Elevation Data (DTED®) [61]. There are 3 levels of DTED resolution: level 0, 1, and 2. The DTED resolution is defined by the latitudinal and longitudinal area occupied by each elevation post. The National Imagery and Mapping Agency's DTED performance specification [9] defined the resolution of each DTED level.

Table 3. DTED Post Sizes (Adapted from [8,9])

Position on Earth	DTED	Level 0	DTED	Level 1	DTED	Level 2
1 Osition on Earth	Post Size (arc-seconds, 1 arc-second $\approx 30 \text{ m}$ )					
Latitude N/S (deg)	lat	lon	lat	lon	lat	lon
0-50	30	30	3	3	1	1
50-70	30	60	3	6	1	2
70-75	30	90	3	9	1	3
75-80	30	120	3	12	1	4
80-90	30	180	3	18	1	6

There are various methods of obtaining DEMs. The U.S. Geological Survey

(USGS) provides 3 arc-second and 1 arc-second SRTM data which can be downloaded in DTED format [62]. These datasets are referred to as DTED1 and DTED2 throughout this thesis.

Global Multi-resolution Terrain Elevation Data 2010 (GMTED2010) model, produced jointly NGA and USGS, used the best available data from various sources to produce elevation data at three different resolutions of 30, 15, and 7.5 arc-seconds (about 1000, 500, 250 meters) [63]. GMTED2010 draws from DTED, USGS DEMs, and even international data sources to provide a worldwide surface model. The mean elevations contained in GMTED2010 have a global root mean square error (RMSE) of 26.72 m [63].

**DEM Reference** For each of these products, the digital elevations are vertical heights H in meters referenced from the Earth Gravitational Model (EGM96) [6]. The EGM96, or Geoid, was a DEM developed in 1996 that is used in most military simulations as a reference for zero elevation or mean sea level (MSL) [6]. The Geoid differs from the WGS84 Ellipsoid by as much as 100 m [6]. While vertical DEM datum are referenced to the Geoid, in most advanced DEMs the elevation posts are horizontally referenced by the WGS84 geodetic latitude and longitude.

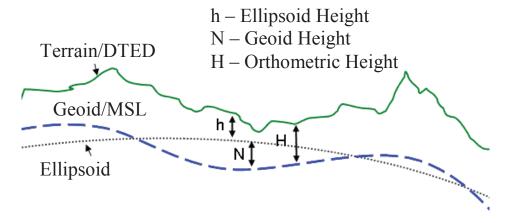


Figure 12. The geoid, a reference ellipsoid, and terrain [6]

In practice, elevation data can be converted to WGS84 Ellipsoid height for altitude calculations. For each post, the elevation H can be added to the Geoid height N at the post's latitude and longitude, which typically requires interpolation.

$$h = H + N \tag{2.40}$$

**DEM Application** Schmidt [8] used DTED1 and DTED2 to further refine ITL solutions obtained via TDOA and AOA geolocation algorithms. He utilized a grid search to choose an elevation post for the geolocation estimate based on figures of merit [8]. This research will utilize 30-arcsecond GMTED2010 in ITL calculations. Furthermore, USGS 3-arcsecond SRTM data (DTED1) will be used to execute a grid search similar to that in [8] to obtain better accuracy.

# 2.7 Summary

This chapter has described the current progress in the space-based RF geolocation effort and surveyed the principles behind the geolocation problem. These principles included CubeSat design limitations, formation flying, signal measurement, initial transmitter localization (ITL), estimation, estimate fusion, and application of digital elevation models. The next chapter, Methodology, will explain how these principles are applied to accomplish the geolocation analysis and answer the research questions.

# 3. Methodology

The primary method of answering the research question was developing an end-toend simulation of 1-4 CubeSats geolocating a fixed-site Air Route Surveillance Radar. This chapter describes the methods and tools used to produce the simulation. Secondly, the chapter explains the measures of performance (MOPs) which are numerical quantities used in Chapters 4 and 5 to assess, compare and contrast results.

#### 3.1 Overview

An overview of the geolocation simulation can be seen in Fig. 13. The structure of this chapter will resemble the flow of this diagram.

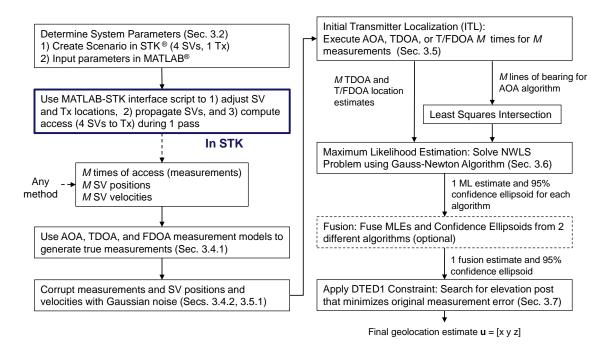


Figure 13. Overview of STK-MATLAB Geolocation Simulation

# 3.2 System Parameters

This section discusses the input parameters (Table 4) needed for the geolocation simulation, some of which remain constant and others of which are varied, depending on the scenario.

Table 4. Simulation Input Parameters

Orbit and Cluster	SV Payload		
Chief altitude (km)	Receiver Gain (dB)		
Chief inclination (deg)	Integration Time (s)		
Chief longitude of the ascending node (deg)	# Samples per collect		
Chief argument of latitude (deg)			
Chief orbit epoch (date/time)			
Baseline distance (km)	Error $(1-\sigma)$		
	Angle measurement (deg)		
<u>Transmitter</u>	DTO measurement (s)		
Latitude (deg)	DFO measurement (Hz)		
Longitude (deg)	Absolute SV Position (m)		
Altitude (m)	Absolute SV Velocity (m/s)		
Transmit Frequency (Hz)	Relative SV Position (m)		
Transmit Power (W)	Relative SV Velocity (m/s)		
Transmit Gain (dB)	SV attitude knowledge (deg)		
Transmit Bandwidth (Hz)	Timing synchronization (s)		
Beam Pattern (Sweep, Constraints)	Frequency synchronization (Hz)		

#### 3.2.1 Transmitter Characterization

Type An RF transmitter with an isotropic beam pattern was primarily utilized throughout this research. So it was assumed that whenever the SVs were within line of sight of the transmitter a signal could be collected, with a minimum elevation angle of 5°. A signal collect is defined as a discrete instance where all SVs in the cluster receive the same signal of interest. So for a 3-SV TDOA system, there

are M discrete collects for a single pass, and each collect includes 2 time difference measurements ( $\tau_{21}, \tau_{31}$ ). An isotropic transmitter was chosen for generality, not for realism. In Chapter 5, where the system level performance is analyzed, a radar signal of interest was also simulated to add a realistic scenario and observe how much the radar beam constraints affected signal collection and subsequently geolocation accuracy. The radar simulated was an Air Route Surveillance Radar Series 4 (ARSR-4). Its properties are seen in Table 5. The isotropic transmitter was assumed to have the same transmit frequency as in Table 5, but as previously discussed, there were no beam constraints.

Table 5. ARSR-4 Signal Characteristics [10]

Parameter	Value	Unit	
Transmit Frequency	1315	MHz	
Bandwidth	100	MHz	
Transmit Power	6.5	kW	
Transmit Gain	45	dB	
Azimuth Spinning	5	RPM	
Beam Elevation	5-35	deg	
Beam Width	1.5	deg	

**Location** The simulated transmitter locations were arbitrary, but locations with varied latitude and altitude were chosen so the effects of the oblateness of the Earth and the elevation of the transmitter could be studied. Furthermore, locations in the center of  $1 \times 1^{\circ}$  DTED grids were chosen so that only one DTED file would be required for analysis.

Altitude The altitude for each of the transmitters was defined from the level 2 DTED obtained from USGS (See App. B.1). While the DTED2 surface does not

Table 6. Transmitter Locations

Tx	Latitude (deg)	Longitude (deg)	Altitude	
	Latitude (deg)	Longitude (deg)	(WGS84 height, m)	
1	0.5011	100.4989	104.29	
2	15.5011	100.4989	25.80	
3	30.5011	100.4989	3968.68	
4	45.5011	100.4989	1386.62	
5	58.5011	100.4989	173.00	

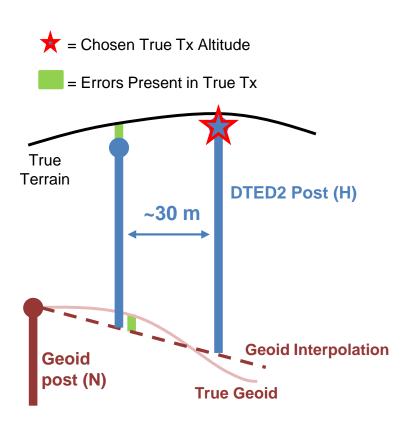


Figure 14. Defining the true transmitter altitude using DTED2 posts

represent truth, it was high enough resolution (30 m) for this research.

A single post near the center of the  $1 \times 1^{\circ}$  DTED2 grid was chosen, and the latitude and longitude of that post was used for the transmitter. Using the DTED2 post altitude was preferred over choosing a latitude and longitude and interpolating the DTED2 surface for altitude. Such interpolation could lead to additional inaccuracy depending on the interpolation method, as seen in Fig. 14. Ultimately, the DTED2 post elevation error and Geoid interpolation error were the only uncertainties present in the chosen transmitter altitudes.

#### 3.2.2 Orbit Selection

Some, but not all of the orbit design choices were relevant to this research, so selections were made that would maintain continuity with AFIT SV design research. For this analysis the simulation only runs for a single pass, therefore drag, perturbations, and multi-pass geolocation are not considered. However, the geolocation simulation can be initialized with any set of measurements, meaning other mission orbits and multiple passes can be used as long as measurements and corresponding receiver positions and velocities are obtained.

Number of SVs The number of SVs influences the type of ITL algorithm that can be used to geolocate the transmitter. A trade space of 1-4 SVs was chosen since beyond 4 SVs there is no variation in the algorithms chosen, and it is assumed more measurements implemented with the same algorithms would produce a more accurate ITL solution.

Altitude and Inclination CubeSats tend to operate in LEO due to payload size, weight, and power limitations, as well as radiation threats posed by the Van Allen belts [64]. Thus an upper bound of 1000 km was chosen for the trade space of SV

altitudes. The lowest altitude explored was 350 km due to the high amount of  $\Delta V$  required for station-keeping below that altitude [64]. The default altitude was set to 500 km to maintain continuity with AFIT SV design research. All orbits were circular, and while the inclination was arbitrary, 64° was chosen for continuity with recent AFIT research.

Pass Geometry A pass is defined in this research as the time during which the SVs (or SV) are within line of sight of the transmitter. A pass begins when the SVs rise above the horizon and ends when the SVs fall below the horizon, with an assumed minimum elevation angle of  $5^{\circ}$ . During a pass M signal collects are obtained by the SV(s). This research assumes that only a single pass is achievable for a given transmitter, meaning the M collects from that pass are the only data used for on-board geolocation.

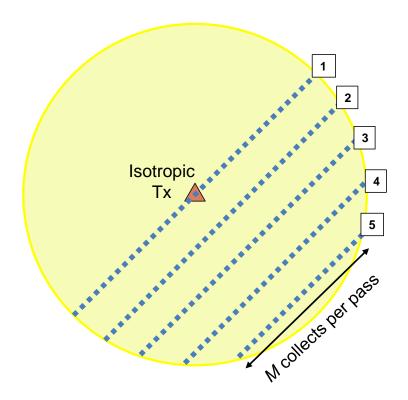


Figure 15. SV Pass Geometry for Isotropic Transmitter

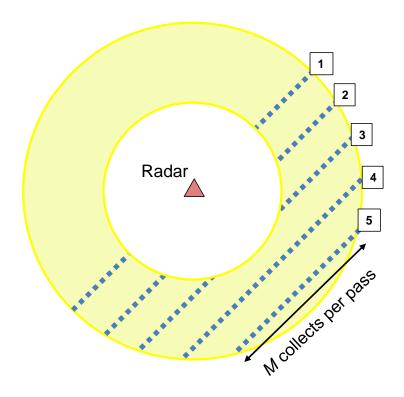


Figure 16. SV Pass Geometry for Radar

While it was assumed only one pass over the unknown transmitter was achievable, 5 different pass types were chosen to observe the effect of collection geometry on geolocation accuracy. These passes ranged from overhead passes (1) to passes closer to the horizon (5). These passes were simulated independently, the M signal collects did not accumulate for the 5 passes. Fig. 15 shows the pass types simulated for the isotropic transmitter and Figure 16 contains the pass types for the sweeping radar. Both figures display the SV ground tracks for each pass.

# 3.2.3 Cluster Design

The goal of cluster design was to not to optimize cluster geometry for TDOA and FDOA collection, but rather to create a few baseline geometries useful for comparison.

Table 7. Chief SV Orbital Elements for All Passes

Radar	Pass Type	LAN (deg)	Arg. Lat (deg)
	1	100.1	0.9
	2	105	0.9
1	3	109	0.9
	4	113	0.9
	5	117	0.9
	1	93.9	16.6
	2	99	16.6
2	3	103	16.6
	4	107	16.6
	5	111	16.6
	1	86.1	34.5
	2	91.2	34.5
3	3	96.2	34.5
	4	101.2	34.5
	5	106.2	34.5
	1	74.6	52.6
	2	79.4	52.6
4	3	85.4	52.6
	4	91.4	52.6
	5	97.4	52.6
	1	48.8	74.7
	2	58.8	74.7
5	3	68.8	74.7
	4	78.8	74.7
	5	88.8	74.7

Constants: Alt. 500 km, Inc.  $64^{\circ}$  ( [10]), Orbit epoch at 1 Jan 2017 at 12:00:00 UTC

Formation Type For the duration of a pass over the transmitter, geometric diversity of the cluster is optimal for accurate TDOA and T/FDOA geolocation estimates [14]. Though some geometrically diverse formations like Natural Motion Circumnavigation (NMC) [14] exist, a simpler formation similar to Non-Coplanar Oscillator was chosen. The formation used in this research (Fig. 17) features the first two SVs in the same plane and the third and fourth SVs in a plane with a slightly different inclination and/or right ascension of the ascending node (RAAN).

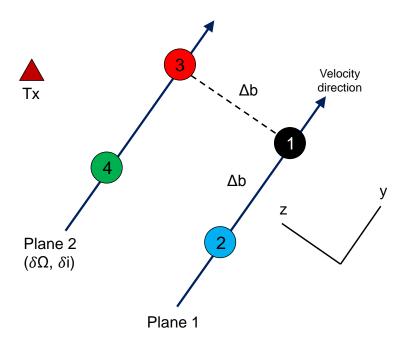


Figure 17. Cluster formation in HCW frame (not to scale)

Baseline Distance The last element of the cluster design is baseline distance, or separation between two SVs. In order to keep cluster geometry as constant as possible across different passes, a fixed separation distance was chosen for each scenario. Large baselines can make it difficult for all SVs to collect the same RF signal, depending on the transmitter beam pattern. For the chosen spinning ARSR-4 radar with beam azimuth of 1.5°, a baseline of greater than 15 km would make it

highly unlikely for all 4 SVs to collect the same radar pulse. It's also important to reiterate that this research assumes all the SVs have hardware capable of detecting and correlating the transmitter signal.

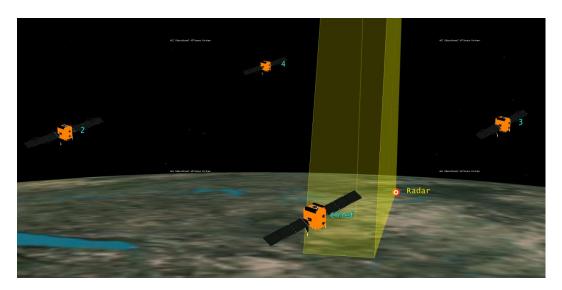


Figure 18. 4 SVs orbiting within range of a sweeping radar with finite beamwidth

On the other hand, small baseline distance is unfavorable for TDOA and T/FDOA geolocation accuracy. The trade space for baseline distance was chosen to be between 1 km and 30 km, and the default was chosen as 15 km.

Cluster Formation The goal was to standardize the cluster formation as much as possible, including baseline and geometry. Thus for each pass, a reference time  $t_0$  was defined as the middle of a pass, or when the sub-satellite point was closest to the target transmitter. At that reference point the cluster was formulated with the baseline and geometry seen in Fig. 17, assuming that variations to the geometry would be minimal throughout the duration of a pass. For each pass simulated the relative geometry was plotted in the HCW frame to observe how it changed (Fig. 19).

- 1. Determine the baseline distance  $\Delta b$  for the scenario.
- 2. Set Chief SV orbit for the current pass using the parameters from Sec. 3.2.2.

3. Define SV 2 in the same plane as the chief but following at the baseline distance (leader-follower). This results only in a change of phase  $\delta\theta$ , where a is the semimajor axis of the chief.

$$\delta\theta = \frac{\Delta b}{a_1} \tag{3.1}$$

4. Define SV 3 in a separate plane from the chief. Use the approximation of the HCW equation approximations (Eq. 2.2) [2] to space SV 3  $\Delta b$  in the cross-track direction z at the reference time  $t_0$ .

$$x = \delta r \tag{3.2}$$

$$y = r_1(\delta\theta + \delta\Omega\cos i_1) \tag{3.3}$$

$$z = r_1(\delta i \sin \theta_1 - \delta \Omega \sin i_1 \cos \theta_1) \tag{3.4}$$

- (a) For SV 3 the relative radial and in-track components are set to 0 (x = y = 0), and only the cross-track z is varied.
- (b) Set  $z = \Delta b$ . Then for an array of possible  $\delta\Omega$ , use Eq. 3.4 to find a corresponding array of  $\delta i$ .
- (c) Choose the  $\delta\Omega \delta i$  pairing which minimizes baseline change over a pass. This usually translates to smaller  $\delta i$  at lower latitudes and larger  $\delta i$  at higher latitudes.
- (d) Then solve Eq. 3.3 for  $\delta\theta$  with the new  $\delta\Omega$  and y=0.
- 5. Define SV 4 as in Step 3, where SVs 3-4 are in a leader follower formation analogous to SVs 1-2.

The relative SV geometry was plotted in the Hill frame to observe how it deviated over the course of a pass (Fig. 19). Similarly, data about the baseline between each

of the SVs for each pass was obtained (Table 8).

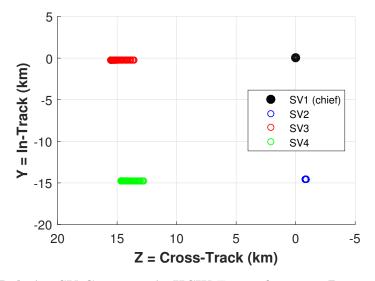


Figure 19. Relative SV Geometry in HCW Frame for Tx 1, Pass 1, Baseline 15km

It is important to note that in Fig. 19, although SVs 1 and 2 are coplanar, there is still some nonzero cross-track offset for SV 2. The actual SV2 cross-track offset in Fig. 19 is -15m. After further investigation it was determined that the slight offset of the orbital planes is due to the imprecision of the MATLAB Object Model code used to establish the SV orbits in STK. If the orbits were manually defined in STK there would be no offset present.

### 3.3 Propagation

Systems Tool Kit The propagation of the SV orbits was executed in Systems Tool Kit (STK), an application developed by Analytical Graphics, Inc. Other tools including MATLAB can be used for the orbit propagation component of the simulation, however STK was used for this research to maintain continuity with the AFIT SV design sequence and to make geolocation scenario changes simpler due to STK's graphical user interface.

Table 8. Baseline Data for All Passes ( $\Delta b = 15km$ )

$\mathbf{T}\mathbf{x}$	Pass	SV 2 Baseline		SV 3 Baseline		SV 4 Baseline	
		Mean	$\sigma$	Mean	$\sigma$	Mean	$\sigma$
1	1	14.592	0.002	15.032	1.129	20.477	0.749
	2	14.592	0.002	15.098	0.938	20.522	0.626
	3	14.593	0.002	15.155	0.782	20.560	0.523
	4	14.593	0.002	15.248	0.573	20.621	0.385
	5	14.593	0.002	15.333	0.394	20.679	0.261
	1	14.590	0.007	14.963	3.128	20.497	2.033
	2	14.591	0.006	15.184	2.853	20.639	1.873
2	3	14.591	0.006	15.340	2.576	20.739	1.706
	4	14.592	0.005	15.531	2.233	20.862	1.493
	5	14.592	0.004	15.757	1.741	21.009	1.179
	1	14.585	0.011	15.072	6.098	20.772	3.978
3	2	14.585	0.011	15.507	5.769	21.049	3.828
	3	14.586	0.010	15.952	5.256	21.334	3.551
	4	14.587	0.009	16.238	4.674	21.514	3.199
	5	14.588	0.007	16.721	3.680	21.828	2.570
	1	14.577	0.011	15.137	11.669	21.355	7.567
	2	14.578	0.012	15.766	11.487	21.751	7.629
4	3	14.579	0.011	16.757	10.826	22.375	7.460
	4	14.580	0.011	17.729	9.821	22.999	7.001
	5	14.580	0.009	18.450	8.226	23.451	6.022
	1	14.570	0.007	14.381	3.933	20.315	2.974
5	2	14.571	0.008	13.773	4.331	19.868	3.150
	3	14.572	0.009	13.092	4.695	19.388	3.273
	4	14.573	0.009	12.580	4.670	19.026	3.158
	5	14.574	0.008	12.224	4.177	18.760	2.775

Note: All baseline means and std. devs. given in km

Implementation The purpose of using STK was to generate M SV positions and velocities Eq. 3.5 during a single pass over the transmitter. Note that the MATLAB portion of the geolocation simulation only requires the inputs in Eq. 3.5 during access to the transmitter, so the method of obtaining these inputs is irrelevant. One could generate their own  $\mathbf{S}_{M\times 3}$  and transmitter characteristics and move on to Sec. 3.4.

$$\mathbf{S}_{M\times3} = \begin{bmatrix} \mathbf{s}_1 \\ \vdots \\ \mathbf{s}_M \end{bmatrix} \qquad \dot{\mathbf{S}}_{M\times3} = \begin{bmatrix} \dot{\mathbf{s}}_1 \\ \vdots \\ \dot{\mathbf{s}}_M \end{bmatrix}$$
(3.5)

While only two body orbit propagation was required for the scope of this thesis, J2 perturbation effects were simulated in STK to account for the oblateness of the Earth. Once a scenario was established in STK, a MATLAB interface script containing Object Model and Connect commands was used to define SV orbits, cluster formation, and transmitter location, propagate the SVs in time, compute access from all 4 SVs to the transmitter for the duration of one pass, and export  $\mathbf{S}_{M\times 3}$  and  $\dot{\mathbf{S}}_{M\times 3}$  directly from STK to MATLAB.

## 3.4 Signal Measurement

Once  $\mathbf{S}_{M\times 3}$  and  $\dot{\mathbf{S}}_{M\times 3}$  were imported to MATLAB, true measurements were generated using the AOA, TDOA, and FDOA measurement models found in Sec. 2.3. The measurements were assumed to be taken at M instants in time. Integration time was considered to determine the CRLB for the TDOA and FDOA measurements as seen in Eq. 2.12 and Eq. 2.13, but the change in  $\mathbf{s}_m$  and  $\dot{\mathbf{s}}_m$  during integration time was considered negligible. Additionally, it was assumed that all signals received had a sufficient SNR to be processed. This assumption is validated for this research scenario by [10].

Determining the actual measurements based on simulated payload hardware and signal propagation was outside the scope of this research. However for future work the framework is established within the simulation to include a signal measurement algorithm, like MUSIC for example, to simulate real measurement.

### 3.4.1 True Measurements

This section contains the equations used to generate true AOA, TDOA, and FDOA measurements as referenced in Sec. 2.3. For each model the set of measurements  $\mathbf{m}$  are nonlinear functions of the transmitter position  $\mathbf{u}$ , SV(s) position  $\mathbf{s}$ , and SV(s) velocity  $\dot{\mathbf{s}}$  if applicable. For convenience, the convention  $\mathbf{m}(\mathbf{u})$  will be used.  $\mathbf{m}$  represents  $\boldsymbol{\alpha}$ ,  $\boldsymbol{\epsilon}$ ,  $\boldsymbol{\tau}$ , or  $\dot{\boldsymbol{\tau}}$  depending on whether you are obtaining AOA, TDOA, or FDOA.

$$\mathbf{m} = \mathbf{m}(\mathbf{u}, \mathbf{s}_i, \dot{\mathbf{s}}_i) \quad i = 1, 2, ..., S$$
(3.6)

**AOA** The process for obtaining the  $\alpha_s$  and  $\epsilon_s$  of arrival in the sensor frame given **u** and **s** is detailed in this section.

- 1. The SV position **s** is first transformed from ECEF to geodetic latitude, longitude, and ellipsoid height using MATLAB function *ecef2geodetic*. Latitude ranges from [-90°, 90°], with origin at the equator. Longitude ranges from [-180°, 180°], with origin at the Prime Meridian.
- 2. Determine the LOB vector **d** referenced from the SV to the transmitter in ECEF coordinates.

$$\mathbf{d}_{ECEF} = \mathbf{u} - \mathbf{s} \tag{3.7}$$

3. Transform the LOB unit vector  $\hat{\mathbf{d}}_{ECEF}$  into local East-North-Up (ENU) coor-

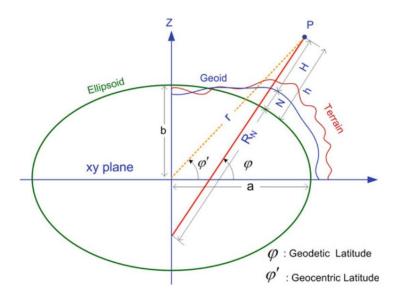


Figure 20. The relationship between various Earth surfaces (highly exaggerated) and a depiction of the ellipsoidal parameters [7]

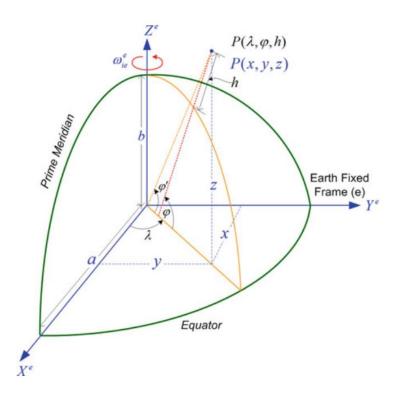


Figure 21. Two types of ECEF coordinates and their interrelationship [7]

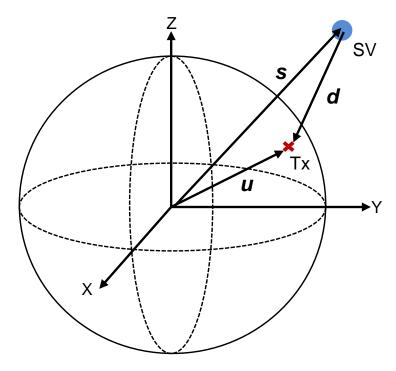


Figure 22. Two types of ECEF coordinates and their interrelationship [7]

dinates using the SV geodetic latitude  $\phi$  and longitude  $\lambda$  [7].

$$\hat{\mathbf{d}}_{ENU} = \begin{bmatrix} -\sin\lambda & \cos\lambda & 0\\ -\cos\lambda\sin\phi & -\sin\lambda\sin\phi & \cos\phi\\ \cos\lambda\cos\phi & \sin\lambda\cos\phi & \sin\phi \end{bmatrix} \hat{\mathbf{d}}_{ECEF}$$
(3.8)

4. Obtain the azimuth and elevation angles in the local ENU frame.

$$\alpha_{ENU} = \tan^{-1} \left( \frac{\hat{d}_e}{\hat{d}_n} \right) \qquad \alpha_{ENU} \in [0, 2\pi]$$

$$\epsilon_{ENU} = \tan^{-1} \left( \frac{\hat{d}_u}{\sqrt{\hat{d}_e^2 + \hat{d}_n^2}} \right) \qquad \epsilon_{ENU} \in [-\pi/2, \pi/2]$$
(3.9)

5. Transform azimuth and elevation in local ENU into the body frame. For this research  $\phi_n$  is assumed to be 0 during SV motion for simplicity's sake.

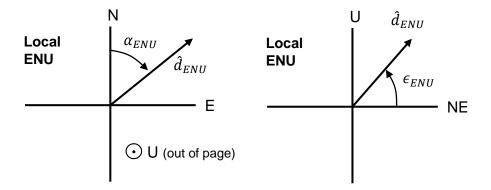


Figure 23.  $\alpha$  and  $\epsilon$  defined in the local East-North-Up coordinate frame

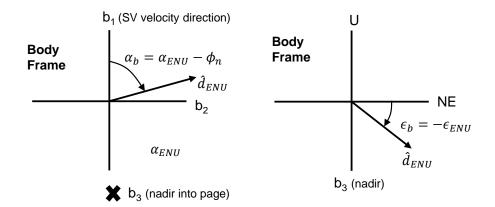


Figure 24.  $\alpha$  and  $\epsilon$  defined in the SV body frame

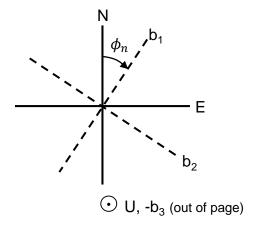


Figure 25. North angle  $\phi$  referenced from the local ENU frame to SV body frame

$$\alpha_b = \alpha_{ENU} - \phi_n \qquad \alpha_b \in [0, 2\pi]$$

$$\epsilon_b = -\epsilon_{ENU} \qquad \epsilon_b \in [-\pi/2, \pi/2]$$
(3.10)

6. Obtain the azimuth and elevation in the sensor frame. For this research the sensor frame is assumed to be aligned with the body frame for simplicity. In the case this assumption is removed, a simple rotation matrix can be applied to transform  $\alpha_b$ ,  $\epsilon_b$  into  $\alpha_s$ ,  $\epsilon_s$ .

$$\alpha_s = \alpha_b \qquad \alpha_s \in [0, 2\pi]$$

$$\epsilon_s = \epsilon_b \qquad \epsilon_s \in [-\pi/2, \pi/2]$$
(3.11)

For an entire pass of M measurements Eq. 3.12 shows the resulting angle vectors produced.

$$\boldsymbol{\alpha}_s = \begin{bmatrix} \alpha_1 & \dots & \alpha_M \end{bmatrix}^T \quad \boldsymbol{\epsilon}_s = \begin{bmatrix} \epsilon_1 & \dots & \epsilon_M \end{bmatrix}^T$$
 (3.12)

**TDOA** For S SVs the time difference measurement  $\tau_{i1}$  between the chief and each other SV is obtained via Eq. 2.5, resulting in

$$\boldsymbol{\tau}_{M\times S-1} = \begin{bmatrix} \tau_{21} & \dots & \tau_{S1} \\ \vdots & \vdots & \vdots \end{bmatrix}$$
(3.13)

**FDOA** For S SVs the nondimensionalized frequency difference measurements  $\dot{\tau}_{i1}$  are obtained using Eq. 2.6 through Eq. 2.10.

$$\dot{\boldsymbol{\tau}}_{M\times S-1} = \begin{bmatrix} \dot{\tau}_{21} & \dots & \dot{\tau}_{S1} \\ \vdots & \vdots & \vdots \end{bmatrix}$$

$$(3.14)$$

# 3.4.2 Corrupted Measurements

Sec. 2.3 discusses the inaccuracy associated with geolocation measurements due to MUSIC, CAF, and realistic payloads. This research corrupts the true measurements using Gaussian random variable X. All random errors e are assumed to have normal distributions with standard deviations  $\sigma$  and means centered at the true measurements.

$$\tilde{m} = m + e_m$$

$$e_m = X\sigma_m \qquad X \in \mathcal{N}(0, 1)$$
(3.15)

Note that subscripts of X will be used to signify different realizations of the random variable X.

Corrupted  $\alpha$  and  $\epsilon$  The error in AOA measurement is comprised of MUSIC algorithm error, payload antenna calibration error, and SV attitude knowledge error. The angle measurement error due to the payload receiver and the MUSIC algorithm is assumed to be normally distributed with standard deviation  $\sigma_{\alpha}$  and  $\sigma_{\epsilon}$ . Error in attitude determination  $e_{att}$  is also normally distributed with standard deviation  $\sigma_{att}$ . For convenience,  $e_{att}$  is assumed to be identical in the sensor frame azimuth and elevation.

$$\tilde{\alpha} = \alpha + X_1 \sigma_{\alpha} + X_2 \sigma_{att}$$

$$\tilde{\epsilon} = \epsilon + X_3 \sigma_{\epsilon} + X_4 \sigma_{att}$$
(3.16)

Corrupted  $\tau$  The error in TDOA measurement is generally influenced by SV relative clock synchronization error  $e_t$  and CAF measurement error  $e_{dto}$ .

$$\tilde{\tau} = \tau + X_1 \sigma_{dto} + X_2 \sigma_t \tag{3.17}$$

Corrupted  $\dot{\tau}$  The error in FDOA measurement is influenced by the error in relative frequency precision  $e_f$  and CAF measurement error  $e_{dfo}$ .

$$\tilde{\dot{\tau}} = \dot{\tau} + X_1 \frac{\sigma_{dfo}}{f_c} + X_2 \frac{\sigma_f}{f_c} \tag{3.18}$$

Measurement CRLB As discussed in Sec. 2.3,  $\sigma_{\alpha}$ ,  $\sigma_{\epsilon}$ ,  $\sigma_{dto}$  and  $\sigma_{dfo}$  are impacted by SNR, which is determined by several factors including slant range  $\rho_{it}$ . Thus when comparing the measurement error for different pass geometries and altitudes, the change in error due to slant range change must be incorporated. Therefore in the sensitivity analysis (Chapter 4) the measurement CRLB from Sec. 2.3 was used for  $\sigma_{\alpha}$ ,  $\sigma_{\epsilon}$ ,  $\sigma_{dto}$  and  $\sigma_{dfo}$ , and additional measurement errors were simply added to the CRLB when necessary.

Several parameters were needed to determine the CRLB for each AOA, TDOA, or FDOA measurement, including SNR, signal bandwidth, number of collectd samples, and integration time. It is assumed throughout that for each signal collect the SV receiver has integration time T of 1 ms and 10,000 samples N are obtained. The assumptions for Bandwidth, Transmit Power, Tx Antenna Gain, and Rx Antenna Gain were chosen arbitrarily to yield reasonable CRLB values for the analysis.

Table 9. Link Budget Parameters and Assumptions

Parameter	Value	Unit
Slant Range	Variable	km
Frequency	1.315	GHz
Bandwidth	1	MHz
Transmit Power	65	W
Tx Antenna Gain	10	dBi
Free-Space Path Loss	Variable	dB
Other Losses	-1	dB
Rx Antenna Gain	0	dBi
System Noise Temp	27.9 [64]	dB-K

For each of the M measurements collected during a pass, the SNR  $\gamma_i$  at each SV was calculated using Eq. 3.19 [64]. The assumptions made in the link budget are described in Table 9.

$$\gamma_i = \frac{C}{N} = \frac{P_t G_t G_r L_{atm} L_{fs}}{k T_s B_s} \qquad i = 1, 2, 3, 4 \tag{3.19}$$

The azimuth and elevation CRLBs are obtained from Eqns. 2.3 and 2.4, arranged in terms of the standard deviations  $\sigma_{\alpha}$  and  $\sigma_{\epsilon}$ . The SNR  $\gamma_1$  and elevation angle  $\epsilon$  change for each signal collect, while all other parameters in Eq. 3.20 are constant.

$$\sigma_{\alpha} = \sqrt{\frac{\gamma_1^{-1} + A}{\gamma_1 N A^2 (2\pi r/\lambda_r)^2 \sin^2(\epsilon)}}$$

$$\sigma_{\epsilon} = \sqrt{\frac{\gamma_1^{-1} + A}{\gamma_1 N A^2 (2\pi r/\lambda_r)^2 \cos^2(\epsilon)}}$$
(3.20)

The CRLB for  $\sigma_{dto}$  and  $\sigma_{dfo}$  was assumed to be constant for all SVs for a given measurement. So if there were 4 SVs in a cluster, there would be 3 TDOA measurements,  $\tau_{21}$ ,  $\tau_{31}$ , and  $\tau_{41}$ , at any instant. Each of these measurements are assumed to have the same effective SNR  $\gamma_{eff}$  due to the close proximity of the SVs. Thus,  $\gamma_1$  and  $\gamma_2$ , the SNRs at SVs 1 and 2, were used to obtain  $\gamma_{eff}$  and the corresponding CRLB for each measurement. (See Sec. 2.3).

The DTO and DFO CRLBs were described in Eqns. 2.12 and 2.13, respectively. Note that for implementation  $\sigma_{dfo}$  is nondimensionalized by the carrier frequency  $f_c$ .

$$\sigma_{dto} = \frac{0.55}{B_s \sqrt{B_n T \gamma_{eff}}}$$

$$\sigma_{dfo} = \frac{0.55}{f_c T \sqrt{B_n T \gamma_{eff}}}$$

$$\frac{1}{\gamma_{eff}} \equiv \frac{1}{2} \left[ \frac{1}{\gamma_1} + \frac{1}{\gamma_2} + \frac{1}{\gamma_1 \gamma_2} \right]$$
(3.21)

### 3.5 Initial Transmitter Localization

# 3.5.1 Corrupt SV Position and Velocity

In reality each satellite does not exactly know its position and velocity, thus it was assumed that its attitude determination and control system features a GPS receiver. It is also assumed that the error distribution is equal in all 3 ECEF directions x, y, and z. In reality, GPS navigation error will have some nonzero geometric dilution of precision (GDOP), but an equal distribution was chosen to model the worst case error and maintain simplicity.

In practice, relative position knowledge is more precise than absolute position determination due to the advent of differential GPS. Therefore the absolute position and velocity knowledge error  $(e_{p,abs}, e_{v,abs})$  is not modeled as independent, but rather uniform across all SVs in the cluster. The absolute position and velocity error can be thought of as the cluster position and velocity error.

$$\tilde{\mathbf{s}}_{i}' = \mathbf{s}_{i} + X_{1} \begin{bmatrix} \sigma_{p,abs} \\ \sigma_{p,abs} \\ \sigma_{p,abs} \end{bmatrix} \qquad \dot{\tilde{\mathbf{s}}}_{i}' = \dot{\mathbf{s}}_{i} + X_{1} \begin{bmatrix} \sigma_{v,abs} \\ \sigma_{v,abs} \\ \sigma_{v,abs} \end{bmatrix} \qquad i = 1, 2, 3, 4 \tag{3.22}$$

Relative knowledge errors  $(e_{p,rel}, e_{v,rel})$  are then added to SVs 2, 3, and 4 independently.

$$\tilde{\mathbf{s}}_{i} = \tilde{\mathbf{s}}'_{i} + X_{i} \begin{bmatrix} \sigma_{p,rel} \\ \sigma_{p,rel} \\ \sigma_{p,rel} \end{bmatrix} \qquad i = 2, 3, 4$$

$$\dot{\tilde{\mathbf{s}}}_{j} = \dot{\tilde{\mathbf{s}}}'_{j} + X_{j} \begin{bmatrix} \sigma_{v,rel} \\ \sigma_{v,rel} \\ \sigma_{v,rel} \\ \sigma_{v,rel} \end{bmatrix} \qquad j = 2, 3, 4$$

$$(3.23)$$

Notice the standard deviations of relative knowledge error is constant across the SVs but the errors are independent, since each  $X_i$  is a new realization of the random variable.

### 3.5.2 ITL Methods

Each ITL method takes M sets of measurements and obtains M ITL solutions (with exception of AOA, which obtains 1 ITL solution). See App. A for in depth implementation of each ITL method: AOA, TDOA3, TDOA4, TFDOA2, TFDOA3. Recall TFDOA4 is the same algorithm as TFDOA3, the only difference is the number of SVs.

$$\tilde{\mathbf{m}}_{LM\times 1} \to \hat{\mathbf{u}}_{M\times 3}$$
 (3.24)

In the sensitivity analysis (Chapter 4), the ITL solutions are used to evaluate algorithm accuracy. However, additional methods like maximum likelihood estimation, estimate fusion, and application of digital elevation models will be used to evaluate realistic system level performance (Chapter 5).

### 3.6 Maximum Likelihood Estimation

Once an ITL solution  $\hat{\mathbf{u}}_{ITL}$  has been obtained, the Gauss-Newton algorithm can be executed to determine the maximum likelihood estimate  $\hat{\mathbf{u}}_{MLE}$ . Recall the iterative solution for  $\hat{\mathbf{u}}_{MLE}$  from Sec. 2.5.3.

$$\hat{\mathbf{u}}_{k+1} = \hat{\mathbf{u}}_k + (\mathbf{J}^T \mathbf{Q}_m^{-1} \mathbf{J})^{-1} \mathbf{J}^T \mathbf{Q}_m^{-1} [\tilde{\mathbf{m}} - \mathbf{m}(\hat{\mathbf{u}}_k)]$$

$$||\hat{\mathbf{u}}_{k+1} - \hat{\mathbf{u}}_k|| \le tol$$
(3.25)

The parameters on the right side of Eq. 3.25 must be determined to execute the algorithm. The initial guess  $\hat{\mathbf{u}}_0$  is the average of all the ITL solutions for that pass

 $(\hat{\mathbf{u}}_{M\times 3})$  which were obtained in Sec. 3.5.2.  $\mathbf{Q}_m$  is  $LM\times LM$ , where L is the number of measurement parameters per collect. For AOA, L=2, for 4-ball TDOA, L=3.

$$\mathbf{Q}_{m} = \operatorname{diag}[\sigma_{\alpha_{1}}^{2}, \sigma_{\epsilon_{1}}^{2}, ..., \sigma_{\alpha_{M}}^{2}, \sigma_{\epsilon_{M}}^{2}] \quad (AOA)$$

$$= \operatorname{diag}[\sigma_{\tau_{21_{1}}}^{2}, \sigma_{\tau_{31_{1}}}^{2}, ..., \sigma_{\tau_{21_{M}}}^{2}, \sigma_{\tau_{31_{M}}}^{2}] \quad (TDOA3)$$

$$= \operatorname{diag}[\sigma_{\tau_{21_{1}}}^{2}, \sigma_{\dot{\tau}_{21_{1}}}^{2}, ..., \sigma_{\tau_{21_{M}}}^{2}, \sigma_{\dot{\tau}_{21_{M}}}^{2}] \quad (TFDOA2)$$
(3.26)

The Jacobian matrix  $\mathbf{J}$  is  $LM \times 3$  and represents the change in measurements with respect to change in transmitter location.  $\mathbf{J}$  for the TFDOA2 case will be expressed here,  $\mathbf{J}$  for other techniques (AOA, TDOA3, TDOA4, TFDOA2, TFDOA4) can be inferred.

$$\mathbf{J} = \frac{\partial \mathbf{m}}{\partial \mathbf{u}} = \begin{bmatrix} \frac{\partial \tau_{21_1}}{\partial u_x} & \frac{\partial \tau_{21_1}}{\partial u_y} & \frac{\partial \tau_{21_1}}{\partial u_z} \\ \frac{\partial \dot{\tau}_{21_1}}{\partial u_x} & \frac{\partial \dot{\tau}_{21_1}}{\partial u_y} & \frac{\partial \dot{\tau}_{21_1}}{\partial u_z} \\ \vdots & \vdots & \vdots \\ \frac{\partial \tau_{21_M}}{\partial u_x} & \frac{\partial \tau_{21_M}}{\partial u_y} & \frac{\partial \tau_{21_M}}{\partial u_z} \\ \frac{\partial \dot{\tau}_{21_M}}{\partial u_x} & \frac{\partial \dot{\tau}_{21_M}}{\partial u_y} & \frac{\partial \dot{\tau}_{21_M}}{\partial u_z} \end{bmatrix}$$

$$(3.27)$$

The expected and corrupted measurements  $\mathbf{m}(\hat{\mathbf{u}}_k)$  and  $\tilde{\mathbf{m}}$  are each  $LM \times 1$  and were defined in Eqns. 2.16 and 2.17, but are rewritten for the TFDOA2 case as an example in Eq. 3.28.  $\mathbf{m}(\hat{\mathbf{u}}_k)$  contains the expected true measurements given the current transmitter location estimate.

$$\mathbf{m}(\mathbf{u}) = [\tau_{21_1}, \dot{\tau}_{21_1}, ..., \tau_{21_M}, \dot{\tau}_{21_M}]^T$$

$$\tilde{\mathbf{m}} = [\tilde{\tau}_{21_1}, \tilde{\dot{\tau}}_{21_1}, ..., \tilde{\tau}_{21_M}, \tilde{\dot{\tau}}_{21_M}]^T$$
(3.28)

If the estimate converges to within tol = 0.1 m the method is complete. Estimates which diverge are discarded and the original guess  $\hat{\mathbf{u}}_0$  is defined as  $\hat{\mathbf{u}}_{MLE}$ .

# 3.7 Application of DEM

The method for refining the estimate  $\hat{\mathbf{u}}$  using a digital elevation model is similar to the one Schmidt [8] used. As discussed in Sec. 2.6, the DEM utilized for the grid search was USGS 3-arcsecond SRTM data [62]. This DEM will be referred to as DTED1 for convenience. The method of downloading this data is explained in App. B. The process for applying DTED1 to obtain a better estimate for  $\mathbf{u}$  is as follows:

- 1. **Seed**. Use the MLE estimate  $\hat{\mathbf{u}}_{MLE}$  as the seed, or initial guess, for the following grid search. First convert the seed  $\hat{\mathbf{u}}_{MLE}$  from ECEF coordinates to latitude, longitude, and elevation using the MATLAB function ecef2lla.
- 2. Grid Size. The 95% confidence ellipsoid semi-major axis (SMA) length (Sec. 3.8) is used to determine the grid width w<sub>g</sub>. This method avoids the computational inefficiency of importing unnecessary grid points. A rough approximation of 110 km ≈ 1° latitude is used to convert the SMA length into degrees. The grid limits are then defined using the seed.

$$LATLIM = [lat_{\hat{u}} - 0.5h_g, lat_{\hat{u}} + 0.5h_g]$$

$$LONLIM = [lon_{\hat{u}} - 0.5w_g, lon_{\hat{u}} + 0.5w_g]$$

$$h_g = w_g = SMA(\text{km}) \left(\frac{1^{\circ}}{110 \text{ km}}\right)$$
(3.29)

If  $w_g$  is too large then the grid desired might require multiple DTED1  $1^{\circ} \times 1^{\circ}$  files. It is assumed that if  $w_g$  is too large (> 100 km uncertainty) then a DTED1 grid search won't greatly improve the estimate. Though rare, if  $w_g$  is too small then not enough DTED1 posts will be imported. Thus lower and upper bounds are set for  $w_g$  for this research.

$$0.5 \text{ km} \left( \frac{1^{\circ}}{110 \text{ km}} \right) < w_g < 0.5^{\circ}$$
 (3.30)

3. Import DTED1. Once the grid limits are defined, DTED1 can be imported using the MATLAB dted function. App. B explains how DTED data can be downloaded in advance. MATLAB's dted allows sampling factor  $s_f$  to be chosen. MATLAB extracts every  $s_f^{th}$  point from the DTED1 grid. For a large grid  $s_f = 1$  can be computationally inefficient. Thus, a constant number of grid cells is chosen, then  $s_f$  is calculated based on the grid size  $w_g$ .

$$desired\ grid\ cells = constant = 20$$

$$DTED1\ resolution = 1200\ cells/deg$$

$$DTED1\ cells = w_g(DTED1\ resolution)$$

$$s_f \approx \frac{DTED1\ cells}{desired\ grid\ cells}$$

$$(3.31)$$

The data returned is a square matrix containing elevations (in meters) referenced to the Earth Gravitational Model (EGM 96). Each elevation value is the orthometric height H (Fig. 12).

4. Get WGS84 Ellipsoid Height h. The next step is to define the newfound elevation data with respect to the WGS84 ellipsoid using Eq. 3.32. Recall Fig. 12 from Sec. 2.6.

$$h = H + N \tag{3.32}$$

The Geoid heights N for the grid defined in Eq. 3.29 are obtained via the MATLAB function egm96geoid. Since the Geoid has poorer resolution than DTED1, ltln2val is used to perform bicubic interpolation to obtain the correct N for each DTED1 post H.

5. LLA to ECEF. Convert the geodetic coordinates of each post (latitude, lon-

gitude, WGS84 height) into ECEF coordinates using *lla2ecef*.

$$(\phi, \lambda, h) \to (x, y, z) \tag{3.33}$$

6. Choose Best Post. The maximum likelihood principle is applied to choose the DTED1 post closest to u. The correct post is the one that minimizes the original measurement errors. Recall Eq. 2.20 and rearrange in terms of the posts p.

$$\hat{\mathbf{u}}_p = \arg\min_{\mathbf{p}} \left\{ [\tilde{\mathbf{m}} - \mathbf{m}(\mathbf{p})]^T \mathbf{W} [\tilde{\mathbf{m}} - \mathbf{m}(\mathbf{p})] \right\}$$
(3.34)

The right side of Eq. 3.34 is the figure of merit (FOM)  $\psi_i$ .  $\psi_i$  is explicitly calculated for each post. This method of obtaining an FOM is more computationally burdensome than the FOMs Schmidt [8] utilized, however it has higher fidelity and is uniform for each of the algorithm types (AOA, TDOA, T/FDOA).  $\psi_i$  only differs by the type of measurement inputs  $\mathbf{m}$ .

$$\psi_i = [\tilde{\mathbf{m}} - \mathbf{m}(\mathbf{p}_i)]^T \mathbf{W} [\tilde{\mathbf{m}} - \mathbf{m}(\mathbf{p}_i)] \qquad i = 1, 2, ..., P$$
 (3.35)

In Eq. 3.35  $\tilde{\mathbf{m}}$  is  $LM \times 1$  set of measurements for the pass,  $\mathbf{m}(\mathbf{p}_i)$  is the set of expected measurements were the true transmitter located at  $\mathbf{p}_i$ , and  $\mathbf{W}$  weighting matrix, defined as  $\mathbf{Q}_m^{-1}$  (See Eq. 3.26). The optimal  $\mathbf{p}_i$  is the one that corresponds to the minimum  $\psi_i$ .

$$\hat{\mathbf{u}}_{dted} = \arg\min_{\mathbf{p}} \left\{ \boldsymbol{\psi} \right\} \tag{3.36}$$

7. **Iterate**. If the chosen post  $\hat{\mathbf{u}}_p$  lies on the outside of the grid, it is possible that the optimal solution may be off the grid. Therefore it is necessary to redefine the grid with  $\hat{\mathbf{u}}_p$  as the seed, and return to step 2.

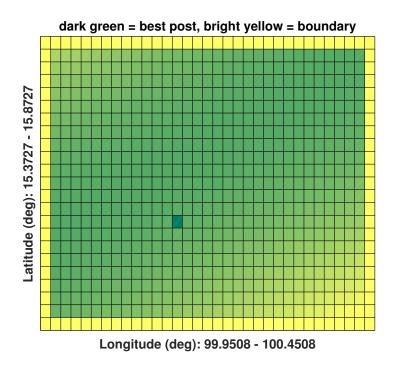


Figure 26. DTED1 grid search for post that minimizes FOM  $\psi$ 

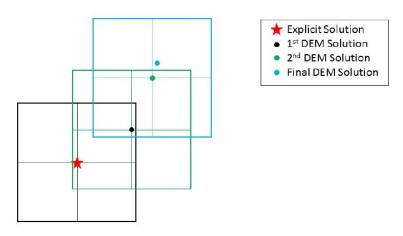


Figure 27. Example of DEM iterative grid search when chosen post is near grid boundary ([8])

The final geolocation solution obtained by the DTED1 grid search lies on a DTED1 elevation post, so there is additional uncertainty since the true transmitter location was defined with the DTED2 data (Sec. 3.2.1). This uncertainty caused by difference in resolution between DTED1 and DTED2 as shown in Fig. 28. The effect of this

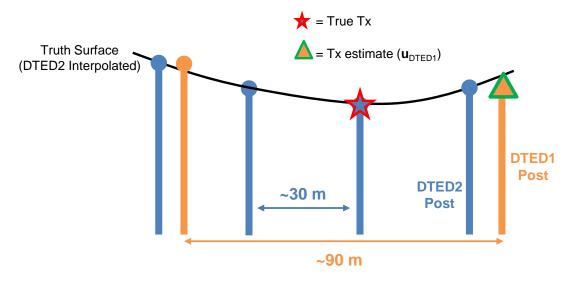


Figure 28. Geolocation error due to resolution of DTED1

uncertainty is negligible for this research because for the geolocation error due to system errors is much larger than the resolution discrepancy of the DEMs.

## 3.8 Measures of Performance

This section contains the quantitative measures used in Chapters 4 and 5 to evaluate performance. Overall, four MOPs were used to assess geolocation accuracy: range root mean square error, average miss distance, average ellipsoid volume, and average semi-major axis length.

Table 10. Measures of Performance

MOP	Symbol	Unit
Range RMSE	RMSE	m
Average Miss Distance	AMD	m
Average Ellipsoid Semi-Major Axis Length	$\overline{SMA}$	m
Average Ellipsoid Volume	$\overline{V}$	$\mathrm{m}^3$

$$\mathbf{e}_{\hat{\mathbf{u}}} = \hat{\mathbf{u}} - \mathbf{u} = \begin{bmatrix} e_x \\ e_y \\ e_z \end{bmatrix}$$
 (3.37)

The covariance matrix is defined as

$$\mathbf{C}_{\hat{\mathbf{u}}} = E[(\hat{\mathbf{u}} - \mathbf{u})(\hat{\mathbf{u}} - \mathbf{u})^T] \tag{3.38}$$

The absolute range error for a single estimate  $\hat{\mathbf{u}}$  is shown in Eq. 3.39.

$$e_{\rho} = \sqrt{(\hat{\mathbf{u}} - \mathbf{u})^T(\hat{\mathbf{u}} - \mathbf{u})} = \sqrt{\mathbf{e}_{\hat{\mathbf{u}}}^T \mathbf{e}_{\hat{\mathbf{u}}}}$$
 (3.39)

**ECEF to ENU Transformation** The absolute error and covariance matrix are expressed in ECEF coordinates. To graphically depict the estimate  $\hat{\mathbf{u}}$  and its covariance matrix  $\mathbf{C}$  in East-North-Up (ENU) coordinates, it is necessary to use the transformation matrix  $\mathbf{R}_{ecef}^{enu}$ .  $\lambda$  and  $\phi$  are the longitude and latitude of the reference

point. In Chapter 5 the reference point is the true transmitter location **u**.

$$\hat{\mathbf{u}}_{enu} = \mathbf{R}\hat{\mathbf{u}}_{ecef}$$

$$\hat{\mathbf{u}}_{enu} = \mathbf{R}\mathbf{C}_{ecef}\mathbf{R}^{T}$$

$$-\sin\lambda \quad \cos\lambda \quad 0$$

$$-\cos\lambda\sin\phi \quad -\sin\lambda\sin\phi \quad \cos\phi$$

$$\cos\lambda\cos\phi \quad \sin\lambda\cos\phi \quad \sin\phi$$
(3.40)

Ellipsoid Semi-Major Axis Length The square root of the eigenvalues of C represent the 3 ellipsoid axis lengths. The semi-major axis (SMA) is the maximum of the 3 semi-axis lengths. The SMA of the 95% confidence ellipsoid is obtained by multiplying the scale factor  $\chi$  times the square root of the eigenvalue.

$$SMA_{95\%} = \chi \sqrt{\lambda_{max}}$$

$$\chi^2 = 7.815$$
(3.41)

**Ellipsoid Volume** Each of the semi-axis lengths (a, b, and c) of the 95% confidence ellipsoid is defined as  $2.8\sqrt{\lambda_i}$ . The 95% confidence ellipsoid volume is:

$$V_{95\%} = \frac{4}{3}\pi abc \tag{3.42}$$

It is valuable to maintain both the ellipsoid volume and SMA because a confidence ellipsoid with small volume could be misleading if it has very large SMA.

## 3.8.1 Monte Carlo Simulation

The geolocation simulation includes Gaussian random variables used to model system errors. A Monte Carlo Simulation (MCS) is useful when the probability of a random variable cannot be determined analytically or numerically [65]. An

MCS involves executing N trials of a test and obtaining the expected value of the outcomes [65]. Depending on the test, hundreds or thousands (or more) trials could be needed for the statistics to converge. For the tests in this research involving random noise, N trials were run and the 4 MOPs below were determined. These MOP definitions were also utilized in Guo [3] and Schmidt [8], among others.

## 1. Range Root Mean Square Error (RMSE)

$$RMSE = \sqrt{\frac{1}{N} \sum_{n=1}^{N} (\hat{\mathbf{u}} - \mathbf{u})^{T} (\hat{\mathbf{u}} - \mathbf{u})}$$
(3.43)

# 2. Average miss distance (AMD)

$$AMD = \frac{1}{N} \sum_{n=1}^{N} \sqrt{(\hat{\mathbf{u}} - \mathbf{u})^T (\hat{\mathbf{u}} - \mathbf{u})}$$
(3.44)

### 3. Average Ellipsoid SMA

$$\overline{SMA}_{95\%} = \frac{1}{N} \sum_{n=1}^{N} SMA_{95\%_n}$$
 (3.45)

## 4. Average Ellipsoid Volume

$$\overline{V}_{95\%} = \frac{1}{N} \sum_{n=1}^{N} V_{95\%_n} \tag{3.46}$$

Due to limited time and the computational efficiency of the algorithms used in this research, enough trials were executed to observe general trends in the data, but in some test cases more trials would be needed to have statistical convergence

# 3.9 Summary

This chapter described the methods used to simulate a geolocation scenario and obtain an estimate for an RF transmitter's location using initial transmitter localization (ITL) techniques, maximum likelihood estimation, fusion, and digital elevation models. The next chapter contains the results and analysis pertaining to the sensitivity of ITL accuracy to system errors and variation in SV orbit geometry. Chapter 5 demonstrates how geolocation accuracy is significantly improved when the methods discussed in Chapter 3 are combined.

# 4. Sensitivity Analysis

#### 4.1 Overview

This chapter contains analysis of the sensitivity of the initial transmitter localization (ITL) accuracy to system errors and SV orbit geometry.

Trade Space The sensitivity of ITL accuracy to 11 different parameters was analyzed. These parameters and their trade spaces are seen in Table 11. Notice there are some parameters related to System Performance (See Table 17) not included, namely attitude knowledge error and time/frequency synchronization errors, due to their redundancy. For example, in the simulation, attitude knowledge error is simply added to AOA measurement error (Sec. 3.4.2), so doing an additional trade on attitude knowledge impact on ITL accuracy would be redundant with a trade on AOA measurement error.

**Methods** Several assumptions were made in this sensitivity analysis to isolate the variable of interest's effect on geolocation accuracy.

- Isotropic Transmitter. The transmitter utilized in this sensitivity analysis has an isotropic beam pattern. The transmitter beam pattern and SV ground tracks for each pass type are seen in Fig. 15. A signal collect was simulated approximately every 12 seconds.
- Transmitter Altitude. The true transmitter altitude is assumed to be known. Therefore no iteration is required to obtain the transmitter altitude  $r_e$ , and altitude errors can be factored out of the resultant ITL error.
- Baseline. Fig. 46 from the baseline analysis was used to determine a viable baseline distance to use for all sensitivity analyses. It was determined that error

Table 11. Sensitivity Analysis Trade Space

Parameter	Trade Space	Remarks				
SV Altitude	[350, 1000] km	Lower bound: $\Delta V$ required, Upp bound: Van Allen belt				
Pass Geometry	1-5	1 = Pass directly overhead, 5 = Pass near horizon (Fig. 15)				
Baseline	1-30 km	Defined by separation distance from chief (in-track or cross-track)				
# Signal Collects	[2, 20]	At least 2 collects needed for AOA solution (2 LOBs)				
	SV Navigation Errors					
Absolute Position	[0, 50] m	Assuming on-board GPS receiver				
Absolute Velocity	[0, 1] m/s	Assuming on-board GPS receiver				
Relative Position	[0, 5] m	Assuming Differential GPS				
Relative Velocity	[0, 0.5]  m/s	Assuming Differential GPS				
Measurement Errors						
Az and El	$[0, 0.5] \deg$	Error in Az and El angle measurements, due to hardware and MUSIC algorithm error				
Differential Time Offset (DTO)	[0, 150] ns	Time difference measurement error, due to hardware and Complex Ambi- guity Function (CAF) accuracy				
Differential Freq. Offset (DFO)	[0, 150] Hz	Frequency difference measurement error, due to hardware and CAF accuracy				

due to short baseline did not decrease much beyond 15 km. The relative SV geometry for this scenario is seen in Fig. 17. Also Tx 1 (Table 6) was chosen because for the relative SV geometry was most constant compared to the mock transmitters at other latitudes.

• Number of Collects. For all of the analyses (except ITL sensitivity to number of signal collects and pass geometry) the minimum number of signal collects to obtain an ITL solution was utilized. That way the number of collects was removed as an independent variable. For the Pass Geometry analysis, the num-

ber of collects varied with pass type (Fig. 15). For the "number of collects" analysis, M was the independent variable.

• System Errors. For the Altitude, Pass Geometry, Baseline, and Number of Collects analyses, all system errors were assumed to be zero except that the measurement error was set to equal the MUSIC or CAF CRLB (Eqs. 2.3, 2.4, 2.12, 2.13). There is variation of slant range inherent with altitude and collection geometry changes, so measurement error based off of the CRLB is used to include slant range effects on measurements. However, for the other analyses all system errors were set to zero except for the variable being traded.

For each test case, system parameters were defined, then the initial transmitter localization (ITL) solution was calculated for N Monte Carlo trials. In the cases where solutions could not be found due to high system errors or solutions not within line of sight of the SVs, solutions were discarded. Then the ITL root mean square error (RMSE) was determined using Eq. 3.43. All of the results in this sensitivity analysis contain accuracy in terms of ITL RMSE (km).

## 4.1.1 Initial Noise-Free Test

Before the ITL accuracy in the present of system errors was analyzed, it was necessary to obtain a baseline by observing the ITL method accuracy and computation time without the presence of measurement and SV location errors. For a single pass of M measurements, the time to compute M ITL solutions and the RMSE of those M ITL solutions was determined. The exception is that the AOA algorithm produces 1 ITL solution for M measurements. For this test, it was assumed the true transmitter altitude was known and root disambiguation errors were ignored. The computation times were normalized by the fastest time, which was the AOA processing time  $t_{aoa}$ . Results are shown in Table 12. Note that TFDOA3 and TFDOA4 are really the same

method, and their inaccuracy is caused due to the tolerance of the Newton method search, which was set to 1 m for this test. The AOA algorithm was the fastest and

Table 12. ITL Method Accuracy and Computation Time in Noise-Free Case

ITL Method	# of SVs	ITL RMSE (m)	Normalized	
11L Method	# 01 5 V S	TIL RIVISE (III)	Comp. Time	
AOA	1	5.35e-9	1.00	
TDOA3	3	5.71e-6	7.50	
TDOA4	4	1.15e-4	5.99	
TFDOA2	2	3.66e-6	10.47	
TFDOA3	3	1.59	15.87	
TFDOA4	4	2.20	14.65	

Note: Tx 3, Pass 3, M = 30, times normalized by  $t_{aoa}$ 

most accurate, because the algorithm requires only trigonometry and a single LS intersection. The other algorithms require solving polynomial equations for the root  $\rho_1$ . Furthermore, TFDOA3 involves Newton iteration, which adds additional time. Recall that TFDOA3 and TFDOA4 are the same algorithm, the only difference is number of SVs. Computation time for TFDOA3 can be decreased by decreasing the Newton method tolerance, although some accuracy will be forfeited.

### 4.2 ITL Sensitivity to Altitude

It is important to point out that in this analysis the signal collects were simulated to occur directly above the transmitter, so that the SV ground track was co-located with the transmitter (Fig. 29). Therefore as the altitude was increased, only slant range from the transmitter to the SVs was increased. If the SVs were not directly overhead, a change in altitude would be accompanied with change in elevation angle of the SVs w.r.t. the transmitter.

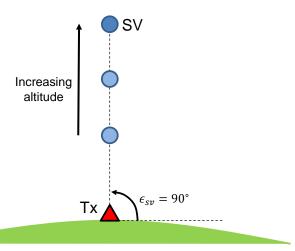


Figure 29. Method of increasing SV altitude for sensitivity analysis (Not to scale)

# 4.2.1 AOA Sensitivity to Altitude

To begin, the effect of altitude on single-SV AOA accuracy was studied. All system errors were assumed to be zero except the AOA measurement error,  $\sigma_{\alpha}$  and  $\sigma_{\epsilon}$ . The CRLB from Eq. 2.3 and Eq. 2.4 was used to model  $\sigma_{\alpha}$  and  $\sigma_{\epsilon}$  at each altitude. The altitude certainly has an impact on the best measurement accuracy achievable since  $\sigma_{\alpha}$  and  $\sigma_{\epsilon}$  depend on SNR  $\gamma$ . Modeling angle measurement error as constant for all altitudes would yield overly optimistic results at higher altitudes. The results in Fig. 30 show that as altitude increases AOA geolocation accuracy decreases. The fundamental independent variable is slant range. Slant range impacts 1) the angle measurement error due reduced signal strength caused by free-space loss and 2) the effect small measurement noise has on the ITL algorithm solution. Fig. 31 shows how the signal measurement error (AOA), modeled as the CRLB, increases Secondly, of slant range has an as altitude, or slant range in this case, increases. impact on AOA error due to the basic geometry of the AOA algorithm. As shown in Fig. 32, increase in slant range  $\rho_1$  for constant angle error causes greater estimate uncertainty. The uncertainty of the line of bearing (LOB) end points generated from AOA measurements will be greater as the slant range increases, for a constant angle

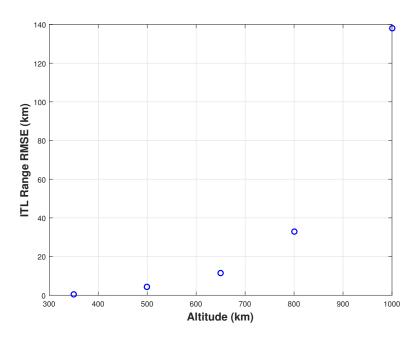


Figure 30. AOA algorithm sensitivity to SV altitude (Tx 1, Pass 1, 1 collect, 2000 trials,  $\sigma_{\alpha} = \sigma_{\epsilon} = CRLB$ )

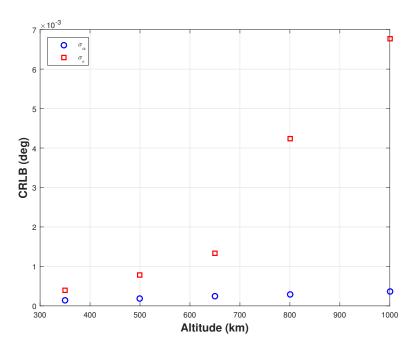


Figure 31. MUSIC  $(\sigma_{\alpha}, \sigma_{\epsilon})$  CRLB at different altitudes (See Eqs. 2.3 and 2.4)

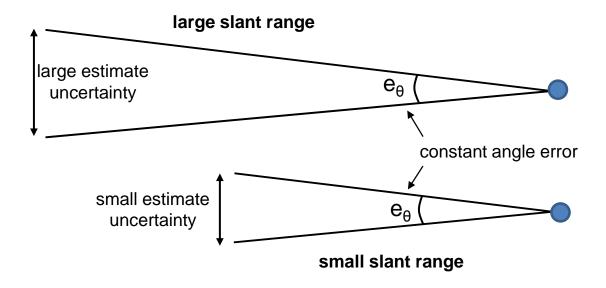


Figure 32. Constant AOA error leads to large estimate uncertainty in presence of large slant range, due to geometry

error.

# 4.2.2 TDOA Sensitivity to Altitude

It is observed in Figs. 33 and 34 that for both the TDOA3 and TDOA4 algorithms, accuracy decreases with increase in altitude. This effect is attributed to the increase in slant range, which affects the measurement error  $\sigma_{\tau}$  and the TDOA algorithm equation. As seen in Fig. 35,  $\sigma_{\tau}$  increases due to decrease in SNR  $\gamma$  caused by free-space loss (See Eq. 2.12). The effect of increased slant range on the TDOA algorithm is seen in the general TDOA Eq. A.18 found in App. A.

$$\tilde{r}_{i1}^2 + 2\rho_1 \tilde{r}_{i1} = \mathbf{s}_i^T \mathbf{s}_i - \mathbf{s}_1^T \mathbf{s}_1 - 2(\mathbf{s}_i - \mathbf{s}_1)^T \mathbf{u}$$

$$(4.1)$$

The TDOA corrupted by measurement error  $\tilde{\tau}_{i1}$  causes  $r_{i1}$  in Eq. 4.1 to become corrupted  $(\tilde{r}_{i1})$ , due to Eq. 2.5. So as the slant range  $\rho_1$  increases, the second term in Eq. 4.1 becomes larger, thereby magnifying the effect measurement noise has on

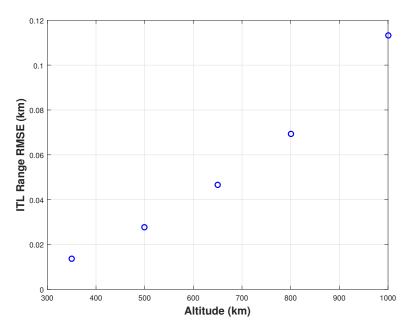


Figure 33. TDOA3 algorithm sensitivity to SV altitude (Tx 1, Pass 1, 1 collect, 2000 trials,  $\sigma_{\tau} = CRLB$ )

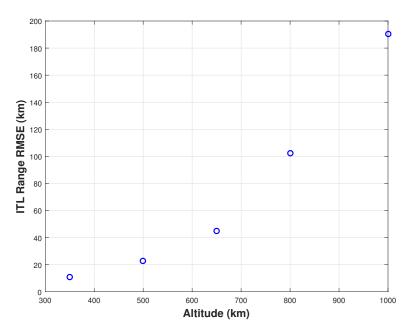


Figure 34. TDOA4 algorithm sensitivity to SV altitude (Tx 1, Pass 1, 1 collect, 2000 trials,  $\sigma_{\tau} = CRLB$ )

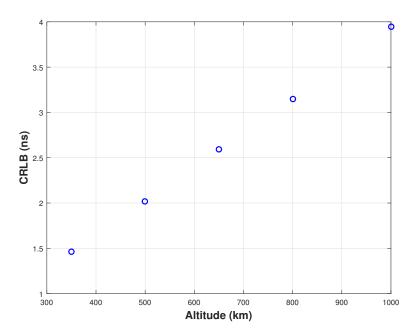


Figure 35. Complex Ambiguity Function (CAF) differential time offset CRLB  $\sigma_{\tau}$  at different altitudes (See (2.12))

the TDOA equation. When there are any corrupt terms in the equation, the left side is not equal to the right side. This discrepancy will be referred to in this section as the equation defect.

### 4.2.3 T/FDOA Sensitivity to Altitude

Similar to AOA and TDOA, for the T/FDOA methods geolocation error increases as SV altitude increases, as shown in Figs. 36 and 37. The slant range impacts the DTO and DFO measurement errors ( $\sigma_{\tau}$  and  $\sigma_{f}$ ), because of the lower SNR caused by free-space loss. The effect of SNR on measurement error is seen in Eqs. 2.12 and 2.13, and the impact of altitude, or more specifically slant range, on the CAF CRLB is shown in Fig. 38. Slant range  $\rho_{1}$  also impacts the TDOA and T/FDOA equation defect. The effect of  $\rho_{1}$  on the general TDOA equation was discussed in Sec. 4.2.2. The T/FDOA general equation is rewritten in Eq. 4.2 with the corrupt range and range rate difference measurements  $\tilde{r}_{i1}$  and  $\tilde{r}_{i1}$ . The range rate difference measurements  $\tilde{r}_{i1}$  are corrupted by erroneous FDOA measurement errors  $\tilde{\tau}_{i1}$  according

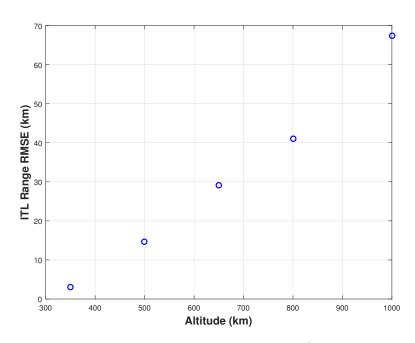


Figure 36. TFDOA2 algorithm sensitivity to SV altitude (Tx 1, Pass 1, 1 collect, 2000 trials,  $\sigma_{\tau} = CRLB$ ,  $\sigma_{\dot{\tau}} = CRLB$ )

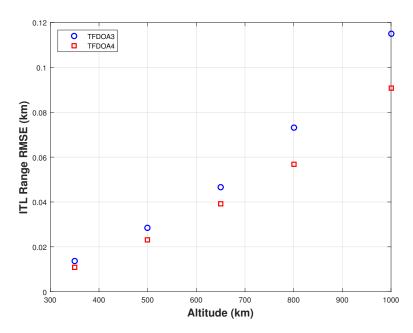


Figure 37. T/FDOA algorithm sensitivity to SV altitude (Tx 1, Pass 1, 1 collect, 2000 trials,  $\sigma_{\tau} = CRLB$ ,  $\sigma_{\dot{\tau}} = CRLB$ )

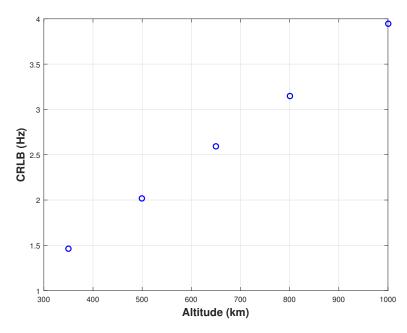


Figure 38. Complex Ambiguity Function (CAF) differential frequency offset CRLB  $\sigma_f$  at different altitudes (See (2.12))

to Eq. 2.6.

$$2\tilde{r}_{i1}\tilde{r}_{i1} + 2\tilde{r}_{i1}\dot{\rho}_1 + 2\tilde{r}_{i1}\rho_1 - 2\mathbf{s}_i^T\dot{\mathbf{s}}_i + 2\mathbf{s}_1^T\dot{\mathbf{s}}_1 = -2(\dot{\mathbf{s}}_i - \dot{\mathbf{s}}_1)^T\mathbf{u} \qquad i = 2, 3, ..., S \quad (4.2)$$

It is seen from an (4.2) that an increase in  $\rho_1$  causes the third term in Eq. 4.2 to be magnified. Thus for two different cases where the noise in  $\tilde{r}_{i1}$  is constant, the one with larger  $\rho_1$  will have greater T/FDOA equation defect.

It can be observed from Figs. 36 and 37 that for the same measurement errors  $\sigma_{\tau}$  and  $\sigma_{f}$ , as the number of SVs increases, the ITL accuracy improves. This is to be expected, since as the number of SVs increase, the number of measurements per collect increases. Note that the TFDOA3 and TFDOA4 were executed with the same algorithm, T/FDOA for  $S \geq 3$  [23]. Therefore it is expected that their sensitivity to altitude have similar trends.

## 4.2.4 Altitude Sensitivity Summary

Another result evident in Fig. 34 is that compared with TDOA3 Fig. 33 the same measurement error yields much larger error in the TDOA4 algorithm. This effect is discussed in subsequent analyses.

In general, as the altitude of any SV or constellation increases, the geolocation accuracy will decrease. This statement is true for all of the methods considered when only the altitude changes. Essentially, change in altitude corresponds with change in slant range, which impacts both the signal measurement error and the ITL algorithm equation defect in the noisy case.

It is important to note that for a single pass, depending on the collection geometry, an increase in altitude could entail an increase in slant range and elevation angle of the SVs w.r.t. the transmitter. A graphic of this is seen in Fig. 39. In this

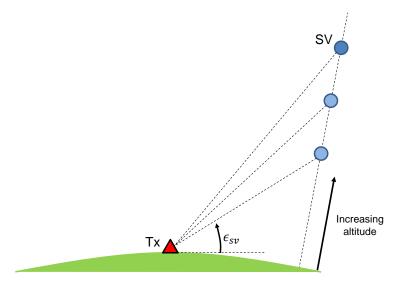


Figure 39. Effect of increasing SV altitude on slant range and elevation of SVs w.r.t. transmitter for non-overhead passes (Not to scale)

case, the slant range is not the only independent variable, and the ITL algorithm error could display a different trend than discussed in this section. For example, if elevation angle of the SVs also increased, AOA and TDOA3 error could decrease.

Guo [3] demonstrated how TDOA3 error was smaller when the Tx was close to the sub-satellite point. However, the orbit designer is not taking into account a single pass, but all the different pass geometries over a mission lifetime, and for that scope, increased altitude generally yields increased geolocation error.

## 4.3 ITL Sensitivity to Pass Geometry

The 5 different pass types defined in Fig. 15 represent 5 possible signal collection geometries. For an isotropic transmitter, a SV passing overhead will have more opportunities to collect the signal of interest. Furthermore, during the course of a single pass, both the slant range and the elevation angle of the SVs w.r.t. the transmitter are changing. So there are several independent variables involved in a change in pass type. It is also important to note that for the case of an unknown transmitter, the pass type cannot be controlled by the designer. The purpose of this analysis is to investigate the general behavior ITL algorithms for different pass types.

# 4.3.1 AOA Sensitivity to Pass Geometry

The AOA algorithm sensitivity to the 5 different pass types is seen in Fig. 40. It is evident from Fig. 40 that the geolocation error is less for overhead passes than for passes close to the horizon. Recall that for this analysis it was assumed that the SV receiver had an isotropic beam pattern, so the receiver gain was equal in all directions. Therefore, signal collects near the horizon had a lower SNR than collects close to overhead, due to longer slant range. However, many payload antennas have omni-directional or directional beam patterns, which could have higher gain for lower elevation angles. The trend seen in Fig. 40 is only applicable for systems where angle measurement error is decreased at the horizon due to slant range and/or elevation.

The increase in ITL error from Passes 1-5 is caused by several factors. Firstly,

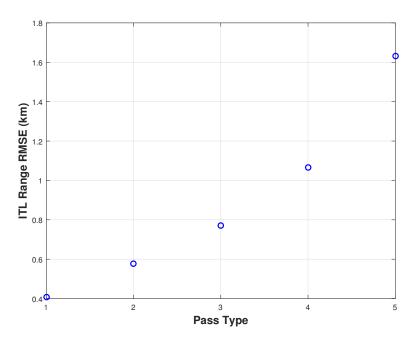


Figure 40. AOA algorithm sensitivity to pass geometry (Tx 1, 2000 trials,  $\sigma_{\alpha} = \sigma_{\epsilon} = CRLB$ )

as the pass number increases, the average elevation angle of arrival decreases, since the passes become closer to the horizon. It can be seen in Eq. 2.4 how the MUSIC CRLB increases as elevation of arrival decreases. Secondly, as pass number increases, the average slant range for the entire pass increases. It was discussed in Sec. 4.2 how slant range impacts the both the angle measurement error and the uncertainty of the LOBs in the noise case. Lastly, as the pass number increases, the number of collects decreases for this isotropic transmitter case. It will be investigated in Sec. 4.5 how more signal collects can lead to a more accurate geolocation estimate.

# 4.3.2 TDOA Sensitivity to Pass Geometry

The TDOA3 and TDOA4 algorithm sensitivity to the pass type is shown in Figs. 41 and 42, respectively. For this analysis it was assumed that the 15 km baseline distance between the satellites remained relatively constant during the entire pass. It is left for future work to explore how a more geometrically diverse satellite formation

influences the algorithm accuracy for different pass types. In addition, it was assumed that the SV receiver gain was equal in all directions, so the change in SNR was solely influenced by free-space loss. As a result, the CAF CRLB increased with slant range.

For TDOA3 passes close to overhead were more accurate than passes close to the

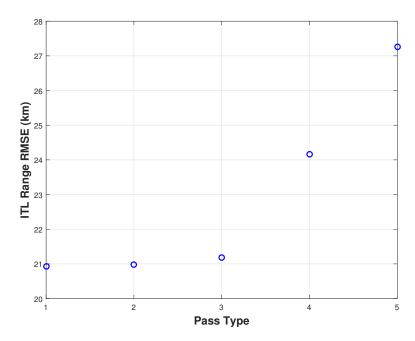


Figure 41. TDOA3 algorithm sensitivity to pass geometry (Tx 1, 2000 trials,  $\sigma_{\tau} = CRLB$ )

horizon. For the other transmitter locations tested (Table 6) this general trend was also true. This trend is consistent with Guo's [3] findings that the TDOA3 solutions are most accurate when the transmitter is near the sub-satellite point. Furthermore, Pass 1 contains several signal collects overhead the transmitter, so it is expected that it is generally more accurate.

It is evident from Fig. 42 that for TDOA4, "middle" passes are the most accurate for this scenario. The extent to which middle passes are "better" for this particular TDOA4 algorithm is dependent on the SV formation geometry and the DTO measurement error.

There are several factors which influence the TDOA algorithm error. The impact

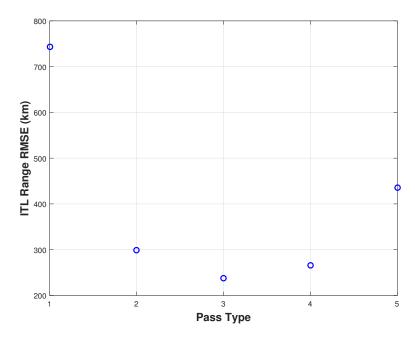


Figure 42. TDOA4 algorithm sensitivity to pass geometry (Tx 1, 2000 trials,  $\sigma_{\tau} = CRLB$ )

of slant range  $\rho_i$  on DTO measurement error  $\sigma_{\tau}$  and the TDOA equation defect was discussed in Sec. 4.2. The impact of the number of collects on TDOA3 and TDOA4 accuracy is investigated in Sec. 4.5. An additional factor that influences TDOA and T/FDOA geolocation is the observation geometry of the SVs during a signal collect.

Observability in geolocation describes how well a unique solution for the transmitter can be determined based on observations [3]. Poor observability leads to a near-singular matrix in the TDOA and T/FDOA algorithms, which causes inaccurate matrix inversion. Also note that observability is not affected by measurement noise, but by collection geometry. More diverse SV relative geometries at the time of signal collection yield good observability. The GDOP due to collection geometry can be found in [3] and [23].

The observability error has a much greater influence on TDOA4 error (Fig. 42) than TDOA3 error for this case. The TDOA4 error has a similar trend to TDOA3 but the total TDOA4 error is more than 10 times the magnitude of TDOA3. TDOA4

is much more sensitive to poor observation geometry and increase in slant range.

# 4.3.3 TFDOA2 Sensitivity to Pass Geometry

The T/FDOA algorithms exhibit slightly different behavior than AOA and TDOA (Figs. 43, 44, 45). Firstly, observability has a more visible effect in the ITL error trend seen in Figs. 41 and 42. Guo [3] showed that the T/FDOA error is greater in the direction of SV velocity, because  $\mathbf{G}_1$  found in Eq. A.50 is not invertible. This effect is seen in Figs. 43, 44, and 45. A "dip" is seen in each of the T/FDOA plots, showing that the middle pass is where neither poor observability error nor large slant range error dominate. Thus in the case where the TDOA and FDOA measurement error is close to the CAF CRLB, "middle" passes are best for geolocation accuracy.

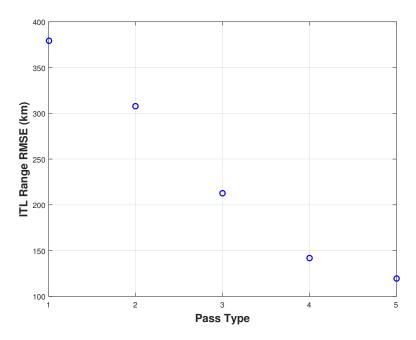


Figure 43. TFDOA2 algorithm sensitivity to pass geometry (Tx 1, 2000 trials,  $\sigma_{\tau} = CRLB$ ,  $\sigma_{\dot{\tau}} = CRLB$ )

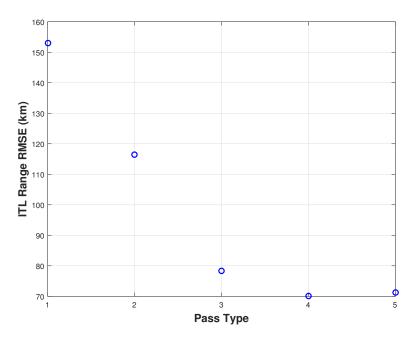


Figure 44. TFDOA3 algorithm sensitivity to pass geometry (Tx 1, 2000 trials,  $\sigma_{\tau} = CRLB$ ,  $\sigma_{\dot{\tau}} = CRLB$ )

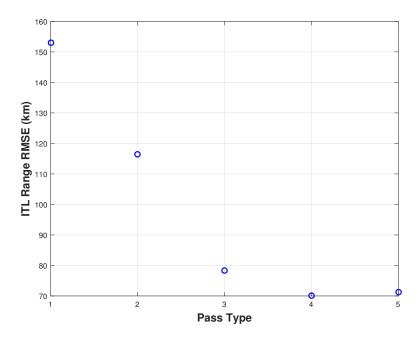


Figure 45. TFDOA4 algorithm sensitivity to pass geometry (Tx 1, 2000 trials,  $\sigma_{\tau} = CRLB$ ,  $\sigma_{\dot{\tau}} = CRLB$ )

# 4.3.4 Pass Geometry Sensitivity Summary

In general, passes at the horizon yield more inaccurate ITL solutions than overhead passes. There are three effects seen: 1) observation error, 2) slant range, and 3) measurement error. For TDOA and T/FDOA algorithms, passes overhead incur errors due to poor observation geometry. All algorithms are inaccurate due to large slant range when passes are at the horizon. And thirdly, the elevation and slant range influence measurement error for each of the algorithms. In the results discussed in this section the measurement error is modeled as the MUSIC and CAF CRLB, so increase in elevation and slant range increases error in all cases.

For AOA, TDOA3, and TDOA4, the ITL error increases as passes become closer to the horizon. The exception is that TDOA3 and TDOA4 experience observation error in overhead passes, and TDOA4 has a very large observation error. For each of the T/FDOA algorithms, middle passes, i.e. passes neither at the horizon nor overhead, yield the highest ITL accuracy. Looking at all algorithms combined, middle passes generate the most consistent ITL accuracy, as they strike a balance between observation error and measurement error due to slant range. Furthermore, horizon passes tend to generate more ITL error. These trends are valid for SVs whose measurement error increases similarly to the MUSIC and CAF CRLB, i.e. increases with slant range.

### 4.4 ITL Sensitivity to Baseline Distance

The baseline distance  $\Delta b$  is the approximate relative distance between the SVs for the duration of a pass (See Fig. 17). As previously mentioned, the effects of cluster geometry on ITL accuracy were not examined in this research, however this analysis details how changing baseline distance in general effects geolocation accuracy. It can be seen in Fig. 46 that for each of the multi-SV algorithms greater baseline

distance directly correlates to greater geolocation accuracy. Smaller baseline distance decreases observability.

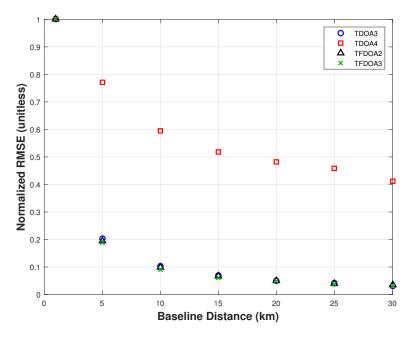


Figure 46. TDOA and T/FDOA algorithm sensitivity to baseline distance between SVs (2000 trials)

### 4.5 ITL Sensitivity to the Number of Signal Collects

Another factor that influences geolocation accuracy is the number of measurements received, or signal collects. For review, a collect is defined as a discrete instance where all SVs in the cluster receive the same signal of interest. For AOA geolocation, more signal collects means more lines of bearing, and more LOBs can lead to a more accurate LS intersection estimate. The TDOA and T/FDOA algorithms only require a single signal collect at each of the SVs to obtain an ITL solution. This analysis was conducted to determine whether more received signal collects during the course of a pass would increase geolocation accuracy from a batch processing standpoint. Note, this average is not weighted by measurement uncertainty or collection geometry. First, the ITL solutions were computed with 2 collects. For AOA, this signifies

2 LOBs being intersected. For the other algorithms, 2 ITL solutions (1 per collect) were averaged together. Then the number of collects was increased to 4, meaning the previous two collects and an additional 2 were used to obtain new ITL results. This was carried on until the case with 20 collects.

#### 4.5.1 ITL Sensitivity to Collection Geometry

Before observing the effect of increasing the number of collects it is important to note that for the TDOA and T/FDOA algorithms M discrete collects leads to M discrete ITL solutions. Since a non-weighted average is taken of these M solutions, the overall solution could decrease if certain collects are more inaccurate due to poor collection geometry. While GDOP is not analyzed in this research, Fig. 47 is an example of how 10 good collects lead to 10 ITL solutions close to the true transmitter, while Fig. 48 shows how 10 poor collects leads to a more dispersed group of 10 ITL solutions.

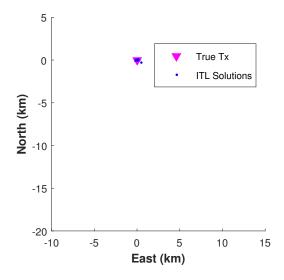


Figure 47. 10 ITL solutions obtained from 10 collects with good geometry (TFDOA4 algorithm, Tx 1, Pass 3)

Since algorithms are sensitive to collection geometry, the method of adding the number of collects was important. Two methods were tested. In the first case (Fig.

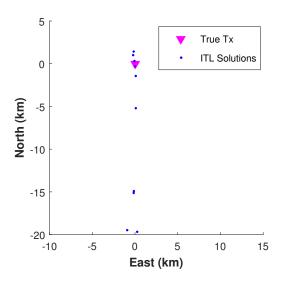


Figure 48. 10 ITL solutions obtained from 10 collects with poor geometry. (TFDOA4 algorithm, Tx 1, Pass 3)

49), the initial two collects were of poor geometry (at the horizon), and the collects added were increasingly better. In the second case (Fig. 50) the initial 2 collects were the best geometry possible, that is the smallest slant range, and the collects added were increasingly worse due to slant range.

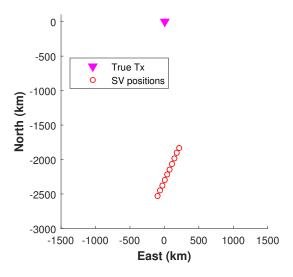


Figure 49. Collection geometry for Case 1. (Tx 1, Pass 3, 10 Collects)

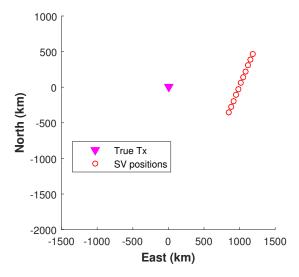


Figure 50. Collection geometry for Case 2. (Tx 1, Pass 3, 10 Collects)

# 4.5.2 Case 1: Addition of "Better" Signal Collects

For the collection geometry in Case 1, shown in Fig. 49, the number of collects was varied and the resulting non-weighted ITL average for each case was calculated. This process was repeated for 2000 trials, and the RMSE of the 2000 non-weighted averages was obtained. Then the results were normalized to observe the trends of the different algorithms simultaneously. Figs. 51 and 52 contain the effect of the number of collects on the ITL average for Case 1. The results are divided into the unconstrained and constrained ITL algorithms, where constrained includes those which utilize an Earth's surface constraint to obtain an ITL solution (TDOA3, TFDOA2, TFDOA3, TFDOA4).

It is seen in Figs. 51 and 52 that regardless of the ITL algorithm, accuracy of the non-weighted average was improved with the addition of "better" collects. This result is to be expected. ITL solutions computed using better measurements should be more accurate in all cases.

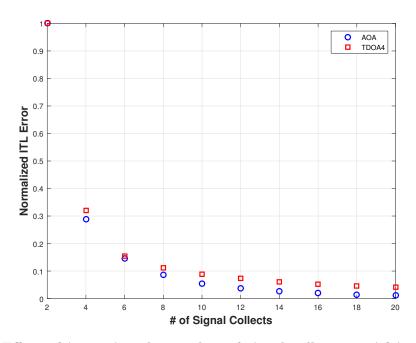


Figure 51. Effect of increasing the number of signal collects on AOA and TDOA4 accuracy for Case 1 (Tx 1, Pass 3, 2000 trials,  $\sigma = CRLB$ )

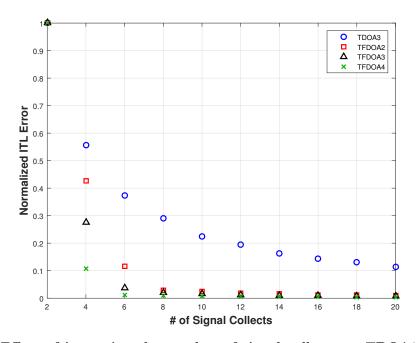


Figure 52. Effect of increasing the number of signal collects on TDOA3, TFDOA2, TFDOA3, and TFDOA4 accuracy for Case 1 (Tx 1, Pass 3, 2000 trials,  $\sigma = CRLB$ )

# 4.5.3 Case 2: Addition of "Worse" Signal Collects

The same process of varying the number of collects was executed again utilizing the collection geometry from Case 2 (Fig. 50). Figs. 53 and 54 contain the effect of increasing the number of collects for this case. Fig. 53 contains results for the unconstrained algorithms, and Fig. 54 is for the constrained algorithms.

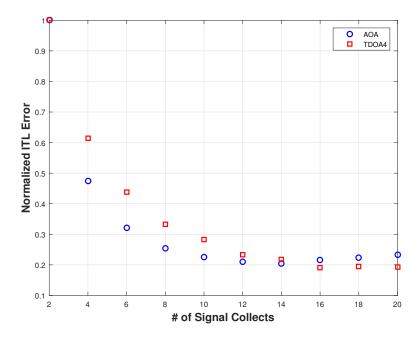


Figure 53. Effect of increasing the number of signal collects on AOA and TDOA4 accuracy for Case 2 (Tx 1, Pass 3, 2000 trials,  $\sigma = CRLB$ )

It is seen from Fig. 53 that even though the quality of additional signal collects is increasingly worse, the accuracy of the AOA and TDOA4 algorithms generally increases with the number of collects. Note that the results calculated were for the AOA LS intersection method and the TDOA4 non-weighted ITL average. This shows that for AOA and TDOA4 in this scenario, more signal collects benefits the overall accuracy even when a non-weighted average is being utilized. The trend seen here for AOA and TDOA4 was also true for Passes 1-2 and 4-5. Future work could investigate an even wider range of collection geometries to see if this trend remains constant.

Fig. 54 shows that the accuracy of the non-weighted ITL average decreases even

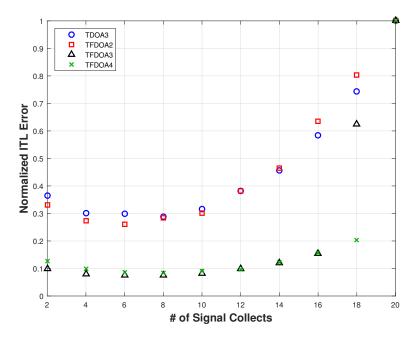


Figure 54. Effect of increasing the number of signal collects on TDOA3, TFDOA2, TFDOA3, and TFDOA4 accuracy for Case 2 (Tx 1, Pass 3, 2000 trials,  $\sigma = CRLB$ )

though more signal collects were added. What these algorithms (TDOA3, T/FDOA) each have in common is that they incorporate the transmitter altitude constraint. The constrained ITL solutions are sensitive to collection geometry, so that ITL solutions calculated using collects at the horizon should be expected to degrade overall ITL accuracy if a simple non-weighted average is being used. It is recommended that a weighted average is used in the presence of multiple signal collects in order to see the benefit of more collects regardless of their uncertainty.

Furthermore, it is observed from Figs. 51 - 53 that for this scenario, approximately 10-15 collects are desirable. After 10-15 collects the overall accuracy does not significantly change.

### 4.5.4 Number of Collects Sensitivity Summary

For the non-weighted average approach used in this analysis, increasing the number of signal collects improved ITL accuracy for AOA and TDOA4, regardless of the

certainty of the collects being added. For TDOA3 and the T/FDOA algorithms, increasing the number of signal collects only improved the average ITL solution when the collection geometry was better. Thus the constrained ITL algorithms (those that utilize Tx altitude constraint) are more sensitive to collection geometry than the unconstrained ITL algorithms (AOA and TDOA4) tested.

The overall ITL accuracy for multiple collects is influenced by the collection geometry, measurement error, and the method of averaging ITL solutions. It is concluded that for the constrained algorithms (TDOA3 and T/FDOA), a weighted average should be utilized to take into account geometry and measurement error for each signal collect. As discussed in Chapter 5, this research employs ML estimation and a DTED1 grid search after using the ITL average as an initial guess, so a non-weighted average was sufficient. But if the ITL average is being used for a final geolocation solution, using a weighted average is recommended.

The problem with using a weighted average is that when SVs obtain measurements on orbit, the collection geometry could be unknown since the location of the transmitter is unknown. Two possible solutions for determining the collection geometry could be to 1) design a SV payload that can sense the signal's AOA in addition to T/FDOA or 2) compute an ITL solution, then use the ITL to recursively estimate collection geometry.

# 4.6 ITL Sensitivity to SV Location Error

The accuracy of GPS receivers in determining SV position and velocity has improved over the years, making them a good choice for on-board CubeSat navigation, but there is still enough location error present to affect RF geolocation accuracy. The effect of absolute and relative SV position and velocity error on geolocation accuracy is analyzed in this section. The method of corrupting the SV positions and velocities

is seen in Sec. 3.5.1.

### 4.6.1 Absolute Position Knowledge Error

For each ITL algorithm (AOA, TDOA3, etc.) the geolocation error was calculated for different absolute position errors. The absolute position error can be thought of as the error in cluster positioning, with the exception of 1-SV AOA. Initially, the minimum number of collects was simulated to obtain a solution, and 10,000 trials were run for each increment of position error. The results for AOA and TDOA3 are seen in Figs. 55 and 56.

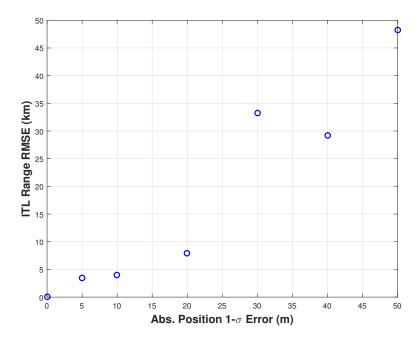


Figure 55. AOA algorithm sensitivity to absolute position error (Tx 1, Pass 3, 10 collects, 10,000 trials)

It was observed that the ITL error was highly sensitive to position error, the way it was modeled in the simulation, which was a random Gaussian variable in 3 ECEF directions. The number of trials was increased to 100,000 and the RMSE still fluctuated. This high sensitivity of the ITL algorithms was seen for each of the SV location error (absolute and relative position and velocity) analyses (See App. C).

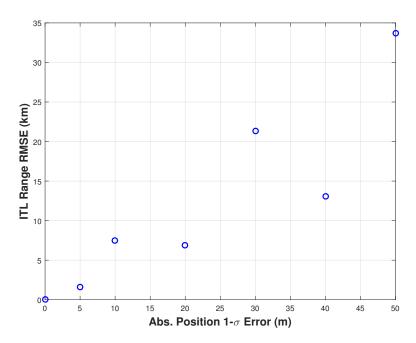


Figure 56. TDOA3 algorithm sensitivity to absolute position error (Tx 1, Pass 3, 1 collect, 10,000 trials)

Since random variables were generated independently for each trial, outliers may have caused increased ITL error, causing RMSE to be increased for a particular trial. It is concluded that a wide range of performance could be expected in the presence of SV location error, especially when only one or a few signal collects are obtained.

Then the simulation was rerun using 30 different signal collects, so that there was some more diversity in collection geometry. The ITL error due to absolute position knowledge error for this new configuration is seen in Figs. 57 - 62.

The effect of absolute position error on AOA error can be traced to Eq. A.5 in App. A.1. The origin of the line of bearing  $\mathbf{d}_0$  is corrupted when  $\mathbf{s}_1$  is corrupted.

The effect of absolute position error  $\mathbf{e}_p$  impact on TDOA error is observed from the general TDOA equation Eq. A.18 in App. A.2. Here Eq. A.18 is rewritten to

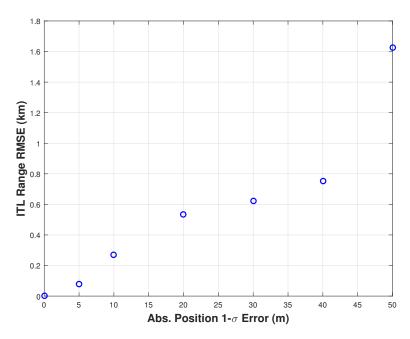


Figure 57. AOA algorithm sensitivity to absolute position error (Tx 1, Pass 3, 30 collects, 10,000 trials)

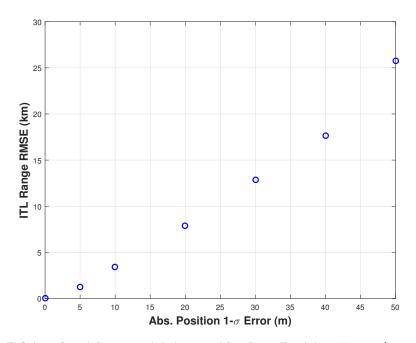


Figure 58. TDOA3 algorithm sensitivity to Absolute Position Error (Tx 1, Pass 3, 30 collects, 10,000 trials)

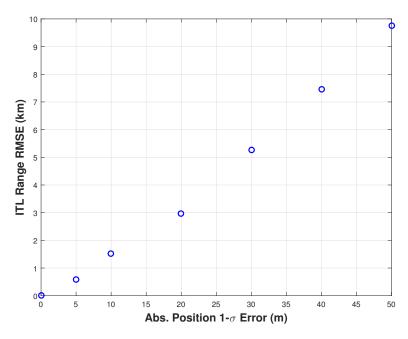


Figure 59. TDOA4 algorithm sensitivity to absolute position error (Tx 1, Pass 3, 30 collects, 10,000 trials)

include  $\tilde{\mathbf{s}}_i$  which is defined as  $\mathbf{s}_i + \mathbf{e}_p$ .

$$r_{i1}^{2} + 2\rho_{1}r_{i1} = \tilde{\mathbf{s}}_{i}^{T}\tilde{\mathbf{s}}_{i} - \tilde{\mathbf{s}}_{1}^{T}\tilde{\mathbf{s}}_{1} - 2(\mathbf{s}_{i} - \mathbf{s}_{1})^{T}\mathbf{u}$$

$$r_{i1}^{2} + 2\rho_{1}r_{i1} = (\mathbf{s}_{i} + \mathbf{e}_{p})^{T}(\mathbf{s}_{i} + \mathbf{e}_{p}) - (\mathbf{s}_{1} + \mathbf{e}_{p})^{T}(\mathbf{s}_{1} + \mathbf{e}_{p}) - 2(\mathbf{s}_{i} - \mathbf{s}_{1})^{T}\mathbf{u}$$

$$(4.3)$$

An increase of the absolute position error  $\mathbf{e}_p$  leads to an increase in TDOA equation defect.

The general T/FDOA equation defect is also influenced by position error, similar to the TDOA equation. The T/FDOA algorithms utilize the TDOA equation Eq. 4.3, but also the general T/FDOA equation Eq. A.48 in App. A.3.1. The T/FDOA equation is rewritten with  $\tilde{\mathbf{s}}_i = \mathbf{s}_i + \mathbf{e}_p$  in Eq. 4.4.

$$2r_{i1}\dot{r}_{i1} + 2r_{i1}\dot{\rho}_1 + 2\dot{r}_{i1}\rho_1 - 2\tilde{\mathbf{s}}_i^T\dot{\mathbf{s}}_i + 2\tilde{\mathbf{s}}_1^T\dot{\mathbf{s}}_1 = -2(\dot{\mathbf{s}}_i - \dot{\mathbf{s}}_1)^T\mathbf{u} \qquad i = 2, 3, ..., S \quad (4.4)$$

 $\tilde{\mathbf{s}}_i$  is substituted with  $\mathbf{s}_i + \mathbf{e}_p$  and the 4th and 5th terms of Eq. 4.4 are expanded in

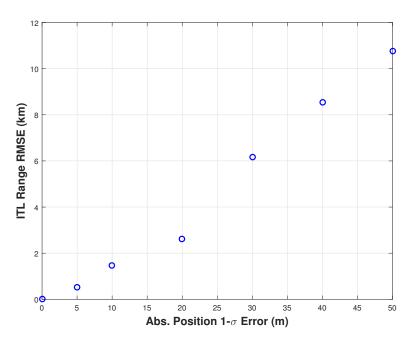


Figure 60. TFDOA2 algorithm sensitivity to absolute position error (Tx 1, Pass 3, 30 collects, 10,000 trials)

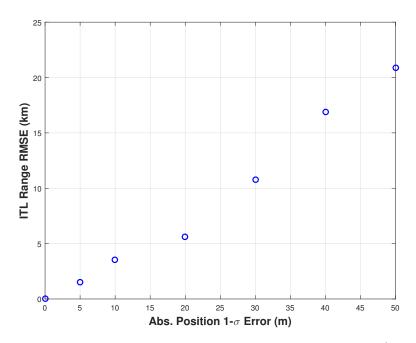


Figure 61. TFDOA3 algorithm sensitivity to absolute position error (Tx 1, Pass 3, 30 collects, 10,000 trials)

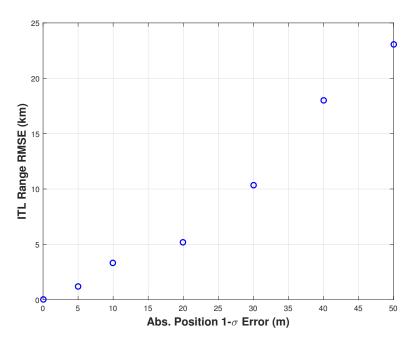


Figure 62. TFDOA4 algorithm sensitivity to absolute position error (Tx 1, Pass 3, 30 collects, 10,000 trials)

Eq. 4.5.

$$-2\tilde{\mathbf{s}}_{i}^{T}\dot{\mathbf{s}}_{i} + 2\tilde{\mathbf{s}}_{1}^{T}\dot{\mathbf{s}}_{1} = -2(\mathbf{s}_{i} + \mathbf{e}_{p})^{T}\dot{\mathbf{s}}_{i} + 2(\mathbf{s}_{1} + \mathbf{e}_{p})^{T}\dot{\mathbf{s}}_{1}$$

$$= -2\mathbf{s}_{i}^{T}\dot{\mathbf{s}}_{i} - 2\mathbf{e}_{p}^{T}\dot{\mathbf{s}}_{i} + 2\mathbf{s}_{1}^{T}\dot{\mathbf{s}}_{1} + 2\mathbf{e}_{p}^{T}\dot{\mathbf{s}}_{1}$$

$$= -2\mathbf{s}_{i}^{T}\dot{\mathbf{s}}_{i} + 2\mathbf{s}_{1}^{T}\dot{\mathbf{s}}_{1} - 2\mathbf{e}_{p}^{T}(\dot{\mathbf{s}}_{i} - \dot{\mathbf{s}}_{1})$$

$$(4.5)$$

It is seen in Eq. 4.5 how an increase in  $\mathbf{e}_p$  influences the 4th and 5th terms of the general T/FDOA equation, leading to increased equation defect.

For the case with 30 different signal collects, which is the case with a wider range of geometric diversity, the AOA, TDOA, and T/FDOA algorithms displayed a nearly linear response to absolute position error. Different results could be expected if the SV position error was modeled differently, that is other than independent Gaussian random variables of equal uncertainty in all three ECEF directions, and if the collection geometry was less diverse, as observed in Figs. 55 and 56.

# 4.6.2 Absolute Velocity Knowledge Error

The absolute velocity error is only factored into the T/FDOA algorithms because they must be related to the frequency difference measurements according to the doppler equation Eq. 2.8. The ITL error due to absolute velocity knowledge error for the 30-collect case is seen in Figs. 109 - 111. It is seen that for TF-

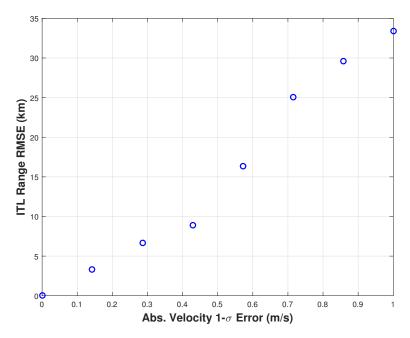


Figure 63. TFDOA2 algorithm sensitivity to absolute velocity error (Tx 1, Pass 3, 30 collects, 10,000 trials)

DOA2 (Fig. 63) the ITL error increases nearly linearly with absolute velocity error for this case. The TFDOA3 and TFDOA4 algorithms are less sensitive to absolute velocity error. The ITL error for TFDOA3 and T/FDOA is less than 2 km for all of the velocity errors tested. There is fluctuation in the ITL error for TFDOA3 and TFDOA4, but as previously explained and seen in App. C the algorithms are highly sensitive to SV location error the way it was modeled in this research. There were outliers in the noise realizations for a few of the cases that caused the TFDOA3 or TFDOA4 error to be magnified.

The second T/FDOA equation Eq. A.48 found in App. A.3.1 can be observed to

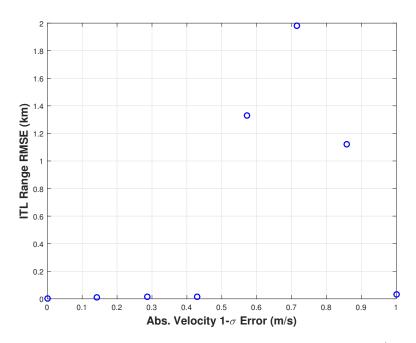


Figure 64. TFDOA3 algorithm sensitivity to absolute velocity error (Tx 1, Pass 3, 30 collects, 10,000 trials)

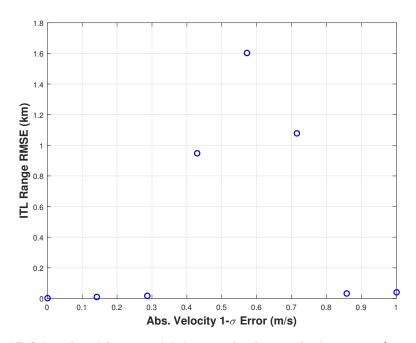


Figure 65. TFDOA4 algorithm sensitivity to absolute velocity error (Tx 1, Pass 3, 30 collects, 10,000 trials)

see how absolute velocity error impacts T/FDOA equation defect. The 4th and 5th terms in Eq. A.48 are corrupted in the presence absolute velocity error.

$$2r_{i1}\dot{r}_{i1} + 2r_{i1}\dot{\rho}_1 + 2\dot{r}_{i1}\rho_1 - 2\mathbf{s}_i^T\tilde{\mathbf{s}}_i + 2\mathbf{s}_1^T\tilde{\mathbf{s}}_1 = -2(\dot{\mathbf{s}}_i - \dot{\mathbf{s}}_1)^T\mathbf{u} \qquad i = 2, 3, ..., S \quad (4.6)$$

If  $\tilde{\mathbf{s}}_i$  is defined as  $\dot{\mathbf{s}}_i + \mathbf{e}_v$ , then the 4th and 5th term can be rewritten and simplified to observe the effect of  $\mathbf{e}_v$  as seen in Eq. 4.7. Notice that the term on the right side of Eq. 4.6 is impacted by relative velocity error, so it will be ignored here.

$$-2\mathbf{s}_{i}^{T}\tilde{\mathbf{s}}_{i} + 2\mathbf{s}_{1}^{T}\tilde{\mathbf{s}}_{1} = -2\mathbf{s}_{i}^{T}(\dot{\mathbf{s}}_{i} + \mathbf{e}_{v}) + 2\mathbf{s}_{1}^{T}(\dot{\mathbf{s}}_{1} + \mathbf{e}_{v})$$

$$= -2\mathbf{s}_{i}^{T}\dot{\mathbf{s}}_{i} - 2\mathbf{s}_{i}^{T}\mathbf{e}_{v} + 2\mathbf{s}_{1}^{T}\dot{\mathbf{s}}_{1} + 2\mathbf{s}_{1}^{T}\mathbf{e}_{v}$$

$$= -2\mathbf{s}_{i}^{T}\dot{\mathbf{s}}_{i} + 2\mathbf{s}_{1}^{T}\dot{\mathbf{s}}_{1} - 2(\mathbf{s}_{i}^{T} - \mathbf{s}_{1}^{T})\mathbf{e}_{v}$$

$$(4.7)$$

Therefore the magnitude of equation defect is related to  $\mathbf{e}_v$  by the true difference in SV ECEF positions.

### 4.6.3 Relative Position Knowledge Error

The effect of relative position knowledge error on ITL accuracy is seen in Figs. 66 - 70. It is seen that compared with the error in absolute position and velocity, relative position error is costly for ITL accuracy. In addition, the trends seen in Figs. 69 and 70 show that for this case TFDOA3 and TFDOA4 were highly sensitive to relative position error. It is important to note that these results fluctuate greatly based on the collection geometry. For example, in App. C the TFDOA3 and TFDOA4 error as a function of relative position error for only 1 collect in Pass 3 is seen in Figs. 115 and 116. The change in the collection diversity greatly influences the impact of position error, and even when the collection geometry is held constant the trend in resulting ITL error is unclear. Another effect observed is that the TDOA4 error is the

largest comparatively and it varies almost logarithmically with relative position error. Recall that does not necessarily mean the algorithm is worse in general, because it is not utilizing the surface of the Earth assumption like the other TDOA and T/FDOA algorithms.

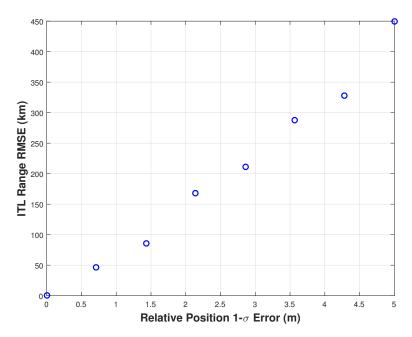


Figure 66. TDOA3 algorithm sensitivity to relative position error (Tx 1, Pass 3, 30 collects, 10,000 trials)

The relative position accuracy has an effect on the TDOA and T/FDOA equation defect. Eq. 4.8 contains the general TDOA and T/FDOA equations and the corrupted variables due to relative position error.

$$r_{i1}^{2} + 2\rho_{1}r_{i1} = \tilde{\mathbf{s}}_{i}^{T}\tilde{\mathbf{s}}_{i} - \mathbf{s}_{1}^{T}\mathbf{s}_{1} - 2(\tilde{\mathbf{s}}_{i} - \mathbf{s}_{1})^{T}\mathbf{u} \qquad TDOA$$

$$2r_{i1}\dot{r}_{i1} + 2r_{i1}\dot{\rho}_{1} + 2\dot{r}_{i1}\rho_{1} - 2\tilde{\mathbf{s}}_{i}^{T}\dot{\mathbf{s}}_{i} + 2\mathbf{s}_{1}^{T}\dot{\mathbf{s}}_{1} = -2(\dot{\mathbf{s}}_{i} - \dot{\mathbf{s}}_{1})^{T}\mathbf{u} \qquad T/FDOA \qquad (4.8)$$

$$i = 2, 3, ..., S$$

If the absolute ECEF position of the  $i^{th}$  SV is defined with respect to the reference satellite  $\mathbf{s}_1$ , then the relative position error  $\mathbf{e}_{p,rel}$  impacts  $\tilde{\mathbf{s}}_i$  because of the way the

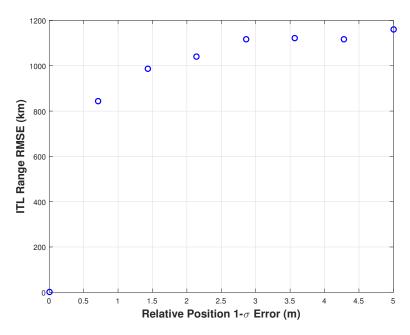


Figure 67. TDOA4 algorithm sensitivity to relative position error (Tx 1, Pass 3, 30 collects, 10,000 trials)

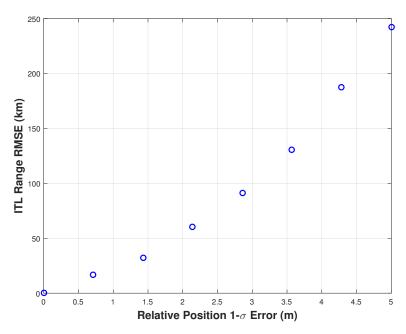


Figure 68. TFDOA2 algorithm sensitivity to relative position error (Tx 1, Pass 3, 30 collects, 10,000 trials)

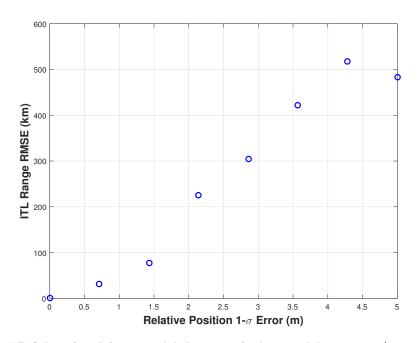


Figure 69. TFDOA3 algorithm sensitivity to relative position error (Tx 1, Pass 3, 30 collects, 10,000 trials)

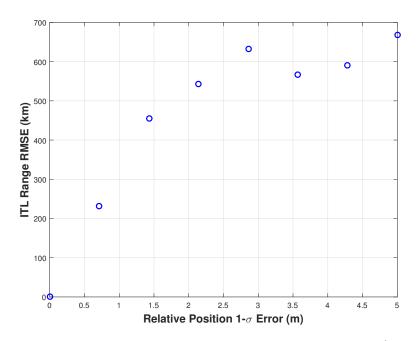


Figure 70. TFDOA4 algorithm sensitivity to relative position error (Tx 1, Pass 3, 30 collects, 10,000 trials)

relative orbits are determined in this research. Thus an increase in  $\mathbf{e}_{p,rel}$  affects terms 3 and 5 in the TDOA equation and term 4 in the T/FDOA equation, leading to overall ITL error.

#### 4.6.4 Relative Velocity Knowledge Error

The ITL accuracy as a function of relative velocity knowledge error  $\mathbf{e}_{v,rel}$  is seen in Figs. 71 - 73. For this case, dozens of cm/s could lead to hundreds of kilometers of T/FDOA error. The TFDOA3 algorithm can handle small relative velocity error well, but the response is also dependent on the collection geometry, so no sweeping conclusions can be made based on these results. The case with only 1 collect is seen in Figs. 117 - 119 in App. C. The relative velocity error only has impact on the

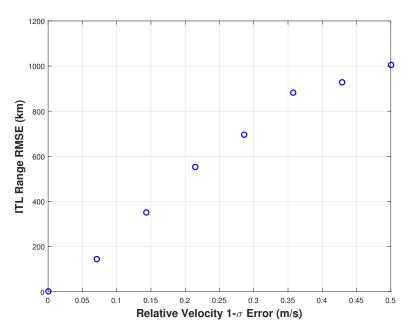


Figure 71. TFDOA2 algorithm sensitivity to relative velocity error (Tx 1, Pass 3, 30 collects, 10,000 trials)

T/FDOA equation. The T/FDOA equation is rewritten here to show the effect of relative velocity error. If the ECEF velocity of the  $i^{th}$  SV is defined with respect to

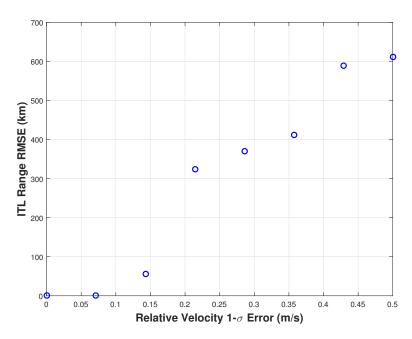


Figure 72. TFDOA3 algorithm sensitivity to relative velocity error (Tx 1, Pass 3, 30 collects, 10,000 trials)

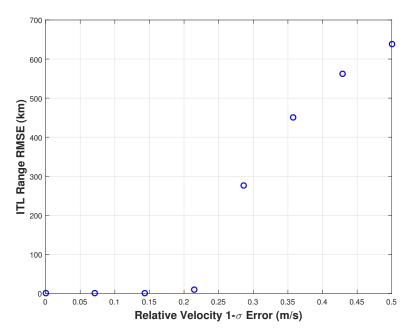


Figure 73. TFDOA4 algorithm sensitivity to relative velocity error (Tx 1, Pass 3, 30 collects, 10,000 trials)

the reference SV  $\dot{\mathbf{s}}_1$ , then  $\dot{\mathbf{s}}_i$  is corrupted.

$$2r_{i1}\dot{r}_{i1} + 2r_{i1}\dot{\rho}_1 + 2\dot{r}_{i1}\rho_1 - 2\mathbf{s}_i^T \tilde{\mathbf{s}}_i + 2\mathbf{s}_1^T \dot{\mathbf{s}}_1 = -2(\tilde{\mathbf{s}}_i - \dot{\mathbf{s}}_1)^T \mathbf{u} \qquad T/FDOA$$

$$i = 2, 3, ..., S$$
(4.9)

The 4th and 6th terms are corrupted as the magnitude of  $\mathbf{e}_{v,rel}$  increases. The impact of  $\mathbf{e}_{v,rel}$  on ITL error also depends on the SV locations and the transmitter location.

# 4.6.5 SV Location Error Sensitivity Summary

Overall, the results in this section show that the ITL algorithms are unstable in the presence of position and velocity error for the number of trials run. It is likely that increasing the number of trials beyond 100,000 could make the trends more visible. Furthermore, the effects of SV location error are highly dependent on the collection geometry. No sweeping conclusions were made based on these results except that increases in SV positioning error cause the ITL error to increase, and high positioning accuracy is crucial for geolocation accuracy.

#### 4.7 ITL Sensitivity to Measurement Error

The sensitivity of each of the ITL algorithms to AOA, TDOA, and FDOA measurement error has been explored to some extent in [4], [3], and [23]. The purpose of this section is to investigate the sensitivity of these algorithms to measurement noise for a 500km orbit CubeSat cluster.

#### 4.7.1 AOA Algorithm Sensitivity to AOA Measurement Error

The AOA measurement error  $(\sigma_{\alpha}, \sigma_{\epsilon})$  impact on AOA geolocation error is shown in Fig. 74. Note that this analysis focuses on AOA measurement error, but according (3.16) the attitude determination error  $\sigma_{att}$  could have the same effect. The relation-

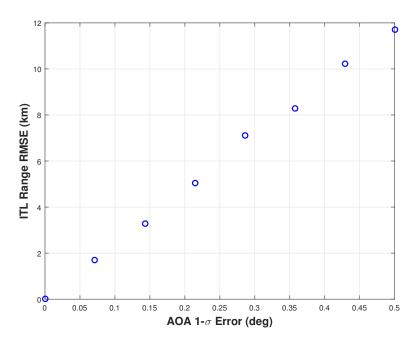


Figure 74. AOA algorithm sensitivity to angle measurement error (Tx 1, Pass 3, 2000 trials,  $\sigma_{\alpha} = \sigma_{\epsilon}$ )

ship between ITL and measurement error is nearly linear. The trend seen in Fig. 74 is intuitive geometrically. Fig. 32 provides a visual of the relation between angle error and estimate uncertainty. This relationship is indirect for the AOA algorithm since there is trigonometry and a LS intersection involved, but overall it was an expected result. Notice that errors of greater than 0.1 deg could yield error worse than 50 km. While this error could be diminished with ML estimation and the application of a DEM, it magnifies the importance of accurate angle measurement and attitude determination in a CubeSat geolocation system.

#### 4.7.2 ITL Sensitivity to Differential Time Offset Error

The ITL error as a function of DTO error  $\sigma_{dto}$  was investigated. The effect of DTO error on ITL error is shown in Figs. 75 - 79. The weighting matrix **W** in the TFDOA3 algorithm (same as TFDOA4) was set to identity, even though the DFO error  $\sigma_{dfo}$  was zero for this analysis. Note that the magnitude of ITL error for the

T/FDOA algorithms is optimistic, because in reality  $\sigma_{dfo}$  would be nonzero.

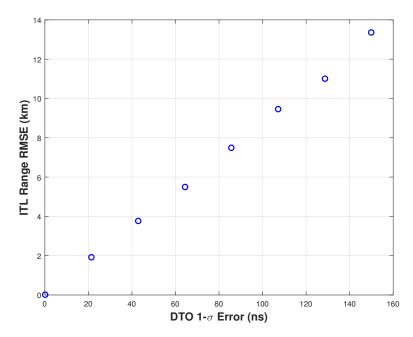


Figure 75. TDOA3 algorithm sensitivity to DTO error (Tx 1, Pass 3, 2000 trials,  $\sigma_f = 0Hz$ )

It is seen from Figs. 75 - 79 that the ITL error increases with DTO error, as expected. Furthermore, the ITL error relationship is nearly linear for the DTO errors observed, with the exception of TDOA4. It was reaffirmed that TDOA4 is most sensitive to measurement error, with nearly 800 km RMSE for 150 ns DTO error. The other algorithms have ITL RMSE of 25 km or less. In addition, the TDOA3 and TFDOA2 algorithm are almost identically sensitive to DTO error for this case of zero DFO error.

The DTO error impacts the TDOA and T/FDOA equation errors, which in turn influences the algorithm accuracy. The general TDOA and T/FDOA equations for corrupted measurements are seen in Eq. 4.10. TDOA measurements  $\tau$  are converted

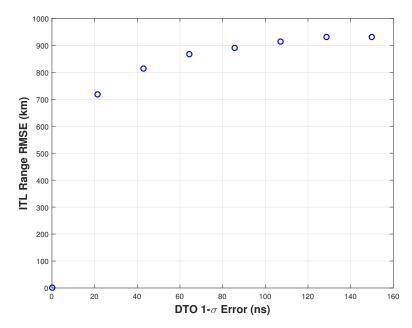


Figure 76. TDOA4 algorithm sensitivity to DTO error (Tx 1, Pass 3, 2000 trials,  $\sigma_f = 0Hz$ )

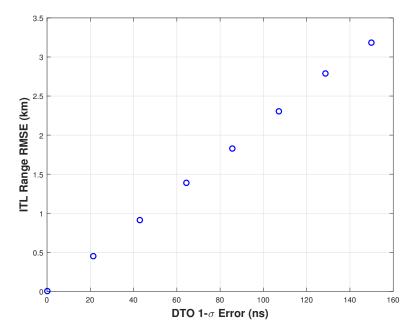


Figure 77. TFDOA2 algorithm sensitivity to DTO error (Tx 1, Pass 3, 2000 trials,  $\sigma_f = 0 Hz$ )

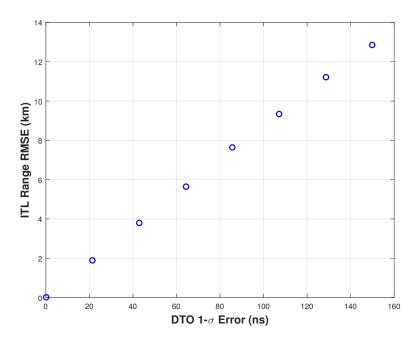


Figure 78. TFDOA3 algorithm sensitivity to DTO error (Tx 1, Pass 3, 2000 trials,  $\sigma_f = 0Hz$ )

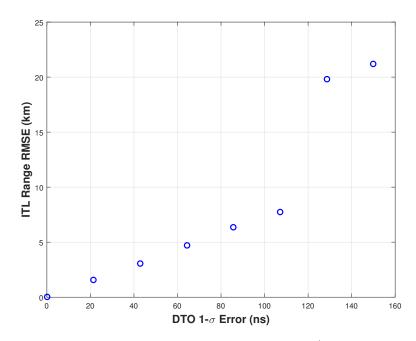


Figure 79. TFDOA4 algorithm sensitivity to DTO error (Tx 1, Pass 3, 2000 trials,  $\sigma_f=0Hz)$ 

to range differences  $r_{i1}$  according to Eq. 2.5.

$$\tilde{r}_{i1}^{2} + 2\rho_{1}\tilde{r}_{i1} = \mathbf{s}_{i}^{T}\mathbf{s}_{i} - \mathbf{s}_{1}^{T}\mathbf{s}_{1} - 2(\mathbf{s}_{i} - \mathbf{s}_{1})^{T}\mathbf{u} \qquad TDOA$$

$$2\tilde{r}_{i1}\dot{r}_{i1} + 2\tilde{r}_{i1}\dot{\rho}_{1} + 2\dot{r}_{i1}\rho_{1} - 2\mathbf{s}_{i}^{T}\dot{\mathbf{s}}_{i} + 2\mathbf{s}_{1}^{T}\dot{\mathbf{s}}_{1} = -2(\dot{\mathbf{s}}_{i} - \dot{\mathbf{s}}_{1})^{T}\mathbf{u} \qquad T/FDOA \qquad (4.10)$$

$$i = 2, 3, ..., S$$

It can be observed in Eq. 4.10 that when all other variables are held constant, a more corrupt  $\tilde{r}_{i1}$  leads to greater equation defect.

# 4.7.3 ITL Sensitivity to Differential Frequency Offset Error

The effect of DFO error  $\sigma_{dfo}$  on ITL accuracy is seen in Figs. 80 - 82. Note that the weighting matrix **W** in the TFDOA3 algorithm was set to identity, even though the DTO error  $\sigma_{dto}$  was zero. As expected, the accuracy of the T/FDOA

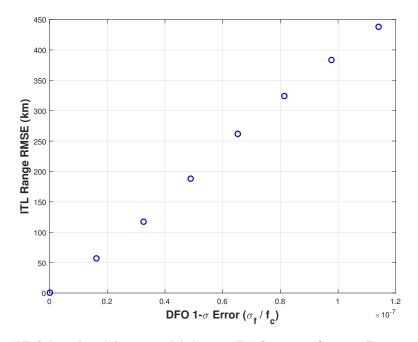


Figure 80. TFDOA2 algorithm sensitivity to DFO error (Tx 1, Pass 3, 2000 trials,  $\sigma_{\tau} = 0s$ )

algorithms increased as the number of SVs is increased. More SVs allows for more measurements, leading to more accurate estimates. The DFO error impacts the range

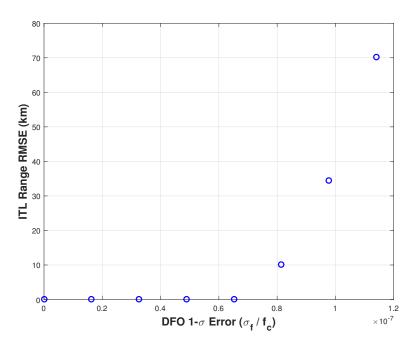


Figure 81. TFDOA3 algorithm sensitivity to DFO error (Tx 1, Pass 3, 2000 trials,  $\sigma_{\tau}=0s$ )

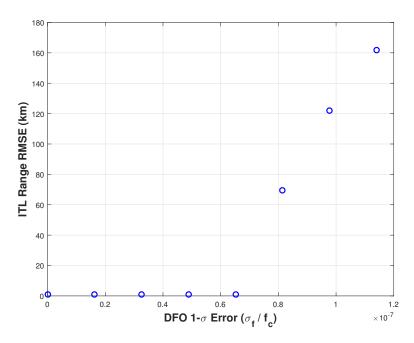


Figure 82. TFDOA4 algorithm sensitivity to DFO error (Tx 1, Pass 3, 2000 trials,  $\sigma_{\tau}=0s$ )

rate measurements  $\dot{r}_{i1}$  which are derived from the frequency difference measurements  $\dot{\tau}$  (Eq. 2.6).

$$2r_{i1}\tilde{r}_{i1} + 2r_{i1}\dot{\rho}_1 + 2\tilde{r}_{i1}\rho_1 - 2\mathbf{s}_i^T\dot{\mathbf{s}}_i + 2\mathbf{s}_1^T\dot{\mathbf{s}}_1 = -2(\dot{\mathbf{s}}_i - \dot{\mathbf{s}}_1)^T\mathbf{u} \qquad T/FDOA$$

$$i = 2, 3, ..., S$$
(4.11)

The 1st and 3rd terms of the T/FDOA equation Eq. 4.11 are corrupted by increase in DFO error.

#### 4.8 Summary

The sensitivity of the initial transmitter localization (ITL) algorithms, namely AOA, TDOA3, TDOA4, TFDOA2, TFDOA3, and TFDOA4, to different system parameters was analyzed. Although each algorithm has its strengths and weaknesses, and they cannot be fully compared and constrasted, there were some general trends observed. The TDOA4 method from [24] utilized in this research does not require the transmitter to be Earth-constrained, so it is solving a slightly different problem. Even so, it is important to note that TDOA4 displayed the greatest ITL error amongst all the methods, so for the purposes of conducting strictly geolocation of surface-constrained transmitters or even low altitude aerial vehicles, it could be advantageous to explore the constrained version of TDOA4 derived in [23].

Furthermore, in practice TDOA3, TDOA4, and TFDOA2 were problematic in the presence of high measurement or navigation errors. While these algorithms only require one set of measurements, or one collect, to obtain an ITL solution, there are times when the solution is out of the coverage area or more than hundreds of kilometers away from the true transmitter location. These erroneous solutions must be identified and discarded. Another problem is solution ambiguity. It was assumed in this chapter that multiple ITL solutions could be disambiguated, but this could be

more challenging in practice, especially with TFDOA2 where in some cases there are two viable solutions in the coverage area. The ITL algorithms themselves are found in detail in App. A, and some further conclusions are discussed in Sec. 6.1.

As seen throughout this chapter, the ITL solutions themselves are very inaccurate in the presence of measurement noise, navigation error, and poor collection geometry. However, depending on the application, these ITL solutions can be very useful as initial guesses for further estimation techniques, such as a Kalman filter or the iterative Gauss-Newton algorithm used in this thesis to find the maximum likelihood estimate.

# 5. System Level Performance

This chapter contains 4 major sections. Sec. 5.1 and Sec. 5.2 are intermediate analyses. Sec. 5.1 is an investigation of how the surface of the earth constraint utilized for the TDOA3, TFDOA2, and TFDOA3 algorithms impacts geolocation accuracy. Sec. 5.2 demonstrates the benefit of implementing maximum likelihood estimation and a DTED1 grid search. Sec. 5.3 is a geolocation performance analysis of a 1-4 CubeSat cluster in a 500km orbit. Sec. 5.4 contains the process of utilizing the simulation to obtain a geolocation system design based on requirements.

# 5.1 Effect of Earth's Surface Constraint on Accuracy

It was established in Sec. 2.4.4 that executing the ITL algorithm with an incorrect transmitter altitude assumption leads to geolocation error [3,23]. This section compares three different Earth's surface constraints: spherical Earth, WGS84, and Level 0 DTED (DTED0). It is demonstrated how using a DTED0 Earth constraint for the TDOA3, TFDOA2, TFDOA3, and TFDOA4 algorithms greatly improves geolocation accuracy, thus justifying its use in the geolocation simulation.

Methods For each ITL algorithm requiring an altitude assumption (TDOA3, TFDOA2, TFDOA3, and TFDOA4), three Earth constraints were tested: 1) Spherical Earth with mean radius 6371km, 2) WGS84 Ellipsoid, and 3) DTED0 (GMTED 2010, see Sec. 2.6). The method of applying the WGS84 and DTED0 constraints is discussed in App. A.2.2.

It is assumed that the transmitter is constrained to the Earth's surface, so for the purposes of this analysis the altitude is assumed to be the Earth's geocentric radius  $r_e$  at the transmitter's latitude and longitude.

In reality, the land elevation varies with latitude and longitude, so  $r_e$  is variable. For the WGS84 and DTED0 surfaces, the elevation at the transmitter location can be expressed as an ellipsoid height  $h_u$ . The height  $h_u$ , can be converted to a geocentric radius  $r_e$  if the latitude and longitude are known. If the transmitter location is unknown, then its altitude  $r_e$  is also unknown, but can be estimated. The estimated altitude  $\tilde{r}_e$  is shown in (5.1).

$$\tilde{r}_e = r_e + e_{alt} \tag{5.1}$$

The corrupt altitude  $\tilde{r}_e$  is an input for the three ITL algorithms mentioned above. For this analysis, a single noise-free geolocation scenario was used to observe how a corrupt input altitude  $\tilde{r}_e$  affects ITL accuracy when 3 different Earth constraints are used.

For each Earth constraint and ITL algorithm, the initial altitude  $\tilde{r}_e$  was corrupted with altitude errors  $e_{alt}$  ranging from 0-10 km. These input altitude errors form the x-axis of Figs. 83 and 84. There were two results recorded for this test: the output altitude error (83) and the ITL accuracy 84. The method of implementing the WGS84 and DTED0 Earth constraints required updating the altitude guess based on the transmitter location estimate  $\hat{\mathbf{u}}$ , so the output altitude error is the difference between final altitude estimate  $r_f$  and the truth  $r_e$ . The ITL accuracy in Fig. 84 is simply the accuracy of  $\hat{\mathbf{u}}$  obtained by the TDOA3 algorithm. TFDOA2, TFDOA3, and TFDOA4 algorithm results were omitted because the results were redundant.

**Results** The output altitude error and ITL error for different input altitude errors are seen in Figs. 83 and 84. Note that the trends in Fig. 83 and Fig. 84 are identical. Together the graphs show how an inaccurate estimate of the transmitter altitude leads to an inaccurate estimate of the transmitter ECEF location  $\hat{\mathbf{u}}$ .

For the spherical Earth constraint, Fig. 83 shows that the output altitude error

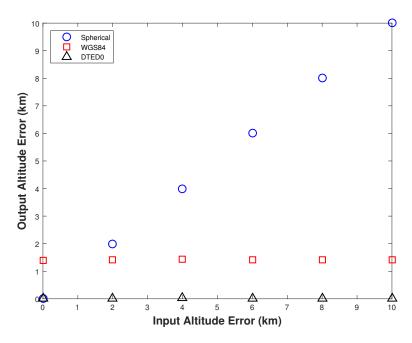


Figure 83. TDOA3 final  $h_u$  error for three different surface of the Earth constraints (Tx 4 with true WGS84 height = 1.39 km, Pass 3)

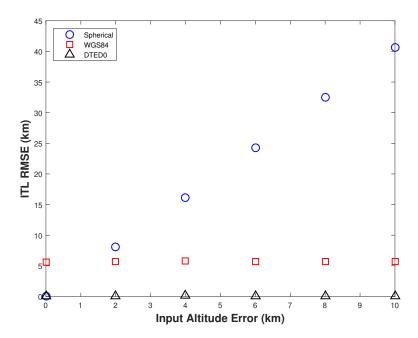


Figure 84. TDOA3 geolocation error for three different surface of the Earth constraints (Tx 4 with true WGS84 height = 1.39 km, Pass 3)

is the same as the input altitude error, which is to be expected, since no iteration is involved. Furthermore, Fig. 84 shows that an input altitude error of 2 km could lead to nearly 10 km ITL error. This error is costly for designers seeking to obtain sub-kilometer geolocation accuracy.

For the WGS84 constraint, it can be seen in Fig. 83 that despite variable input altitude error, the output altitude error converges to the true transmitter ellipsoid height  $h_u$ , which is 1.39 km for this case. In other words, when the WGS84 surface is used as a constraint, the transmitter height  $h_u$  is assumed to be zero, so the resulting output altitude error will be equivalent to the true  $h_u$ . If the  $h_u$  was 0.5 km, using the WGS84 as a constraint would result in 0.5 km output altitude error. Thus the negative impact of using the WGS84 as a constraint depends on the true transmitter height. In addition, the geolocation error is roughly 5 km as seen in

The DTED0 constraint, was shown to have superior accuracy in all cases tested. As seen in Fig. 83 and Fig. 84, despite input altitude errors of up to 10 km, the output altitude and ITL errors are all tens of meters or less. Thus the usage of the DTED0 constraint in the geolocation simulation is justified. The question might be asked: "what is the computational expense of utilizing the DTED0 constraint?" The application of the DTED0 constraint required iteration, but only 2 or 3 iterations were required. Furthermore, it was observed that for an entire pass of M collects, the altitude iteration only needed to be calculated for the first collect. After the first ITL solution, the altitude estimate  $\hat{r}_e$  stayed nearly constant for the remainder of the pass, reducing computation time required by DTED0 iteration.

# 5.2 Effectiveness of MLE and DTED1 Application

For the second intermediate analysis, the effectiveness of the MLE and DTED1 application methods (Secs. 3.6 and 3.7) was evaluated. Bailey [4] demonstrated the

effectiveness of maximum likelihood estimation in improving CubeSat AOA geolocation estimates, and Schmidt [8] showed how applying digital elevation models could improve AOA and TDOA accuracy. This section contains analysis of the effectiveness of the aforementioned methods for each of the geolocation techniques: AOA, TDOA, and T/FDOA. The questions to be answered in this analysis for each technique are:

- For a pass of M collects, is computing an ML estimate necessary? How much does it improve the raw ITL solutions or the average of ITL solutions for a pass?
- For a pass of M collects, is conducting a DTED1 grid search effective in improving accuracy?

**Methods** A single-scenario geolocation simulation Fig. 13 was executed to obtain the  $\hat{\mathbf{u}}_{mle}$  and  $\hat{\mathbf{u}}_{dted}$  for each algorithm (AOA, TDOA3, etc.) given the system parameters in Table 13. As a reminder, for each algorithm and pass geometry chosen, the ITL solution was calculated ( $\hat{\mathbf{u}}_{itl}$ ), the average ITL was used to initialize the Gauss-Newton algorithm to find  $\hat{\mathbf{u}}_{mle}$ , and  $\hat{\mathbf{u}}_{mle}$  was used as a seed in the DTED1 grid search, to finally obtain  $\hat{\mathbf{u}}_{dted}$ .

This process of obtaining  $\hat{\mathbf{u}}_{dted}$  was executed for each algorithm (AOA, TDOA, etc.) for 500 MC trials. In order to investigate the effectiveness of MLE and DTED1 application the range RMSE was computed for each algorithm as specified in Sec. 3.8. Furthermore, the percent improvement from mean ITL RMSE to MLE RMSE was computed to evaluate MLE effectiveness, and the percent improvement from MLE RMSE to DTED1 RMSE was calculated to evaluate DTED1 effectiveness.

#### 5.2.1 Effectiveness of MLE and DTED1 Grid Search

It is important to note first that the method of obtaining  $\hat{\mathbf{u}}_{mle}$ , the maximum likelihood estimate, is the Gauss-Newton algorithm. This algorithm is completely

Table 13. Parameters for Effectiveness of MLE/DTED1 Test

Parameter	Value	Remarks
Transmitter	2	[15.5°, 100.5°, 26 m]
SV Altitude	500 km	From [10]
Baseline	15 km	Obtained from Fig. 46
Absolute Position	5 m	Assuming on-board GPS receiver
Absolute Velocity	20  cm/s	Assuming on-board GPS receiver
Attitude Determination	0.2°	State of the art for star tracker is is 0.007° [18]
Relative Position	0.5 m	Assuming Differential GPS
Relative Velocity	5  cm/s	Assuming Differential GPS
Angle of Arrival	0.3°	Error in Az and El angle measurements, due to hardware and MUSIC algorithm er- ror
Differential Time Offset (DTO)	100 ns	Time difference measurement error, due to hardware and Complex Ambiguity Func- tion (CAF) accuracy
Differential Freq. Offset (DFO)	10 Hz	Frequency difference measurement error, due to hardware and CAF accuracy

separate from the ITL algorithms previously discussed. The difference is that the Gauss-Newton algorithm requires an initial guess and measurements, while ITL algorithms do not require an initial guess. And finally, the Gauss-Newton algorithm is not influenced by system parameters like Number of Collects or Pass Geometry in the same way the ITL algorithms are. Thus the conclusions from Chapter 4 should not be directly applied to the MLE and DTED1 processes.

The RMSE of the ITL, mean ITL, MLE, and DTED1 geolocation solutions can be observed in Table 14. In Table 15, the percent improvement is shown for each of the algorithms.

Effectiveness of MLE It is apparent from Tabs. 14 and 15 that MLE improves accuracy significantly for TDOA3, TDOA4, TFDOA3 and TFDOA4. MLE

Table 14. Geolocation accuracy with the application of MLE and a DTED1 grid search

#### RMSE (km) Algorithm Estimate Type Pass 1 Pass 2 Pass 3 Pass 4 Pass 5 ITL4.245.20 6.883.32 3.56 AOA MLE 1.78 2.643.524.966.73DTED1 0.671.99 2.954.346.08 ITL99.37 124.81 140.58104.66 103.09 Mean ITL 18.30 19.42 18.49 22.1929.92TDOA3 MLE 1.07 1.29 1.63 2.273.19 2.21DTED1 0.640.851.10 1.49 $\operatorname{ITL}$ 1329.58 955.73 919.42972.12 1134.30 Mean ITL 391.66253.35339.96548.21825.85TDOA4 MLE 179.39 59.4231.9763.0673.97DTED1 49.3124.9163.0573.96179.38 ITL270.75772.58481.65372.091060.00 Mean ITL 114.7787.77 51.871024.85748.03TFDOA2 MLE117.9017.3521.841027.58755.51DTED1 751.62111.15 2.06 2.12 1026.99 ITL396.56395.69136.3999.62101.35Mean ITL 68.4080.88 26.3119.77 21.18TFDOA3 MLE 1.06 1.28 1.63 2.26 3.18 DTED1 2.21 0.640.861.10 1.48 ITL329.41315.50111.7187.81 76.04Mean ITL 56.4956.8024.0017.3017.54TFDOA4 MLE 0.800.971.22 1.72 2.42

0.51

0.68

0.86

1.16

1.66

DTED1

Table 15. Percent improvement of geolocation accuracy due to MLE and DTED1 application

Percent 1	Improvement	(%)
-----------	-------------	-----

Algorithm	Estimate Type	Pass 1	Pass 2	Pass 3	Pass 4	Pass 5
AOA	MLE	46.6	25.7	17.0	4.4	2.2
	DTED1	62.5	24.8	16.3	12.6	9.6
TDOA3	MLE	94.2	93.4	91.2	89.8	89.3
	DTED1	39.9	33.6	32.6	34.3	30.6
TDOA4	MLE	84.8	87.4	81.5	86.5	78.3
	DTED1	17.0	22.1	0.01	0.01	0.005
TFDOA2	MLE	-2.7	80.2	57.9	-0.3	-1.0
	DTED1	5.7	88.1	90.3	0.1	0.5
TFDOA3	MLE	98.5	98.4	93.8	88.6	85.0
	DTED1	39.7	33.1	32.5	34.5	30.6
TFDOA4	MLE	98.6	98.3	94.9	90.1	86.2
	DTED1	36.0	30.4	29.7	32.8	31.3

improved the mean ITL estimates by more than 78% for TDOA3, TDOA4, TFDOA3 and TFDOA4. This astounding improvement justifies the usage of MLE in this simulation.

AOA was also found to improve with MLE, but not as significantly as the other algorithms. It improved as much as 46.6% in Pass 1 but as little as 2.2% in Pass 5. The magnitude of MLE improvement from the LS intersection estimate obtained in AOA ITL is consistent with the results of Bailey [4] for a 500 km altitude CubeSat.

While MLE proved to be effective for the previously mentioned algorithms, the ML estimate for TFDOA2 was nominally better than the non-weighted ITL average, as seen in Tabs. 14 and 15. The MLE inaccuracy was not due to divergence of the Gauss-Newton algorithm, since diverged estimates were discarded. The Gauss-Newton algorithm converged on estimates far from the transmitter in the presence of measurement noise. It is hypothesized that the ambiguity of the dual-satellite

TDOA/FDOA localization circle and the fact that the MLE is unconstrained by the Earth's surface leads to convergence on erroneous transmitter locations. This could be investigated in future work or an alternate method could be implemented for TFDOA2.

Another trend seen in the ML estimates was that the percent improvement of MLE was greatest for Pass 1 and least for Pass 5. This trend is visible for AOA, TDOA3, TFDOA3, and TFDOA4. Similarly, as seen in Table 14, the ML estimate accuracy is greater for the overhead pass and decreases as passes become near to the horizon. It's important to note that the effect of pass type on MLE accuracy is not necessarily identical to the effect of pass type on ITL accuracy, which was explored in Sec. 4.3.

Effectiveness of DTED1 Grid Search It is also seen from Tabs. 14 and 15 that the DTED grid search improved the geolocation accuracy in all cases, however the improvement for the TDOA4 and TFDOA2 algorithms was very minimal in some instances.

For TDOA3, TFDOA3, and TFDOA4, the DTED1 grid search improved estimates between 30-40%. The DTED1 constraint also proved to be effective for AOA, although the effectiveness was highly dependent on the pass type. At the horizon, the grid search only improved the accuracy 9.6%, but when the pass was overhead the grid search improved accuracy by 62.5%.

TDOA4 and TFDOA2 did not benefit from the DTED1 constraint in some cases. It can be observed that for both TDOA4 and TFDOA2, the passes that experienced greatest DTED1 grid search improvement in Table 15 were the passes with smallest MLE error in Table 14. For this case the DTED1 grid search is helpful when the MLE, which is used as the grid search center point, is accurate to within about 50 km. In reality, if the geolocation estimate is more than 50 km off, the effect of transmitter

altitude error is relatively minuscule.

Solutions obtained by DTED1 grid search are also different than the ones obtained by MLE because they lie approximately on the Earth's surface, which can reduce ambiguity for a transmitter known to be terrestrial. The performance of the DTED1 constraint could change when the measurement error or SV navigation error is changed. However overall, the DTED1 grid search implemented in this research was shown to be effective in reducing geolocation error. Future refinement of the grid search algorithm and/or application of a higher resolution DEM could lead to even greater accuracy.

# 5.2.2 Computation Time

While the application of MLE and DTED1 was shown to improve the geolocation accuracy, the question could be asked: "what is the computational trade off?" The average computation time for the Gauss-Newton algorithm, which was used to obtain  $\hat{\mathbf{u}}_{mle}$ , and the DTED1 grid search used to obtain  $\hat{\mathbf{u}}_{dted}$ , are seen in Table 16 for each geolocation technique (AOA, TDOA3, etc.). The times in Table 16 are for an entire pass of M collects. Overall, the time to compute  $\hat{\mathbf{u}}_{mle}$  and  $\hat{\mathbf{u}}_{dted}$  is less than 2 seconds total.

#### 5.3 Performance Analysis

The final analysis included in this research is the evaluation of the overall accuracy of a 1-4 CubeSat geolocation system implementing the methods discussed in Chapter 3. All 6 geolocation techniques (AOA, TDOA3, etc.) are evaluated for the appropriate number of SVs. The objectives are 1) to determine the achievable geolocation accuracy given a nominal scenario and 2) to investigate the measurement error allowable to obtain sub-kilometer accuracy.

Table 16. Computation time for MLE and DTED1 grid search

Geolocation	Gauss-Newton	DTED1 Grid	
Technique	Algorithm (s)	Search (s)	
AOA	3.15e-3	1.15	
TDOA3	1.40e-3	0.96	
TDOA4	2.30e-3	0.86	
TFDOA2	2.70e-3	1.64	
TFDOA3	2.50e-3	0.97	
TFDOA4	3.00e-3	0.90	

Note: Tx 1, average time for 5 pass types, 500 trials

Methods The AOA, TDOA, and FDOA error allowed for a 1-4 CubeSat geolocation cluster in a 500km, 64° inclination orbit was investigated. All system parameters were fixed except the AOA, TDOA, and FDOA error, as shown in Table 17. The AOA error includes error due to azimuth/elevation measurement and SV attitude knowledge error (Eq. 3.16). TDOA error includes both differential time offset (DTO) and timing synchronization error (Eq. 3.17). FDOA error includes DFO and all other frequency knowledge errors (Eq. 3.18). Therefore, as an example, if angle measurement accuracy is poor the system designer can compensate with accurate attitude determination.

The navigation errors were chosen based on the state of the art [18] and the CanX mission [29], which are discussed in Sec. 2.1. These navigation errors remained fixed for this analysis. Furthermore, the relative SV geometry and baseline distance remained constant.

The transmitter type utilized for this analysis was a fixed-site, isotropic transmitter seen in Fig. 15. For each pass, collects were arbitrarily simulated every 24 seconds, so that Pass 1 obtained 30 collects. Thus the line of sight was the only

constraint and the effect of transmitter beam width on geolocation accuracy could be removed. A radar with properties detailed in Fig. 16 was also simulated to observe how the results changed for a sweeping, finite beam width transmitter.

Table 17. Performance Analysis Parameters

Parameter	Value	Remarks
Transmitter	1	[0.5°, 100.5°, 104 m]
SV Altitude	500 km	From [10]
Baseline	15 km	Obtained from Fig. 46
Absolute Position	5 m	Assuming on-board GPS receiver
Absolute Velocity	20  cm/s	Assuming on-board GPS receiver
Relative Position	0.5 m	Assuming Differential GPS
Relative Velocity	5  cm/s	Assuming Differential GPS
AOA Error	[0.03°,0.3°]	Includes Az/El measurement and SV attitude knowledge errors
TDOA Error	[40, 150] ns	Includes DTO measurement and timing synchronization errors
FDOA Error	[10, 250] Hz	Includes DFO measurement and other frequency errors

A geolocation simulation Fig. 13 was executed for each technique. The geolocation RMSE after the DTED1 grid search was calculated for at least 500 trials and plotted as a function of the measurement error. It is recommended for future work to run more trials to obtain more statistically stable results.

# 5.3.1 AOA Error Allowed

The effect of angle of arrival error on the geolocation estimate when DTED1 surface is applied is seen in Fig. 85. For overhead passes the SV can have up to 0.3° angle measurement and attitude knowledge error and still achieve accuracy of less than 500 m RMSE. Passes close to the horizon are more demanding on AOA measurement accuracy. Less than 0.05° AOA error is required to achieve sub-kilometer accuracy using the method in this research. The system designer must decide whether

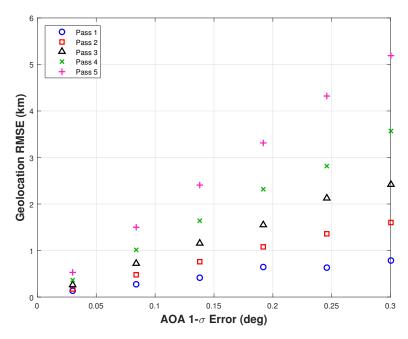


Figure 85. Effect of AOA measurement error on AOA geolocation accuracy with application of DTED1 Earth constraint (2000 trials)

obtaining accurate estimates for near-horizon passes is worth the cost of increasing the AOA measurement and attitude determination accuracy requirements.

#### 5.3.2 TDOA Error Allowed

The effect of the TDOA error on geolocation estimates with the application of a DTED surface constraint is seen in Figs. 86 - 89. For the T/FDOA algorithms the FDOA error was held constant throughout the analyses. The FDOA error was set to 10 Hz. Note that for generality the FDOA error is nondimensionalized by the signal carrier frequency, which is 1.315 GHz. For TDOA3, the geolocation error increases with TDOA error, as expected. It is seen from Fig. 86 that less than 50 ns error is required to achieve sub-kilometer accuracy for all pass types. Greater TDOA error is tolerable to achieve sub-kilometer accuracy for overhead passes, but it is less likely that for an unknown transmitter only overhead passes will occur.

The TDOA4 geolocation error as a function of TDOA error is seen in Fig. 87.

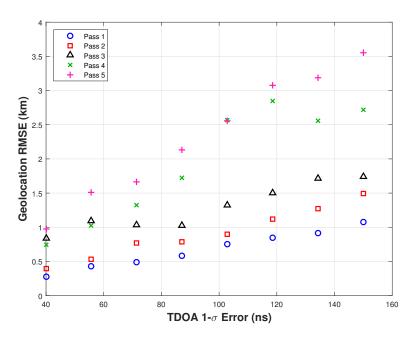


Figure 86. Effect of TDOA measurement error on TDOA3 geolocation accuracy with application of DTED1 Earth constraint (500 trials)

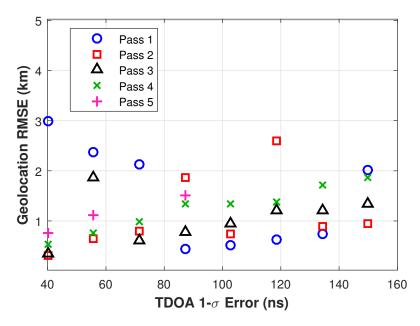


Figure 87. Effect of TDOA measurement error on TDOA4 geolocation accuracy with application of DTED1 Earth constraint (500 trials, Passes 1-4)

The data trend is more sporadic than in Fig. 86 for a few possible reasons. As observed in Table 14, because the TDOA4 algorithm had large errors after the ITL and MLE processes, the DTED1 grid search was ineffective. Because the TDOA4 algorithm was found to be most sensitive to noise for this scenario, a few outliers caused the RMSE to have more unpredictable behavior. Note that some of the Pass 5 data points are omitted in Fig. 87 because of their relatively large magnitude. A complete graph with these points included is in App. B (Fig. 120). Despite the inconsistency of the results, it can be generalized that less than 2 km accuracy is possible for a 4-SV system implementing this TDOA4 algorithm for some pass types and low measurement noise. Figures 88 and 89 demonstrate that for TFDOA3

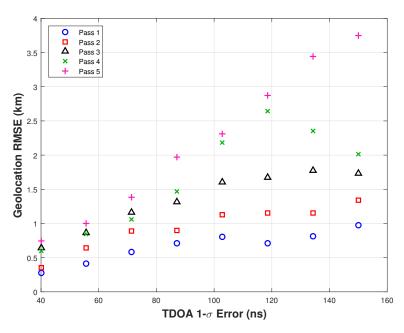


Figure 88. Effect of TDOA measurement error on TFDOA3 geolocation accuracy with application of DTED1 Earth constraint (500 trials,  $\sigma_f = 10Hz$ )

and TFDOA4, when there is a constant 10 Hz FDOA error, less than 50 ns TDOA error is allowed to obtain sub-kilometer accuracy for all pass types. Note that the TFDOA3 performance in Fig. 88 is similar to TDOA3 performance seen in Fig. 86 for these conditions. Future analysis could investigate how TFDOA3 accuracy compares

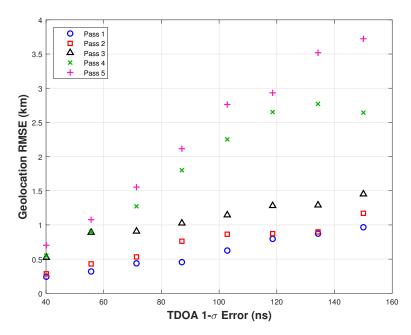


Figure 89. Effect of TDOA measurement error on TFDOA4 geolocation accuracy with application of DTED1 Earth constraint (500 trials,  $\sigma_f = 10Hz$ )

to TDOA3 depending on the FDOA measurement error. It is expected that the TFDOA3 algorithm would have greater accuracy because it incorporates twice the amount of measurements per collect, but the FDOA error and the MLE algorithm influence how much the additional measurements improve the estimate.

#### 5.3.3 FDOA Error Allowed

The effect of FDOA error on geolocation accuracy for the T/FDOA algorithms can be seen in Figs. 90 - 91. Note that the FDOA error  $\sigma_{\dot{\tau}}$  is nondimensionalized by the carrier frequency, and represents the error in range rate difference measured between the  $i^{th}$  and reference SVs. Thus to obtain the FDOA error  $\sigma_f$  required for a particular signal of interest, simply multiply  $\sigma_{\dot{\tau}}$  by the carrier frequency  $f_c$ . Also note that for the duration of this analysis the TDOA error was held constant at 50 ns, so results are limited to this case. It is seen in Fig. 90 that when there is 50 ns TDOA error in the system, less than  $10^{-7}$  of FDOA error (100 Hz for this  $f_c$ ) is required to

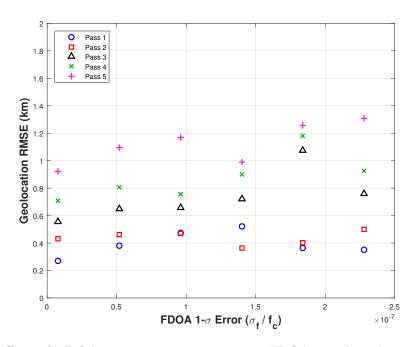


Figure 90. Effect of FDOA measurement error on TFDOA3 geolocation accuracy with application of DTED1 Earth constraint (500 trials)

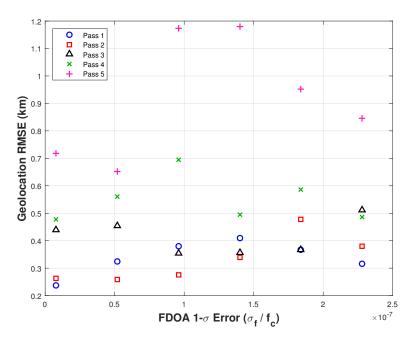


Figure 91. Effect of FDOA measurement error on TFDOA4 geolocation accuracy with application of DTED1 Earth constraint (500 trials)

achieve sub-kilometer accuracy for all pass types. However, greater FDOA error is tolerable if horizon passes are disregarded. Further work could explore what FDOA is allowable for different TDOA errors.

# 5.3.4 Performance Analysis Summary

It is evident from Secs. 5.3.1, 5.3.2, and 5.3.3 that sub-kilometer geolocation accuracy is achievable for the system described in Table 17, but only when there is small measurement error. For AOA geolocation,  $0.05^{\circ}$  AOA error or less is required to be confident sub-kilometer accuracy is obtained for all the pass geometries discussed in this research. For TDOA and T/FDOA systems in this particular scenario, less than 50 ns TDOA and 100 Hz error is desirable for sub-kilometer accuracy. Another trend seen in this section was that overhead passes were generally more accurate than horizon passes. Overhead passes contain more collects for an isotropic transmitter. Furthermore, overhead passes contain signal collects taken from SVs with smaller slant range  $\rho_i$  to the transmitter.

# 5.4 System Design

The previous section analyzed the performance of geolocation systems based on some known parameters. This section explains how one could use the geolocation simulation to develop a system design given some mission requirements. This procedure is not intended to be exhaustive or optimal. However, it is an example of the steps that can be taken to derive SV payload requirements for a hypothetical scenario.

Geolocation Requirement There is a requirement to geolocate a fixed-site radar with the known properties from Table 5 with an accuracy of 2 km.

The first step is to examine Table 4, which contains all the geolocation simulation input parameters. The designer should ask, which parameters are fixed and which

are unknown? What assumptions can be made about each of the parameters? The following paragraphs will discuss each of these parameters and how they might be addressed for an example scenario.

Constraints For this example scenario, it is assumed that the SVs are constrained to a 500 km circular orbit with 64° inclination due to other mission requirements. Secondly, the geologation cluster must consist of no more than 3 SVs.

Transmitter Characterization First note that all of the transmitter parameters are defined by the requirements, with the exception of the radar location and altitude, which are obviously unknown. Thus it is necessary to choose an arbitrary radar location for the purpose of the simulation. A more complex analysis could include multiple radars or radars at varying altitudes or latitudes. For this scenario a radar location of [15.5011°, 100.4989°] will be chosen. Now the true transmitter altitude must be obtained. For this simulation, DTED0 and DTED1 are used throughout for Earth constraints, so it is recommended an altitude based on higher fidelity digital elevation models is used for true altitude. A true altitude of 25.8 m (WGS84 height) obtained from a DTED2 post will be chosen (See Table 6). Ensure that all DTED0, DTED1, and DTED2 files required for the chosen transmitter location are downloaded.

**Orbit Parameters** The orbit parameters in Table 4 that are still undefined are longitude of the ascending node (LAN), argument of latitude, orbit epoch, and baseline distance. Two of many options for generating the first three of these orbit parameters are:

• Propagate the known orbit with arbitrary LAN, argument of latitude, and orbit epoch for several orbital periods in STK (or another propagator of choice), and

analyze a particular pass.

• Manually define 5 (or more) passes with ground tracks similar to the ones in Fig. 15 by shifting the LAN of the orbit.

Method two, "defining 5 passes manually in STK," was chosen for this scenario (Table 7). Next the SV formation must be defined, including the baseline distance between SVs. A good question to ask is: how large of a baseline can be implemented that allows all SVs to still receive the same transmitter signal? If the baseline is too large, all the SVs may not obtain enough collects of the same signal. Employing single-SV AOA geolocation eliminates this problem. For more in depth analysis, the effect of baseline distance on inter-satellite links could be considered to choose the correct baseline for the mission. The SV formation chosen for this example is seen in Sec. 3.2.3.

Once the orbit and transmitter parameters are obtained, the instructions in Sec. 3.3 can be followed to propagate and obtain the SV positions and velocities corresponding to signal collects. Analyses can also be conducted in STK to observe how many signal collects can be expected on average [10].

Algorithms The algorithm was not constrained, however the number of SVs was. Thus multiple algorithms can be simulated: AOA, TDOA3, TFDOA2, and TFDOA3. For further research these algorithms can be fused as well to expand the alternatives (AOA/TFDOA2, AOA/AOA, etc.). The simulation can be run with the multiple algorithms and the results compared to consider the accuracy of the algorithm versus cost of its utilization (AOA payload and # of SVs vs. TDOA3 payload and # of SVs). For this scenario only TFDOA3 will be shown.

System Errors The system errors modeled in the simulation are seen in Table 4. None of these parameters are known based on this scenario's requirements.

For TFDOA3, the applicable system errors can be categorized as navigation errors (absolute and relative positioning) and TDOA or FDOA measurement errors. The goal is to make as many valid assumptions as possible and reduce the number of unknowns. Since there have been recent proximity operations experiments for small satellites in LEO, the absolute and relative positioning achievable can be assumed. A more in depth analysis could include determining the navigation error allowable from plots similar to those in Sec. 4.6.

Since the timing synchronization and DTO measurement errors are modeled as additive Gaussian noise in this simulation, and they both contribute to overall TDOA measurement error as seen in Sec. 3.4.2, they can be treated as general TDOA error. The same can be said for FDOA error. Thus, TDOA and FDOA error are the only remaining variables (with the exception of SV payload parameters). The simulation can be run to determine the geolocation accuracy as a function of the independent variables TDOA and FDOA error.

Measurement Error Allowable Since there are two variables, namely TDOA and FDOA error, one can be fixed at a time with an arbitrary value for simplicity. This exercise is done for the TFDOA3 case only for brevity's sake. Fig. 92 shows the TDOA error allowable based on arbitrary FDOA error of 10 Hz. It is concluded from Fig. 92 that less than 100 ns TDOA error is desirable when FDOA error is 10 Hz. Also as a side note, Pass 3 tends to be most accurate for this radar case. This is a different result than what was seen for the isotropic transmitter (Fig. 88), where Pass 1 was the most accurate.

Then the FDOA error allowable can be determined by holding the TDOA error constant and varying FDOA error. It is shown in Fig. 93 that the FDOA error permitted for the case of 50 ns TDOA error is about  $6 \times 10^{-6}$ . Another iteration of this process would yield more precise TDOA and FDOA requirements, but that

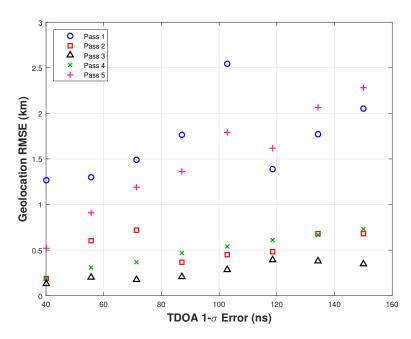


Figure 92. Effect of TDOA measurement error on TFDOA3 geolocation accuracy with application of DTED1 Earth constraint (500 trials,  $\sigma_f = 10Hz$ )

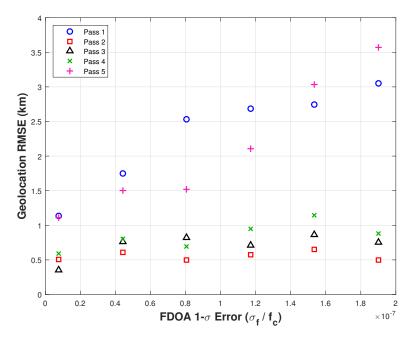


Figure 93. Effect of FDOA measurement error on TFDOA3 geolocation accuracy with application of DTED1 Earth constraint (500 trials,  $\sigma_{\tau} = 50ns$ )

exercise is left for the reader.

SV Payload Requirements Once the required TDOA and FDOA is determined, the designer can determine the payload requirements for measuring the DTO and DFO, via the Complex Ambiguity Function for example (Sec. 2.3.2.3). The CRLBs for the CAF (Eqs. 2.12, 2.13) can be used to determine the integration time T required given a worse case SNR. Then the question could be asked: is the desired T achievable for the chosen payload radio and the transmitter signal characteristics? And for the payload antenna: is the gain pattern and pointing CONOPs sufficient to detect the signal? Additionally, beyond signal detection, will the SNR of the received signal be high enough to obtain the required DTO accuracy according to the CRLB (Eqs. 2.12, 2.13). These same questions can be asked for the AOA payload, pertaining to the number of signal samples N and the type of antenna array, which was covered in Sec. 2.3.1.

**Summary** This section outlined a simple method for utilizing the geolocation simulation to obtain some system level requirements given some mission requirements. While a single design scenario was explored, the tool set can be used for a broad range of geolocation scenarios. The following chapter contains the conclusions of this research effort.

# 6. Conclusions

The goal of this research was to evaluate the performance of a CubeSat in LEO and analyze the sensitivity of AOA, TDOA, and T/FDOA algorithms to system parameters. An STK-MATLAB simulation was developed to determine the geolocation accuracy of a SV cluster utilizing any of the algorithms previously mentioned. A higher fidelity Earth constraint (DTED0) was applied to formerly developed ITL algorithms (TDOA3, T/FDOA). ML estimation was implemented for all 6 geolocation methods. And finally, a Level 1 DTED grid search was utilized for all 6 methods to obtain a more accurate, Earth constrained, geolocation solution.

#### 6.1 Initial Transmitter Localization

The RF geolocation techniques can only be compared and contrasted to an extent, because they have different measurement requirements and are employed from varying numbers of platforms. For example, the AOA and TDOA4 algorithms investigated are not limited to terrestrial transmitters. So if for a nominal scenario the TDOA4 algorithm had poor accuracy and TDOA3 had good accuracy, one could incorrectly draw the conclusion that the TDOA3 algorithm has better performance. The same could be said for the AOA algorithm, since it also does not require a ground constraint. Therefore, any comparisons made apply to the geolocation of terrestrial transmitters only, not the performance of the algorithm in general.

There were many findings from the sensitivity analysis conducted in Chapter 4, the most notable of which will be discussed here. Firstly, it was determined that for all algorithms an increase in slant range from the transmitter to the SVs increased both the measurement error (MUSIC, CAF CRLB) and the effect of the noise on the algorithm itself. Therefore increasing the altitude of the SV orbit has a negative

impact on geolocation accuracy, as expected.

In addition, the geolocation accuracy of different pass types was analyzed. The geolocation performance of the SVs for different pass types is highly dependent on the measurement technique and the transmitter beam pattern. For the CRLB measurement model (MUSIC and CAF) and isotropic transmitter simulated in this research, the AOA and TDOA3 exhibited greater accuracy when passes were overhead the transmitter and were most inaccurate for horizon passes. For the TDOA4 algorithm, Passes 2-4 tended to be more accurate than overhead or horizon passes. And for the measurement model simulated, each of the T/FDOA algorithms exhibited greater accuracy for horizon passes, while overhead passes were the most inaccurate. Depending on the measurement technique utilized, system designers could take advantage of ITL sensitivities to pass geometry by employing two different algorithms, like AOA and TFDOA2 for example, which complement each other's weaknesses, and fusing the measurements and/or estimates.

Overall, the more signal collects obtained by the SVs, the greater ITL accuracy that can be achieved, depending on the method of combining the ITL solutions. A non-weighted average was used to combine the ITL solutions in this research, because that was a sufficient initial guess for ML estimation. However, it was shown that for the ground constrained ITL methods (TDOA3, TFDOA2, TFDOA3, TFDOA4), a greater number of collects did not improve accuracy for all cases when a non-weighted average was utilized, since worse collection geometry leads to worse ITL solutions.

The TDOA4 algorithm from [24] was the most sensitive to system parameter noise. Although it may outperform other ITL methods for transmitter unconstrained by the Earth's surface, for known terrestrial transmitters, it was the most inaccurate in all cases. It is recommended that the TDOA algorithm for S > 3 presented by Ho and Chan in [23], which involves a Newton search much like TFDOA4, be explored for

4-SV ITL using TDOA measurements only in the presence of system errors.

The TFDOA2 algorithm, employed with 2 SVs, generally exhibited more ITL error for the scenarios in Chapter 4 than TDOA3, TFDOA3, and TFDOA4. However, the TFDOA2 algorithm utilizes less measurements than those algorithms. Another disadvantage of TFDOA2 was the solution ambiguity problem. Further work could apply a constrained MLE for the TFDOA2 measurements since the unconstrained MLE was ineffective. Also it is recommended that new formations for dual-satellite TFDOA2 are tested. This research implemented a leader-follower formation, but other formations could yield better geometric diversity which would lead to improved geolocation estimates.

Finally, the negative impact of initial transmitter altitude error on ITL accuracy was reaffirmed for the algorithms that utilize an Earth's surface constraint (TDOA3, T/FDOA). The DTED0 surface implemented into the ITL algorithms was shown to greatly improve ITL solution accuracy, especially when the transmitter was at locations of greater land elevation.

# 6.2 System Level Performance

The ML estimation employed in this research was found to significantly improve upon the ITL solutions for the TDOA3, TDOA4, TFDOA3, and TFDOA4 methods. The DTED1 grid search also successfully enhanced the ML estimates. Both of these methods combined were found to be computationally inexpensive, averaging less than 2 seconds combined to process an entire pass of measurements and obtain a solution.

In addition, the performance analysis conducted in Chapter 5 was found to be useful in determining the geolocation measurement error required to achieve sub-kilometer accuracy. It was determined that 0.05° AOA, 50 ns TDOA, and 100 Hz FDOA error was desirable for the case considered. Results could be improved by

executing more trials. The methods of analyzing system level performance and system design using the geolocation simulation proved to be good starting points for further analyses.

# 6.3 Applicability of Results

Limitations and assumptions had to be made for this analysis. Firstly, a nominal SV formation geometry was chosen for simplicity. Furthermore, it was assumed that each SV utilized a 0 dB receiver with an isotropic beam pattern for signal collection. It was assumed that the signal of interest could be measured, and that the cluster of SVs could identify the same signal being received for each collect.

The type of transmitter, SV payload, signal measurement algorithm, and SV formation are a few factors that could yield better or worse results. For example, a more complex formation, such as the Natural Motion Circumnavigation (NMC) formation discussed in Sec. 2.2, could yield more accurate TDOA and T/FDOA results than seen in this thesis. In addition, SV payload antennas with gain patterns favorable to incoming signals from the horizon could contribute to better accuracy for Pass 5, or in other words, passes occurring close to the horizon as opposed to overhead.

# 6.4 Recommendations for Future Study

There are several areas of this research which could be expanded upon and explored. One major assumption in this research was that the signal of interest could be collected, distinguished, and measured at all of the SVs. In the future, incorporating the MUSIC and CAF algorithm and actual simulation of the signal propagation and measurement could add a degree of fidelity to the geolocation simulation. Secondly, this research assumes a stationary transmitter. However, transmitters of interest

could be stationary or mobile. Further research could be done to investigate the effects of different transmitter types, for example different beam patterns or transmit power, on the satellite collection CONOPs and geologation accuracy.

Decision-level fusion, or the fusion of already determined location estimates, was explored by [8] and shown to be useful for improving geolocation accuracy. The analyses in Chapter 5 could be conducted using fused estimates from multiple algorithms, like AOA and TFDOA2 for example. Fusing estimates could lead to greater accuracy for a wider range of collection geometries, since the different ITL algorithms are affected differently by collection geometry.

It was observed in Chapter 4 that the signal collection geometry highly affects the accuracy of the ITL solution. If the geolocation payload could detect the elevation of arrival of the signal, or somehow determine whether the signal was collected near the horizon or overhead, the ITL solutions could be weighted not only by the measurement error but by the estimated collection geometry.

This research utilized batch estimation to determine the optimal geolocation estimate based off an entire pass of measurements. Sequential methods like a Kalman filter could be explored and compared to the batch method used in this research. Furthermore, the method of implementing maximum likelihood estimation could be improved upon. Using a constrained MLE instead of an unconstrained MLE could improve accuracy and could be more conducive to the TFDOA2 model. Also, while the unconstrained MLE was used for each ITL algorithm (AOA, TFDOA3, etc.) individually to obtain the estimate that minimized the TDOA and FDOA measurement, future work could investigate using angle, time, and frequency measurements combined when determining the estimate that minimizes the measurement error.

And lastly, this tool set could be utilized in a variety of geolocation analyses, including the optimization of mission orbits for the different RF geolocation techniques.

# 6.5 Final Conclusion

This research provides a good overview and structure for analyzing a design problem that has many variables. Eliminating some simplifying assumptions, adding fidelity to the simulation, and focusing the analysis in this research could lead to significant improvements in geolocation performance analysis and system design.

# Appendix A. ITL Methods

This appendix contains the methods of implementing the Initial Transmitter Localization (ITL) algorithms (AOA, TDOA, T/FDOA) used in this research.

# A.1 Angle of Arrival

This section describes in detail the process of obtaining 1 least squares estimate for the location of a transmitter given M azimuth and elevation measurements.

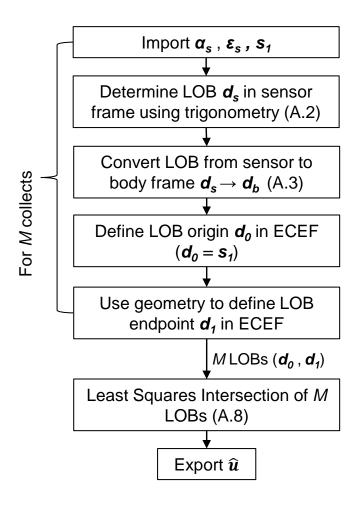


Figure 94. AOA Algorithm Overview

**Inputs** Start with the azimuths and elevations of arrival (Fig. 95) in the sensor frame along with corresponding satellite ECEF positions.

$$\boldsymbol{\alpha}_{s} = \begin{bmatrix} \alpha_{1} \\ \alpha_{2} \\ \dots \\ \alpha_{M} \end{bmatrix}, \boldsymbol{\epsilon}_{s} = \begin{bmatrix} \epsilon_{1} \\ \epsilon_{2} \\ \dots \\ \epsilon_{M} \end{bmatrix}, \mathbf{S}_{1} = \begin{bmatrix} \mathbf{s}_{1,1}^{T} \\ \vdots \\ \mathbf{s}_{1,M}^{T} \end{bmatrix}$$
(A.1)

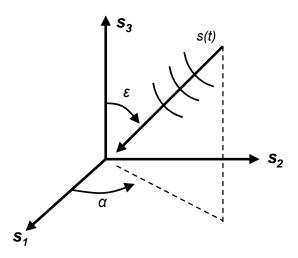


Figure 95. An impinging signal as shown in the sensor frame

Unit vectors representing the signal's direction of arrival are generated using Eq. A.2.

$$\hat{\mathbf{d}} = \begin{bmatrix} \cos \alpha \sin \epsilon \\ \sin \alpha \sin \epsilon \\ \cos \epsilon \end{bmatrix}$$
(A.2)

These lines of bearing must be transformed into the body frame, using a rotation matrix  $\mathbf{R}_{bs}$ .

$$\hat{\mathbf{d}}_b = \mathbf{R}_{bs} \hat{\mathbf{d}}_s \tag{A.3}$$

Modeling sensor frame rotation is outside the scope of this research, so the sensor frame is assumed to be aligned with the body frame ( $\mathbf{R}_{bs} = \mathbf{I}_{3x3}$ ).

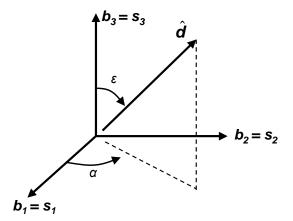


Figure 96. The line of bearing unit vector  $\hat{\mathbf{d}}$  for a single  $\alpha$  and  $\epsilon$ 

Step A:

Once you get stuff in body frame, convert from body to ENU.

$$\epsilon_{ENU} = -\epsilon_b \qquad \epsilon_{ENU} \in [-\pi/2, \pi/2]$$

$$\alpha_{ENU} = alpha_b + \phi_n \qquad \alpha_{ENU} \in [0, 2\pi]$$
(A.4)

The MATLAB commands ecef2geodetic and aer2ecef from the Aerospace Toolbox are used to transform the direction of arrival  $\hat{\mathbf{d}}_b$  into a vector  $\mathbf{d}$  with origin  $\mathbf{d}_0$  at the satellite receiver position and endpoint  $\mathbf{d}_1$  at some arbitrary length long enough to intersect the Earth's surface. Both  $\mathbf{d}_0$  and  $\mathbf{d}_1$  are expressed in ECEF coordinates.

Initial transmitter localization (ITL) can be achieved with a single measurement by intersecting **d** with the Earth's surface. However, in a single pass over the transmitter of interest, the satellite can typically obtain multiple signal measurements, depending on the scenario. For each  $(\alpha_m, \epsilon_m)$  a line of bearing can be generated.

Then least squares intersection can be applied to estimate the transmitter location without utilizing the Earth's surface as a constraint (Sec. 2.4.1). First each LOB with starting point  $\mathbf{d}_0$  and end point  $\mathbf{d}_1$  (ECEF) must be normalized.

$$\hat{\mathbf{d}}_m = \frac{\mathbf{d}_1 - \mathbf{d}_0}{\|\mathbf{d}_1 - \mathbf{d}_0\|} \tag{A.5}$$

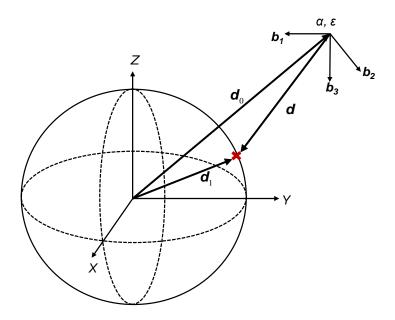


Figure 97. LOB can be represented in ECEF coordinates after being transformed from azimuth, elevation, and range in the body frame

The matrix  $\mathbf{P} = \mathbf{I}_{3x3} - \mathbf{u}\mathbf{u}^T$  will project every vector  $\mathbf{u} \in \mathbb{R}^3$  into the plane orthogonal to  $\mathbf{u}$  which passes through the origin. For each LOB  $\mathbf{d}$  this projection matrix is ([55], [8])

$$\mathbf{P}_m = \mathbf{I}_{3x3} - \hat{\mathbf{d}}_m \hat{\mathbf{d}}_m^T \tag{A.6}$$

In order to find the orthogonal distance  $\delta_m$  between a point **u** and an LOB  $\mathbf{d}_m$ , the LOB endpoint  $\mathbf{d}_{1_m}$  and **u** must both be projected into the orthogonal plane.

$$\delta_m = \|\mathbf{P}_m \mathbf{u} - \mathbf{P}_m \mathbf{d}_{1_m}\| \tag{A.7}$$

The least squares solution is the point  $\mathbf{u}$  which minimizes the sum of the squared distances  $\delta_m$  (Sec. 2.5.2).

$$\hat{\mathbf{u}}_{LS} = \arg\min_{\hat{\mathbf{u}}} \left\{ \sum_{m=1}^{M} \|\mathbf{P}_m \hat{\mathbf{u}} - \mathbf{P}_m \mathbf{d}_{1_m}\|^2 \right\}$$
(A.8)

Define  $\mathbf{A} = \sum_{m=1}^{M} \mathbf{P}_m$  and  $\mathbf{b} = \sum_{m=1}^{M} \mathbf{P}_m \mathbf{d}_{1_m}$ . As mentioned above,  $\mathbf{A}$  maps  $\hat{\mathbf{u}}$  into the orthogonal plane with  $\mathbf{b}$  Eq. A.9.

$$\mathbf{A}\hat{\mathbf{u}} = \mathbf{b} \tag{A.9}$$

As discussed in Sec. 2.5.2, the least squares solution to this overdetermined problem is given as [55]

$$\hat{\mathbf{u}}_{LS} = \left(\mathbf{A}^T \mathbf{A}\right)^{-1} \mathbf{A}^T \mathbf{b} \tag{A.10}$$

#### A.2 Time Difference of Arrival

# A.2.1 TDOA4

This section describes in detail the process of obtaining 1 transmitter location estimate given 3 TDOA measurements taken at approximately the same instant (4 satellites total, 1 reference).

**Inputs** The TDOA measurements and satellite positions are required. The spherical Earth mean radius 6371 km is used as an initial guess by default.

$$\boldsymbol{\tau}_{M\times3} = \begin{bmatrix} \tau_{21} & \tau_{31} & \tau_{41} \\ \vdots & \vdots & \vdots \end{bmatrix}, \mathbf{S}_{i} = \begin{bmatrix} \mathbf{s}_{i,1}^{T} \\ \vdots \\ \mathbf{s}_{i,M}^{T} \end{bmatrix}, i = 1, 2, 3, 4$$
(A.11)

For each m collect, Determine the range differences between receivers 2, 3, 4 and reference receiver 1 using Eq. A.12.

$$r_{i1} = c\tau_{i1} = \rho_i - \rho_1 \qquad i = 2, 3, 4$$

$$\rho_i \equiv \|\boldsymbol{\rho}_i\| = \|\mathbf{s}_i - \mathbf{u}\|$$
(A.12)

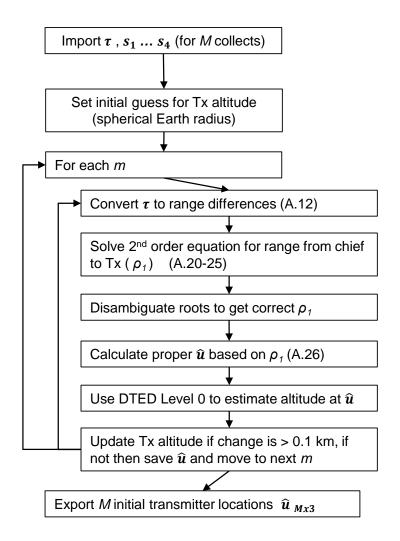


Figure 98. TDOA4 Algorithm Overview

## **Derivation of TDOA Equations** Eq. A.12 to Eq. A.19

Start by expanding  $\rho_i$ .

$$\rho_i = \sqrt{(x_i - x_t)^2 + (y_i - y_t)^2 + (z_i - z_t)^2}$$
(A.13)

Rearrange terms in Eq. A.12, square both sides.

$$\rho_i^2 = r_{i1}^2 + 2r_{i1}\rho_1 + \rho_1^2 \tag{A.14}$$

Rearrange again.

$$r_{i1}^2 + 2\rho_1 r_{i1} = \rho_i^2 - \rho_1^2 \tag{A.15}$$

From Eq. A.13,  $\rho_i^2=(x_i-x_t)^2+(y_i-y_t)^2+(z_i-z_t)^2$  . Expand this definition out:

$$\rho_i^2 = x_i^2 - 2x_i x_t + x_t^2 + y_i^2 - 2y_i y_t + y_t^2 + z_i^2 - 2z_i z_t + z_t^2$$
(A.16)

Substitute Eq. A.16 for the right side of Eq. A.15.

$$\rho_{i}^{2} - \rho_{1}^{2} = x_{i}^{2} - 2x_{i}x_{t} + x_{t}^{2} + y_{i}^{2} - 2y_{i}y_{t} + y_{t}^{2} + z_{i}^{2} - 2z_{i}z_{t} + z_{t}^{2}$$

$$- \left(x_{1}^{2} - 2x_{1}x_{t} + x_{t}^{2} + y_{1}^{2} - 2y_{1}y_{t} + y_{t}^{2} + z_{1}^{2} - 2z_{1}z_{t} + z_{t}^{2}\right)$$

$$= \left(x_{i}^{2} + y_{i}^{2} + z_{i}^{2}\right) - \left(x_{1}^{2} + y_{1}^{2} + z_{1}^{2}\right)$$

$$- 2\left[\left(x_{i} - x_{1}\right)x_{t} + \left(y_{i} - y_{t}\right)y_{t} + \left(z_{i} - z_{1}\right)z_{t}\right]$$
(A.17)

This result plugged into Eq. A.15 gives the general TDOA equation.

$$r_{i1}^{2} + 2\rho_{1}r_{i1} = (x_{i}^{2} + y_{i}^{2} + z_{i}^{2}) - (x_{1}^{2} + y_{1}^{2} + z_{1}^{2})$$

$$- 2[(x_{i} - x_{1})x_{t} + (y_{i} - y_{1})y_{t} + (z_{i} - z_{1})z_{t}]$$

$$= \mathbf{s}_{i}^{T}\mathbf{s}_{i} - \mathbf{s}_{1}^{T}\mathbf{s}_{1} - 2(\mathbf{s}_{i} - \mathbf{s}_{1})^{T}\mathbf{u}$$
(A.18)

The expanded form of Eq. A.3.1 can be written for receivers 2,3, and 4 in matrix form:

$$\begin{bmatrix} r_{21}^2 \\ r_{31}^2 \\ r_{41}^2 \end{bmatrix} + 2\rho_1 \begin{bmatrix} r_{21} \\ r_{31} \\ r_{41} \end{bmatrix} = -2 \begin{bmatrix} x_{21} & y_{21} & z_{21} \\ x_{31} & y_{31} & z_{31} \\ x_{41} & y_{41} & z_{41} \end{bmatrix} \begin{bmatrix} x_t \\ y_t \\ z_t \end{bmatrix} + \begin{bmatrix} K_2 \\ K_3 \\ K_4 \end{bmatrix} - \begin{bmatrix} K_1 \\ K_1 \\ K_1 \end{bmatrix}$$

$$(A.19)$$

$$K_i \equiv x_i^2 + y_i^2 + z_i^2$$

Solving for  $\rho_1$  Kulumani [24] showed how Eq. A.19 can be rewritten solely in terms of  $\rho_1$ , the range from the transmitter to the reference satellite (Eq. A.20). Once Eq. A.20 is solved the unknown transmitter position  $\mathbf{u} = [x_t, y_t, z_t]^T$  can be determined.

$$0 = A\rho_1^2 + B\rho_1 + C \tag{A.20}$$

Where A, B, and C are constants to be derived below. In order to do so, some intermediate constants are defined.

$$\begin{bmatrix} \alpha_1 \\ \alpha_2 \\ \alpha_3 \end{bmatrix} = - \begin{bmatrix} x_{21} & y_{21} & z_{21} \\ x_{31} & y_{31} & z_{31} \\ x_{41} & y_{41} & z_{41} \end{bmatrix}^{-1} \begin{bmatrix} r_{21} \\ r_{31} \\ r_{41} \end{bmatrix}$$
(A.21)

$$\begin{bmatrix} \beta_1 \\ \beta_2 \\ \beta_3 \end{bmatrix} = - \begin{bmatrix} x_{21} & y_{21} & z_{21} \\ x_{31} & y_{31} & z_{31} \\ x_{41} & y_{41} & z_{41} \end{bmatrix} - \begin{bmatrix} r_{21}^2 - K_2 + K_1 \\ \frac{1}{2} & r_{31}^2 - K_3 + K_1 \\ r_{41}^2 - K_4 + K_1 \end{bmatrix}$$
(A.22)

The coefficients can now be written as:

$$A = \alpha_1^2 + \alpha_2^2 + \alpha_3^2 - 1 \tag{A.23}$$

$$B = 2(\alpha_1 \beta_1 + \alpha_2 \beta_2 + \alpha_3 \beta_3 - x_1 \alpha_1 - y_1 \alpha_2 - z_1 \alpha_3)$$
(A.24)

$$C = K_1 - 2x_1\beta_1 - 2y_1\beta_2 - 2z_1\beta_3 + \beta_1^2 + \beta_2^2 + \beta_3^2$$
(A.25)

Now the quadratic equation Eq. A.20 can be simply solved for  $\rho_1$  (e.g. using MAT-LAB function roots).

Root Disambiguation In addition to TDOA4, other methods like TDOA3, TFDOA2, TFDOA3, and TFDOA4 each require solving polynomial equations and disambiguating roots. The general process used in this research for root disambiguation is shown in Fig. 99. The main method used is to remove negative roots and

# Process (TDOA3, TDOA4, TFDOA2, TFDOA34) Remove negative roots For TDOA3 and TDOA4, pick positive complex conjugate (if present) Solve for $\hat{u}$ for each remaining $\rho_1$ Calculate range from $\hat{u}$ to $\mathbf{s}_1$ Calculate max and min $\rho_1$ based on line of sight (coverage constraint) Remove roots don't satisfy coverage constraint If still ambiguous, cheat Choose $\hat{u}$ closest to true u

Figure 99. Root Disambiguation Process

apply the line of sight constraint, as recommended by Guo [3]. The disambiguation method is not the most computationally efficient, but it was designed to be interchangeable between multiple algorithms. Furthermore, a cheat step was added so

that in the presence of large measurement noise failed disambiguation would not detract from the analysis, which is the main focus of this research. Kulumani [24] and Ho [23] suggest using original measurement equations to choose the correct roots.

The second order equation Eq. A.23 will have 2 roots. Typically only one root is positive and within the line of sight constraint. In the presence of measurement or receiver knowledge error it is possible to obtain complex conjugates or in some cases two real negative roots. In many cases the positive complex conjugate can be plugged into Eq. A.26 to get a valid yet inaccurate solution. If there are no valid roots those measurements are thrown out and the next set are used to obtain an ITL solution.

After disambiguation, the unknown  $\mathbf{u}$  can be solved by rearranging Eq. A.19.

$$\hat{\mathbf{u}} = -\begin{bmatrix} x_{21} & y_{21} & z_{21} \\ x_{31} & y_{31} & z_{31} \\ x_{41} & y_{41} & z_{41} \end{bmatrix}^{-1} \left\{ \rho_1 \begin{bmatrix} r_{21} \\ r_{31} \\ r_{41} \end{bmatrix} + \frac{1}{2} \begin{bmatrix} r_{21}^2 - K_2 + K_1 \\ r_{31}^2 - K_3 + K_1 \\ r_{41}^2 - K_4 + K_1 \end{bmatrix} \right\}$$
(A.26)

### A.2.2 TDOA3

This section describes in detail the process of obtaining 1 transmitter location estimate given 2 TDOA measurements taken at approximately the same instant (3 satellites total, 1 reference). This algorithm uses the Earth's surface as an additional constraint, assuming the transmitter has zero altitude. To combat error imposed by unknown altitude and variation in  $r_e$ , an iteration method similar to the one in [3] is utilized. The  $r_e$  based off a spherical Earth is used as the initial guess, and each time a new  $\mathbf{u}$  is calculated,  $r_e$  is updated based off of level 0 digital terrian elevation data (App. B).

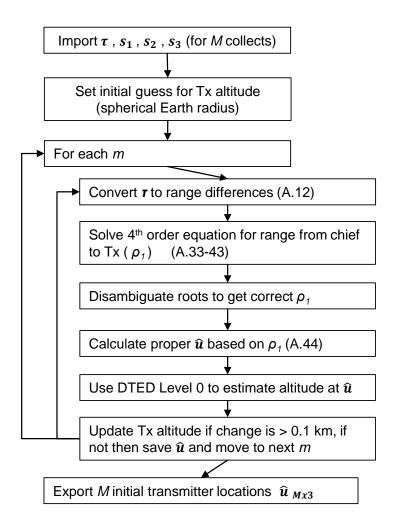


Figure 100. TDOA3 Algorithm Overview

**Inputs** The TDOA measurements and satellite positions are required. The spherical Earth mean radius 6371 km is used as an initial guess by default.

$$\boldsymbol{\tau}_{M\times2} = \begin{bmatrix} \tau_{21} & \tau_{31} \\ \vdots & \vdots \end{bmatrix}, \mathbf{S}_i = \begin{bmatrix} \mathbf{s}_{i,1}^T \\ \vdots \\ \mathbf{s}_{i,M}^T \end{bmatrix}, i = 1, 2, 3$$
(A.27)

For each m collect, Determine the range differences between receivers 2, 3 and reference receiver 1 using Eq. A.12.

### **Derivation of TDOA Equations** Eq. A.12 to Eq. A.32

First group the terms from Eq. A.16 in order to get

$$\rho_i^2 = (x_i^2 + y_i^2 + z_i^2) - 2(x_i x_t + y_i y_t + z_i z_t) + (x_t^2 + y_t^2 + z_t^2)$$
(A.28)

Using the definition of  $K_i$  and assumption  $\mathbf{u}^T\mathbf{u} = x_t^2 + y_t^2 + z_t^2 = r_e^2$ ,

$$\rho_i^2 = K_i - 2(x_i x_t + y_i y_t + z_i z_t) + r_e^2 \tag{A.29}$$

Rearranging gives

$$2x_i x_t + 2y_i y_t + 2z_i z_t = K_i + r_e^2 - \rho_i^2$$

$$2\mathbf{s}_i^T \mathbf{u} = \mathbf{s}_i^T \mathbf{s}_i + r_e^2 - \rho_i^2$$
(A.30)

Eq. A.30 serves as the Earth's surface constraint equation. The equations for satellites 2 and 3 can be obtained by plugging Eq. A.14 into Eq. A.30. The general form is

$$2x_i x_t + 2y_i y_t + 2z_i z_t = K_i + r_e^2 - (r_{i1}^2 + 2r_{i1}\rho_1 + \rho_1^2)$$
(A.31)

Equations 2 and 3 can be added to the first constraint and put in matrix form:

$$\begin{bmatrix} x_1 & y_1 & z_1 \\ x_2 & y_2 & z_2 \\ x_3 & y_3 & z_3 \end{bmatrix} \begin{bmatrix} x_t \\ y_t \\ z_t \end{bmatrix} = \frac{1}{2} \begin{bmatrix} K_1 + r_e^2 - \rho_i^2 \\ K_2 + r_e^2 - \rho_i^2 - 2r_{21}\rho_1 - r_{21}^2 \\ K_3 + r_e^2 - \rho_i^2 - 2r_{31}\rho_1 - r_{31}^2 \end{bmatrix}$$
(A.32)

Solving for  $\rho_1$  Kulumani [24] demonstrated how Eq. A.32 can be expressed solely in terms of  $\rho_1$ , this time in a quartic equation.

$$\tilde{A}\rho_1^4 + \tilde{B}\rho_1^3 + \tilde{C}\rho_1^2 + \tilde{D}\rho_1 + \tilde{E} = 0 \tag{A.33}$$

In order to obtain the unknown coefficients  $\tilde{A}-\tilde{E}$  intermediate parameters must be defined.

$$\begin{bmatrix} \alpha \\ \beta \\ \varphi \end{bmatrix} = \begin{bmatrix} K_1 + r_e^2 \\ K_2 + r_e^2 - r_{21}^2 \\ K_3 + r_e^2 - r_{31}^2 \end{bmatrix}$$
 (A.34)

$$\begin{bmatrix} a_{11} & a_{12} & a_{13} \\ a_{21} & a_{22} & a_{23} \\ a_{31} & a_{32} & a_{33} \end{bmatrix} = \frac{1}{2} \begin{bmatrix} x_1 & y_1 & z_1 \\ x_2 & y_2 & z_2 \\ x_3 & y_3 & z_3 \end{bmatrix}^{-1}$$
(A.35)

$$\begin{bmatrix} A \\ D \\ G \end{bmatrix} = \begin{bmatrix} a_{11} & a_{12} & a_{13} \\ a_{21} & a_{22} & a_{23} \\ a_{31} & a_{32} & a_{33} \end{bmatrix} \begin{bmatrix} -1 \\ -1 \\ -1 \end{bmatrix}$$
(A.36)

$$\begin{bmatrix} B \\ E \\ H \end{bmatrix} = \begin{bmatrix} a_{12} & a_{13} \\ a_{22} & a_{23} \\ a_{32} & a_{33} \end{bmatrix} \begin{bmatrix} -2r_{21} \\ -2r_{31} \end{bmatrix}$$
(A.37)

$$\begin{bmatrix} C \\ F \\ I \end{bmatrix} = \begin{bmatrix} a_{11} & a_{12} & a_{13} \\ a_{21} & a_{22} & a_{23} \\ a_{31} & a_{32} & a_{33} \end{bmatrix} \begin{bmatrix} \alpha \\ \beta \\ \varphi \end{bmatrix}$$
(A.38)

Once the intermediate parameters have been defined the unknown coefficients can be calculated as shown below.

$$\tilde{A} = A^2 + D^2 + G^2 \tag{A.39}$$

$$\tilde{B} = 2AB + 2DE + 2GH \tag{A.40}$$

$$\tilde{C} = -2x_1A - 2y_1D - 2z_1G + 2AC + 2DF + 2GI + B^2 + E^2 + H^2 - 1$$
 (A.41)

$$\tilde{D} = -2x_1B - 2y_1E - 2z_1H + 2BC + 2EF + 2HI \tag{A.42}$$

$$\tilde{E} = -2x_1C - 2y_1F - 2z_1I + C^2 + F^2 + I^2 + K_1 \tag{A.43}$$

Now the quartic equation Eq. A.33 can be simply solved for  $\rho_1$  (e.g. using MATLAB function roots).

Root Disambiguation Four roots are produced from the quartic equation Eq. A.33. The process for root disambiguation is seen in Fig. 99. There will only be 2 positive roots [3]. There will either be two real roots, one of which is valid, or two complex conjugates. Sometimes in the presence of large measurement noise both real roots satisfy line of sight or a complex conjugate does not meet the constraints at all.

After disambiguation, the unknown **u** can be solved by rearranging Eq. A.32 and using the previously found  $\rho_1$ .

$$\hat{\mathbf{u}} = \frac{1}{2} \begin{bmatrix} x_1 & y_1 & z_1 \\ x_2 & y_2 & z_2 \\ x_3 & y_3 & z_3 \end{bmatrix}^{-1} \begin{bmatrix} K_1 + r_e^2 - \rho_1^2 \\ K_2 + r_e^2 - \rho_1^2 - 2r_{21}\rho_1 - r_{21}^2 \\ K_3 + r_e^2 - \rho_1^2 - 2r_{31}\rho_1 - r_{31}^2 \end{bmatrix}$$
(A.44)

Iteration for Proper Altitude Once  $\hat{\mathbf{u}}$  is solved for, the geodetic latitude and longitude are determined using ecef2geodetic. These coordinates are used to obtain the altitude based on 30 arcsecond terrain data (Level 0, App. B). This data has already been converted into WGS 84 ellispoid height h. This h becomes the new  $r_e$ . The maximum number of iterations is small to decrease computational burden. In addition, the tolerance is set to reduce sensitivity to steep altitude gradients.

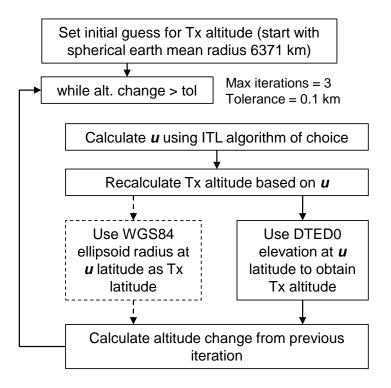


Figure 101. Altitude Iteration Process

### A.3 Time and Frequency Difference of Arrival

### A.3.1 TFDOA2

This section describes in detail the process of obtaining 1 transmitter location estimate given 1 TDOA and 1 FDOA measurement taken at approximately the same instant (between 2 satellites). This algorithm uses the Earth's surface as an additional

constraint, assuming transmitter has zero altitude. The  $r_e$  iteration method discussed in Sec. A.2.2 is used to treat altitude knowledge error. Note that since  $\rho_1$  is used so frequently throughout the next two sections, it is also referred to as  $\rho_1$ .

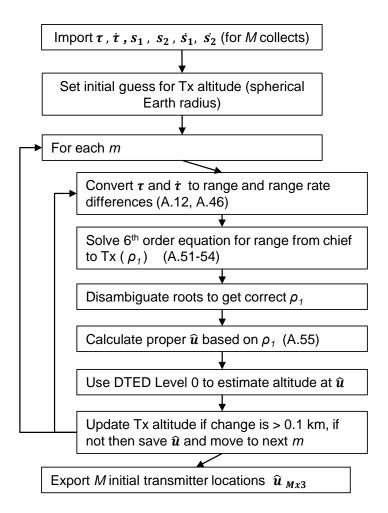


Figure 102. TFDOA2 Algorithm Overview

**Inputs** The TDOA and FDOA measurements, positions, and velocities are required. The spherical Earth mean radius 6371 km is used as an initial guess by

default.

$$\boldsymbol{\tau}_{M\times 1} = \begin{bmatrix} \tau_{21} \\ \vdots \end{bmatrix}, \dot{\boldsymbol{\tau}}_{M\times 1} = \begin{bmatrix} \dot{\tau}_{21} \\ \vdots \end{bmatrix}, \mathbf{S}_{i} = \begin{bmatrix} \mathbf{s}_{i,1}^{T} \\ \vdots \\ \mathbf{s}_{i,M}^{T} \end{bmatrix}, \dot{\mathbf{S}}_{i} = \begin{bmatrix} \dot{\mathbf{s}}_{i,1}^{T} \\ \vdots \\ \dot{\mathbf{s}}_{i,M}^{T} \end{bmatrix}, i = 1, 2$$
(A.45)

For each time measurement  $\tau$ , determine the range difference  $r_{i1}$  between satellites 1 and 2 using Eq. A.12. Then for each frequency measurement  $\dot{\tau}$  determine the range rate difference using Eq. A.46.

$$\dot{r}_{i1} = c\dot{\tau}_{i1} = \dot{\rho}_i - \dot{\rho}_1 \qquad i = 2, 3, 4$$
 (A.46)

**TDOA and FDOA Equations** Recall the TDOA equation for the  $i^{th}$  receiver from Sec. A.2.1. This equation relates the measured  $\rho_i$  to the transmitter location **u**. Rearrange terms to obtain Eq. A.47.

$$r_{i1}^2 + 2\rho_1 r_{i1} - \mathbf{s}_i^T \mathbf{s}_i + \mathbf{s}_1^T \mathbf{s}_1 = -2(\mathbf{s}_i - \mathbf{s}_1)^T \mathbf{u}$$
  $i = 2, 3, ..., S$  (A.47)

Then an equation utilizing the TDOA, FDOA, and transmitter location can be formed by taking the derivative of Eq. A.47.

$$2r_{i1}\dot{r}_{i1} + 2r_{i1}\dot{\rho}_1 + 2\dot{r}_{i1}\rho_1 - 2\mathbf{s}_i^T\dot{\mathbf{s}}_i + 2\mathbf{s}_1^T\dot{\mathbf{s}}_1 = -2(\dot{\mathbf{s}}_i - \dot{\mathbf{s}}_1)^T\mathbf{u} \qquad i = 2, 3, ..., S \quad (A.48)$$

Equations Eq. A.47 and Eq. A.48 each have three unknowns,  $\mathbf{u} = [x_t, y_t, z_t]^T$ . Therefore if S = 2 (two satellite receivers), there will be one TDOA equation and one T/FDOA equation, and an additional constraint is required to obtain a solution. In this case the Earth's surface constraint can be used. Rearranging Eq. A.30 the third

T/FDOA equation becomes

$$\rho_i^2 = r_e^2 + \mathbf{s}_i^T \mathbf{s}_i - 2\mathbf{s}_i^T \mathbf{u} \qquad i = 2, 3, ..., S$$
(A.49)

Ho and Chan combine Eq. A.47 and Eq. A.48 for i = 2, and Eq. A.49 for i = 1 to generate the matrix equation

$$\mathbf{u} = \mathbf{G}_{1}^{-1}\mathbf{h} = \mathbf{G}_{4}\bar{\rho}_{a} + \mathbf{g}_{5}\dot{\rho}_{1}$$

$$\mathbf{G}_{1} \equiv -2\begin{bmatrix} \mathbf{s}_{1}^{T} \\ \mathbf{s}_{2}^{T} - \mathbf{s}_{1}^{T} \\ \dot{\mathbf{s}}_{2}^{T} - \dot{\mathbf{s}}_{1}^{T} \end{bmatrix}$$

$$\dot{\mathbf{h}} \equiv \mathbf{G}_{2}\bar{\rho}_{a} + \mathbf{g}_{3}\dot{\rho}_{1} = \begin{bmatrix} -r_{e}^{2} - \mathbf{s}_{1}^{T}\mathbf{s}_{1} & 0 & 1 \\ r_{21}^{2} - \mathbf{s}_{2}^{T}\mathbf{s}_{2} + \mathbf{s}_{1}^{T}\mathbf{s}_{1} & 2r_{21} & 0 \\ 2r_{21}\dot{r}_{21} - 2\mathbf{s}_{2}^{T}\dot{\mathbf{s}}_{2} + 2\mathbf{s}_{1}^{T}\dot{\mathbf{s}}_{1} & 2\dot{r}_{21} & 0 \end{bmatrix} \begin{bmatrix} 1 \\ \rho_{1} \\ \rho_{2}^{2} \end{bmatrix} + \begin{bmatrix} 0 \\ 0 \\ 2r_{21} \end{bmatrix}$$

$$\mathbf{G}_{4} \equiv \mathbf{G}_{1}^{-1}\mathbf{G}_{2} \quad \mathbf{g}_{5} \equiv \mathbf{G}_{1}^{-1}\mathbf{g}_{3} \quad \bar{\rho}_{a} \equiv \begin{bmatrix} 1 & \rho_{1} & \rho_{1}^{2} \end{bmatrix}^{T}$$

$$(A.50)$$

 $G_1$  must be invertible in order to obtain a solution for  $\mathbf{u}$ . Ho [23] states that  $G_1$  is not invertible when 1)  $\mathbf{s}_1$ ,  $\mathbf{s}_2$  and the Earth's center all lie on a straight line or 2)  $(\dot{\mathbf{s}}_2 - \dot{\mathbf{s}}_1)$ , the relative velocity between SV 1 and SV 2, is in the direction of  $(\mathbf{s}_2 - \mathbf{s}_1)$  or  $\mathbf{s}_1$ . The goal is to obtain  $\rho_1$  in order to solve Eq. A.50 for the unknown transmitter  $\mathbf{u}$ . The algebraic derivations Ho and Chan use to obtain an equation for  $\rho_1$  are detailed in [3] and [23]. This section will only document the steps taken to solve for  $\rho_1$ .

Solving for  $\rho_1$  First calculate  $G_1$ ,  $g_3$ ,  $G_2$ ,  $G_4$ , and  $g_6$  as defined in Eq. A.50. For the case without measurement or receiver knowledge error, Eq. A.51 should be satisfied.

$$\mathbf{u} = \mathbf{G}_1^{-1} (\mathbf{G}_2 \bar{\boldsymbol{\rho}}_a + \mathbf{g}_3 \dot{\boldsymbol{\rho}}_1) \tag{A.51}$$

Determine new constants  $\mathbf{g}_6$  and p. Verify Eq. A.52 is satisfied.

$$\dot{\rho}_{1} = \frac{1}{\rho_{1} + p} \mathbf{g}_{6}^{T} \bar{\boldsymbol{\rho}}_{a}$$

$$p \equiv \dot{\mathbf{s}}_{1}^{T} \mathbf{g}_{5} \qquad \mathbf{g}_{6} \equiv \begin{bmatrix} \mathbf{s}_{1}^{T} \dot{\mathbf{s}}_{1} & 0 & 0 \end{bmatrix}^{T} - \mathbf{G}_{4}^{T} \dot{\mathbf{s}}_{1}$$
(A.52)

Now define the constant  $G_7$ . Eq. A.53 can be used for verification.

$$\mathbf{u} = \frac{\mathbf{G}_7 \bar{\boldsymbol{\rho}}_b}{\rho_1 + p}$$

$$\mathbf{G}_7 \equiv \begin{bmatrix} p\mathbf{G}_4 + \mathbf{g}_5 \mathbf{g}_6^T & \mathbf{0}_{3x1} \end{bmatrix} + \begin{bmatrix} \mathbf{0}_{3x1} & \mathbf{G}_4 \end{bmatrix}$$

$$\bar{\boldsymbol{\rho}}_b \equiv \begin{bmatrix} 1 & \rho_1 & \rho_1^2 & \rho_1^3 \end{bmatrix}$$
(A.53)

Now obtain the 3 new constants  $G_8$ ,  $g_7$ , and  $g_8$  to solve the  $6^{th}$  order equation for  $\rho_1$ . More than one method can be used to solve Eq. A.54, but this research uses the MATLAB function *roots* to obtain 6 possible values of  $\rho_1$ .

$$\mathbf{g}_{8}^{T} \bar{\boldsymbol{\rho}}_{c} = 0 \tag{A.54}$$

$$\mathbf{G}_{8}(1,1) - \mathbf{g}_{7}(1)$$

$$\mathbf{G}_{8}(2,1) + \mathbf{G}_{8}(1,2) - \mathbf{g}_{7}(2)$$

$$\mathbf{G}_{8}(3,1) + \mathbf{G}_{8}(2,2) + \mathbf{G}_{8}(1,3) - \mathbf{g}_{7}(3)$$

$$\mathbf{G}_{8}(4,1) + \mathbf{G}_{8}(3,2) + \mathbf{G}_{8}(2,3) + \mathbf{G}_{8}(1,4)$$

$$\mathbf{G}_{8}(4,2) + \mathbf{G}_{8}(3,3) + \mathbf{G}_{8}(2,4)$$

$$\mathbf{G}_{8}(4,3) + \mathbf{G}_{8}(3,4)$$

$$\mathbf{G}_{8}(4,4)$$

$$\mathbf{G}_{8}(4,4)$$

$$\mathbf{G}_{8}(4,4)$$

 $\bar{\boldsymbol{\rho}}_c \equiv \begin{bmatrix} 1 & \rho_1 & \rho_1^2 & \rho_1^3 & \rho_1^4 & \rho_1^5 & \rho_1^6 \end{bmatrix}$ 

Root Disambiguation Six roots are produced from solving Eq. A.55. See Fig. 99 for the disambiguation process. When the ground tracks of the satellites are close to the transmitter it is likely that two solutions within the coverage area will arise. In practice, information such as the receiver antenna beam orientation might be needed to choose the proper solution [3]. Typically there are two positive roots, and no valid complex conjugates as in TDOA3 and TDOA4.

Finally, the proper  $\rho_1$  is used to find  $\bar{\rho}_a$  Eq. A.50,  $\dot{\rho}_1$  Eq. A.52, and subsequently **u**.

$$\mathbf{u} = \mathbf{G}_4 \bar{\boldsymbol{\rho}}_a + \mathbf{g}_5 \dot{\boldsymbol{\rho}}_1 \tag{A.55}$$

Iteration for Altitude As in Sec. A.2.2, the first ITL solution  $\hat{\mathbf{u}}$  is used to update  $r_e$  based on Level 0 digital elevation data.

### A.3.2 TFDOA3

If there are 3 or more satellites then the system is overdetermined with at least 4 total equations (2 TDOA and 2 T/FDOA equations) and only 3 unknowns  $\mathbf{u} = [x_t, y_t, z_t]^T$ . Ho and Chan [23] provide a general solution for the  $S \geq 3$  case which is utilized in this research. Note that while this section is titled TFDOA3, this algorithm is applied to TFDOA4, the only difference is the number of input measurements, as well as number of SV positions and velocities.

**Inputs** The TDOA and FDOA measurements, positions, and velocities an are required. The spherical Earth mean radius 6371 km is used as an initial guess by

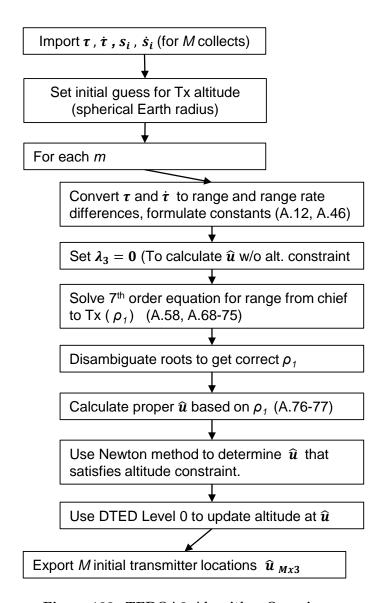


Figure 103. TFDOA3 Algorithm Overview

default.

$$\boldsymbol{\tau}_{M\times S-1} = \begin{bmatrix} \tau_{21} & \dots & \tau_{S1} \\ \vdots & \vdots & \vdots \end{bmatrix}, \dot{\boldsymbol{\tau}}_{M\times S-1} = \begin{bmatrix} \dot{\tau}_{21} & \dots & \dot{\tau}_{S1} \\ \vdots & \vdots & \vdots \end{bmatrix}$$

$$\mathbf{S}_{i} = \begin{bmatrix} \mathbf{s}_{i,1}^{T} \\ \vdots \\ \mathbf{s}_{i,M}^{T} \end{bmatrix}, \dot{\mathbf{S}}_{i} = \begin{bmatrix} \dot{\mathbf{s}}_{i,1}^{T} \\ \vdots \\ \dot{\mathbf{s}}_{i,M}^{T} \end{bmatrix}, i = 1, 2, \dots, S$$

$$(A.56)$$

Equation Set Up For the  $S \ge 3$  case, there are S-1 TDOA measurements and S-1 FDOA measurements, and therefore 2S-2 total equations. Recall Eq. A.47 and Eq. A.48 from Sec. A.3.1. Move all of the terms to the left side.

$$r_{i1}^{2} - \mathbf{s}_{i}^{T} \mathbf{s}_{i} + \mathbf{s}_{1}^{T} \mathbf{s}_{1} + 2(\mathbf{s}_{i} - \mathbf{s}_{1})^{T} \mathbf{u} + 2r_{i1}\rho_{1} = 0$$

$$2r_{i1}\dot{r}_{i1} - 2\mathbf{s}_{i}^{T}\dot{\mathbf{s}}_{i} + 2\mathbf{s}_{1}^{T}\dot{\mathbf{s}}_{1} + 2(\dot{\mathbf{s}}_{i} - \dot{\mathbf{s}}_{1})^{T} \mathbf{u} + 2r_{i1}\dot{r}_{1t} + 2\dot{r}_{i1}\rho_{1} = 0$$

$$i = 2, 3, ..., S$$
(A.57)

Ho and Chan [23] relate the range measurements  $r_{i1}$  and  $\dot{r}_{i1}$  to the transmitter position **u**. In matrix form this becomes

$$\mathbf{h} - \mathbf{G}_{1}\mathbf{u} - \mathbf{g}_{2}\rho_{1} - \mathbf{g}_{3}\dot{\rho}_{1} = \mathbf{0}$$

$$(A.58)$$

$$\mathbf{h} = \begin{bmatrix} r_{21}^{2} - \mathbf{s}_{2}^{T}\mathbf{s}_{2} + \mathbf{s}_{1}^{T}\mathbf{s}_{1} \\ r_{31}^{2} - \mathbf{s}_{3}^{T}\mathbf{s}_{3} + \mathbf{s}_{1}^{T}\mathbf{s}_{1} \\ \dots \\ r_{S1}^{2} - \mathbf{s}_{S}^{T}\mathbf{s}_{S} + \mathbf{s}_{1}^{T}\mathbf{s}_{1} \\ 2r_{21}\dot{r}_{21} - 2\mathbf{s}_{2}^{T}\dot{\mathbf{s}}_{2} + 2\mathbf{s}_{1}^{T}\dot{\mathbf{s}}_{1} \\ 2r_{31}\dot{r}_{31} - 2\mathbf{s}_{3}^{T}\dot{\mathbf{s}}_{3} + 2\mathbf{s}_{1}^{T}\dot{\mathbf{s}}_{1} \\ \dots \\ 2r_{S1}\dot{r}_{S1} - 2\mathbf{s}_{S}^{T}\dot{\mathbf{s}}_{S} + 2\mathbf{s}_{1}^{T}\dot{\mathbf{s}}_{1} \end{bmatrix}, \mathbf{G}_{1} \equiv -2 \begin{bmatrix} \mathbf{s}_{2}^{T} - \mathbf{s}_{1}^{T} \\ \mathbf{s}_{3}^{T} - \mathbf{s}_{1}^{T} \\ \vdots \\ \mathbf{s}_{2}^{T} - \mathbf{s}_{1}^{T} \\ \vdots \\ \mathbf{s}_{3}^{T} - \mathbf{s}_{1}^{T} \\ \vdots \\ \vdots \\ \vdots \\ \mathbf{s}_{3}^{T} - \mathbf{s}_{1}^{T} \\ \vdots \\ \mathbf{s}_{3}^{T} - \mathbf{s}_{1}^{T} \\ \vdots \\ \vdots \\ \vdots \\ \mathbf{s}_{3}^{T} - \mathbf{s}_{1}^{T} \\ \vdots \\ \vdots \\ \mathbf{s}_{3}^{T} - \mathbf{s}_{1}^{T} \\ \vdots \\ \vdots \\ \mathbf{s}_{3}^{T} - \mathbf{s}_{1$$

In an ideal situation these equations could be satisfied, but in a real, overdetermined situation a solution for the transmitter must be found that minimizes Eq. A.58, i.e. brings the left side as close to zero as possible. Thus a cost function  $\xi$  is defined that squares Eq. A.58 and weights it with W, incorporating three constraint equations and corresponding Lagrange multipliers  $\lambda_1$ ,  $\lambda_2$ , and  $\lambda_3$ . The first constraint is obtained by rearranging the TDOA equation Eq. A.50 for the reference satellite. The second constraint is obtained from expanding and rearranging Eq. 2.7, which is the relation between  $\dot{\rho}_1$  and unknown transmitter  $\mathbf{u}$ . The third equation corresponding to  $\lambda_3$  constrains  $\mathbf{u}$  to the assumed altitude  $r_e$ .

$$\xi = (\mathbf{h} - \mathbf{G}_1 \mathbf{u} - \mathbf{g}_2 \rho_1 - \mathbf{g}_3 \dot{\rho}_1)^T \mathbf{W} (\mathbf{h} - \mathbf{G}_1 \mathbf{u} - \mathbf{g}_2 \rho_1 - \mathbf{g}_3 \dot{\rho}_1)$$

$$+ \lambda_1 (2\mathbf{s}_1^T \mathbf{u} - \mathbf{s}_1^T \mathbf{s}_1 - r_e^2 + \rho_1^2) + \lambda_2 (2\dot{\mathbf{s}}_1^T \mathbf{u} - 2\mathbf{s}_1^T \dot{\mathbf{s}}_1 + 2\rho_1^2 \dot{\rho}_1)$$

$$+ \lambda_3 (\mathbf{u}^T \mathbf{u} - r_e^2)$$
(A.59)

The proper estimate  $\hat{\mathbf{u}}$  is the one that minimizes  $\xi$ . The first term represents the weighted error of the combined TDOA and T/FDOA equations.

**Derivation of W** The TDOA equations for non-reference satellites can be seen in the first S-1 rows of Eq. A.58, while the T/FDOA equations are in the second S-1 rows. The TDOA equation error due to TDOA measurement noise can be inferred from Eq. A.58. Here  $\mathbf{u}$ ,  $\rho_1$ , and  $\dot{\rho}_1$  are the true values, and  $\mathbf{h}$ ,  $\mathbf{G}_1$ , and  $\mathbf{g}_2$  are measured.

$$\begin{bmatrix} \phi_t \\ \phi_f \end{bmatrix} \equiv \mathbf{h} - \mathbf{G}_1 \mathbf{u} - \mathbf{g}_2 \rho_1 - \mathbf{g}_3 \dot{\rho}_1 \tag{A.60}$$

The true  $\mathbf{u}$ ,  $\rho_1$ , and  $\dot{\rho}_1$  are unknown, so Ho and Chan [23] derive the error in terms of the true measurement error and the ranges  $\rho_i$  (i=2,...,S).  $e_{\tau}$  represents the true TDOA measurement error in seconds and  $e_{\dot{\tau}}$  is the nondimensionalized FDOA

measurement error.

$$\phi_{t,i} = c\rho_i e_\tau + c^2 e_\tau^2 \approx c\rho_i e_\tau$$

$$\phi_{f,i} = c\dot{\rho}_i e_\tau + c\rho_i e_{\dot{\tau}} + 2c^2 e_\tau e_{\dot{\tau}} \approx c\dot{\rho}_i e_\tau + c\rho_i e_{\dot{\tau}}$$
(A.61)

The last terms can be eliminated from Eq. A.61 due to the small measurement noise assumption,  $\rho_i \gg ce_{\tau}$ . The matrix **W** weights the TDOA and T/FDOA equation error.

$$\mathbf{W} = E[[\phi_t^T, \phi_f^T]^T [\phi_t^T, \phi_f^T]]^{-1}$$
(A.62)

W can be obtained by inserting Eq. A.61 into Eq. A.62 and expanding. This derivation will assume S=3 for convenience, but same process applies for S>3. Assume TDOA and FDOA measurement errors are uncorrelated, thus  $E[e_{\tau_i}e_{\dot{\tau}_i}]=0$ . Also assume  $E[e_{\tau_i}e_{\tau_j}]=0$ ,  $i\neq j$ . Expanding the expectation, we get:

$$E\left\{ \left[ \phi_{t,1} \ \phi_{t,2} \ \phi_{f,1} \ \phi_{f,2} \right]^T \left[ \phi_{t,1} \ \phi_{t,2} \ \phi_{f,1} \ \phi_{f,2} \right] \right\} = \\ E\left\{ \begin{aligned} & \left\{ e^{2} \left[ \begin{array}{cccc} \rho_{2}e^{2}_{\tau_{21}} & 0 & \rho_{2}\dot{\rho}_{2}e^{2}_{\tau_{21}} & 0 \\ 0 & \rho_{3}^{2}e^{2}_{\tau_{31}} & 0 & \rho_{3}\dot{\rho}_{3}e^{2}_{\tau_{31}} \\ \rho_{2}\dot{\rho}_{2}e^{2}_{\tau_{21}} & 0 & \dot{\rho}_{2}^{2}e^{2}_{\tau_{21}} + \rho_{2}^{2}e^{2}_{\tau_{21}} & 0 \\ 0 & \rho_{3}\dot{\rho}_{3}e^{2}_{\tau_{31}} & 0 & \dot{\rho}_{3}^{2}e^{2}_{\tau_{31}} + \rho_{3}^{2}e^{2}_{\tau_{31}} \\ 0 & \rho_{3}\dot{\rho}_{3}e^{2}_{\tau_{31}} & 0 & \dot{\rho}_{3}^{2}e^{2}_{\tau_{31}} + \rho_{3}^{2}e^{2}_{\tau_{31}} \\ 0 & \rho_{3}\dot{\rho}_{3}E[e_{\tau_{31}}e_{\tau_{31}}] & 0 & \rho_{3}\dot{\rho}_{3}E[e_{\tau_{31}}e_{\tau_{31}}] \\ \rho_{2}\dot{\rho}_{2}E[e_{\tau_{21}}e_{\tau_{21}}] & 0 & \dot{\rho}_{2}^{2}E[e_{\tau_{21}}e_{\tau_{21}}] + \rho_{2}^{2}E[e_{\tau_{21}}e_{\tau_{21}}] & 0 \\ 0 & \rho_{3}\dot{\rho}_{3}e^{2}_{\tau_{31}} & 0 & \dot{\rho}_{3}^{2}E[e_{\tau_{31}}e_{\tau_{31}}] \\ 0 & \rho_{3}\dot{\rho}_{3}e^{2}_{\tau_{31}} & 0 & \dot{\rho}_{3}^{2}E[e_{\tau_{31}}e_{\tau_{31}}] + \rho_{3}^{2}E[e_{\tau_{31}}e_{\tau_{31}}] \end{aligned} \right. \tag{A.63}$$

Note that the measurement noise is independent and Gaussian, thus each expectation can be substituted with its corresponding noise variance.

$$\sigma_{\tau_i}^2 = E[e_{\tau_i} e_{\tau_i}]$$

$$\sigma_{\dot{\tau}_i}^2 = E[e_{\dot{\tau}_i} e_{\dot{\tau}_i}]$$
(A.64)

$$\begin{split} E[[\phi_t^T,\phi_f^T]^T[\phi_t^T,\phi_f^T]] = \\ 4c^2 \begin{bmatrix} \rho_2\sigma_{\tau_{21}}^2 & 0 & \rho_2\dot{\rho}_2\sigma_{\tau_{21}}^2 & 0 \\ 0 & \rho_3^2\sigma_{\tau_{31}}^2 & 0 & \rho_3\dot{\rho}_3\sigma_{\tau_{31}}^2 \\ \rho_2\dot{\rho}_2\sigma_{\tau_{21}}^2 & 0 & \dot{\rho}_2^2\sigma_{\tau_{21}}^2 + \rho_2^2\sigma_{\tau_{21}}^2 & 0 \\ 0 & \rho_3\dot{\rho}_3\sigma_{\tau_{31}}^2 & 0 & \dot{\rho}_3^2\sigma_{\tau_{31}}^2 + \rho_3^2\sigma_{\tau_{31}i}^2 \end{bmatrix} \end{split} \tag{A.65}$$

Then Eq. A.65 can be written in matrix form based on new variables  $\mathbf{B}$ ,  $\dot{\mathbf{B}}$  and the measurement covariances  $\mathbf{Q}_t$  and  $\mathbf{Q}_f$ . Note that the constant 4 is factored into  $\mathbf{B}$  and  $\dot{\mathbf{B}}$  to agree with [23].

$$E\left\{\dots\right\} = c^{2} \left\{ \begin{bmatrix} \mathbf{B} & 0 \\ \dot{\mathbf{B}} & \mathbf{B} \end{bmatrix} \begin{bmatrix} \mathbf{Q}_{t} & 0 \\ 0 & \mathbf{Q}_{f} \end{bmatrix} \begin{bmatrix} \mathbf{B} & \dot{\mathbf{B}} \\ 0 & \mathbf{B} \end{bmatrix} \right\}$$

$$\mathbf{B} = diag(\rho_{2}, \dots, \rho_{i}) \quad \dot{\mathbf{B}} = diag(\dot{\rho}_{2}, \dots, \dot{\rho}_{i})$$

$$\mathbf{Q}_{t} = \begin{bmatrix} \sigma_{\tau_{21}}^{2} & 0 \\ 0 & \sigma_{\tau_{31}}^{2} \end{bmatrix} \quad \mathbf{Q}_{f} = \begin{bmatrix} \sigma_{\tau_{21}i}^{2} & 0 \\ 0 & \sigma_{\tau_{31}i}^{2} \end{bmatrix}$$

$$(A.66)$$

Therefore, ignoring scaling factor  $c^2$ , Eq. A.62 can be simmplified to

$$\mathbf{W} = E \left\{ \dots \right\}^{-1} = \left\{ \begin{bmatrix} \mathbf{B} & 0 \\ \dot{\mathbf{B}} & \mathbf{B} \end{bmatrix} \begin{bmatrix} \mathbf{Q}_t & 0 \\ 0 & \mathbf{Q}_f \end{bmatrix} \begin{bmatrix} \mathbf{B} & \dot{\mathbf{B}} \\ 0 & \mathbf{B} \end{bmatrix} \right\}^{-1}$$
(A.67)

In practice  $\mathbf{W}$  is scaled so that it's maximum term has unit magnitude. The scaling of  $\mathbf{W}$  affects the eigenvalues of the first term in Eq. A.59, and thus influences the increments of  $\lambda_3$  used in application of the Secant method (Fig. 104). For a pass consisting of multiple sets of measurements M,  $\mathbf{W}$  can be calculated for each M or once per pass. From Eq. A.67 it can be deduced that two measurements of equal error may not result in identical T/FDOA equation error. The geometry of the satellites from which the measurement was taken also has an influence.

**Solving for \rho\_1** Ho and Chan [23] describe the derivations involved in obtaining  $\rho_1$ . This section will solely include the process of solving for  $\rho_1$ . First, let us examine the method of obtaining the proper weighting matrix **W**.

Using range and range difference measurements as well as receiver positions and velocities, obtain the constants  $\mathbf{h}$ ,  $\mathbf{G}_1$ ,  $\mathbf{g}_2$ , and  $\mathbf{g}_3$ . Eq. A.58 should be satisfied in the noise-free case. Next, the constants  $\mathbf{g}_7$ ,  $\mathbf{G}_5$ , and  $\mathbf{g}_8$  should be determined since they are not dependent on  $\lambda_3$ , which will later be varied.

$$\mathbf{g}_{7} = \begin{bmatrix} \mathbf{s}_{1}^{T} \mathbf{s}_{1} + r_{e}^{2} & 0 & -1 & 0 & 0 \end{bmatrix}^{T}$$

$$\mathbf{G}_{5} = \begin{bmatrix} \mathbf{h}, -\mathbf{g}_{2}, \mathbf{0}, -\mathbf{g}_{3}, \mathbf{0} \end{bmatrix}$$

$$\mathbf{g}_{8} = \begin{bmatrix} 2\dot{\mathbf{s}}_{1}^{T} \dot{\mathbf{s}}_{1}, 0, 0, 0, -2 \end{bmatrix}$$
(A.68)

From now on the constants needed to solve for  $\rho_1$  depend on the Lagrange multiplier  $\lambda_3$ . Start with  $\lambda_3 = 0$ , which signifies relaxing the Earth surface constraint. Then

calculate  $\mathbf{G}_4$ ,  $\mathbf{G}_6$ ,  $\mathbf{g}_9$ , and  $\mathbf{g}_{10}$ .

$$\mathbf{G}_{4} = (\mathbf{G}_{1}^{T}\mathbf{W}\mathbf{G}_{1} + \lambda_{3}\mathbf{I})^{-1} \qquad \mathbf{I} = identity$$

$$\mathbf{G}_{6} = \mathbf{G}_{4}\mathbf{G}_{1}^{T}\mathbf{W}\mathbf{G}_{5}$$

$$\begin{bmatrix} \mathbf{g}_{9}^{T} \\ \mathbf{g}_{10}^{T} \end{bmatrix} = \frac{1}{2} \begin{bmatrix} \mathbf{s}_{1}^{T}\mathbf{G}_{4}\mathbf{s}_{1} & \mathbf{s}_{1}^{T}\mathbf{G}_{4}\dot{\mathbf{s}}_{1} \\ \dot{\mathbf{s}}_{1}^{T}\mathbf{G}_{4}\mathbf{s}_{1} & \dot{\mathbf{s}}_{1}^{T}\mathbf{G}_{4}\dot{\mathbf{s}}_{1} \end{bmatrix}^{-1} \begin{bmatrix} 2\mathbf{s}_{1}\mathbf{G}_{6} - \mathbf{g}_{7}^{T} \\ 2\dot{\mathbf{s}}_{1}\mathbf{G}_{6} - \mathbf{g}_{8}^{T} \end{bmatrix}$$

$$(A.69)$$

Any change in  $\lambda_3$  only affects the eigenvalues of  $\mathbf{G}_4$ , so an eigenvalue decomposition [55] can be conducted on  $\mathbf{G}_1^T \mathbf{W} \mathbf{G}_1$  to avoid matrix inversion Eq. A.70. This decreases computation time, especially when the Newton method requires recalculating  $\mathbf{G}_4$  for each new  $\lambda_3$ .  $\mathbf{D}$  is the diagonal matrix and  $\mathbf{X}$  contains the eigenvectors.

$$\mathbf{G}_{4} = (\mathbf{G}_{1}^{T}\mathbf{W}\mathbf{G}_{1} + \lambda_{3}\mathbf{I})^{-1} = (\mathbf{Y} + \lambda_{3}\mathbf{I})^{-1}$$

$$= (\mathbf{X}\mathbf{D}\mathbf{X}^{-1} + \lambda_{3}\mathbf{I})^{-1}$$

$$= [\mathbf{X}(\mathbf{D} + \lambda_{3}\mathbf{I})\mathbf{X}^{-1}]^{-1}$$

$$= \mathbf{X}(\mathbf{D} + \lambda_{3}\mathbf{I})^{-1}\mathbf{X}^{-1}$$
(A.70)

Then  $G_{11}$  and  $G_{12}$  can be solved for.

$$\mathbf{G}_{11} = \mathbf{G}_6 - \mathbf{G}_4(\mathbf{s}_1 \mathbf{g}_9^T + \dot{\mathbf{s}}_1 \mathbf{g}_{10}^T)$$

$$\mathbf{G}_{12} = \mathbf{G}_5 - \mathbf{G}_1 \mathbf{G}_{11}$$
(A.71)

Determine the constants  $\mathbf{g}_{13}$ ,  $\mathbf{g}_{14}$ , and  $\mathbf{g}_{15}$ .

$$\mathbf{g}_{13} \equiv \mathbf{G}_{12}^{T} \mathbf{W}^{T} \mathbf{g}_{3}$$

$$\mathbf{g}_{14} \equiv [-g_{13}(4), g_{10}(4) - g_{13}(5), g_{10}(5), 0, 0]^{T}$$

$$\mathbf{g}_{15} \equiv [-g_{13}(4), g_{10}(4) - g_{13}(5), g_{10}(5), 0, 0]^{T}$$
(A.72)

Determine the constants  $G_{16}$ ,  $G_{17}$ , and  $G_{18}$ , and C.

$$\mathbf{G}_{16} \equiv [\mathbf{g}_{14}, \mathbf{C}\mathbf{g}_{14}, \mathbf{C}^{2}\mathbf{g}_{14}, \mathbf{g}_{15}, \mathbf{C}\mathbf{g}_{15}]^{T}$$

$$\mathbf{G}_{17} \equiv \mathbf{g}_{14}\mathbf{g}_{9}^{T}\mathbf{G}_{16}$$

$$\mathbf{G}_{18} \equiv (\mathbf{g}_{15}\mathbf{g}_{10}^{T} - \mathbf{g}_{14}\mathbf{g}_{2}^{T}\mathbf{W}\mathbf{G}_{12})\mathbf{G}_{12}$$

$$\mathbf{C} \equiv \begin{bmatrix} 0 & 0 & 0 & 0 & 1 \\ 1 & 0 & 0 & 0 & 0 \\ 0 & 1 & 0 & 0 & 0 \\ 0 & 0 & 1 & 0 & 0 \\ 0 & 0 & 0 & 1 & 0 \end{bmatrix}$$
(A.73)

Now the  $7^{th}$  order equation for  $\rho_1$  can be solved.

$$\rho_1 \bar{\boldsymbol{\rho}}_d^T \mathbf{G}_{17} \bar{\boldsymbol{\rho}}_d + \bar{\boldsymbol{\rho}}_d^T \mathbf{G}_{18} \bar{\boldsymbol{\rho}}_d = 0$$

$$\bar{\boldsymbol{\rho}}_d \equiv [1, \rho_1, \rho_1^2, \rho_1^3, \rho_1^4]^T$$
(A.74)

This  $7^{th}$  order equation can be rearranged algebraically and solved with the MATLAB function roots to obtain 7 possible values for  $\rho_1$ .

$$\mathbf{g}_{19}^{T}[\rho_{1}^{7}, \rho_{1}^{6}, \rho_{1}^{5}, \rho_{1}^{4}, \rho_{1}^{3}, \rho_{1}^{2}, \rho_{1}, 1]^{T} = 0 \tag{A.75}$$

$$\mathbf{g}_{19} \equiv \begin{bmatrix} \mathbf{G}_{17}(3,5) + \mathbf{G}_{18}(4,5) \\ \mathbf{G}_{17}(3,4) + \mathbf{G}_{17}(2,5) + \mathbf{G}_{18}(4,4) + \mathbf{G}_{18}(3,5) \\ \mathbf{G}_{17}(3,3) + \mathbf{G}_{17}(2,4) + \mathbf{G}_{17}(1,5) + \mathbf{G}_{18}(4,3) + \mathbf{G}_{18}(3,4) + \mathbf{G}_{18}(2,5) \\ \mathbf{G}_{17}(3,2) + \mathbf{G}_{17}(2,3) + \mathbf{G}_{17}(1,4) + \mathbf{G}_{18}(4,2) + \mathbf{G}_{18}(3,3) + \mathbf{G}_{18}(2,4) + \mathbf{G}_{18}(1,5) \\ \mathbf{G}_{17}(3,1) + \mathbf{G}_{17}(2,2) + \mathbf{G}_{17}(1,3) + \mathbf{G}_{18}(4,1) + \mathbf{G}_{18}(3,2) + \mathbf{G}_{18}(2,3) + \mathbf{G}_{18}(1,4) \\ \mathbf{G}_{17}(2,1) + \mathbf{G}_{17}(1,2) + \mathbf{G}_{18}(3,1) + \mathbf{G}_{18}(2,2) + \mathbf{G}_{18}(1,3) \\ \mathbf{G}_{17}(1,1) + \mathbf{G}_{18}(2,1) + \mathbf{G}_{18}(1,2) \end{bmatrix}$$

**Disambiguate Roots** The 7 roots produced from solving Eq. A.74 need to be disambiguated (Ref fig). There is typically only one positive root because the system is overdetermined [23]. The proper root is used to determine  $\bar{\rho}_d$  Eq. A.74  $,\dot{\rho}_1$ , and  $\bar{\rho}_e$ .

$$\dot{\rho}_{1} = \frac{\mathbf{g}_{15}^{T} \bar{\boldsymbol{\rho}}_{d}}{\mathbf{g}_{14}^{T} \bar{\boldsymbol{\rho}}_{d}}$$

$$\bar{\boldsymbol{\rho}}_{e} = \left[1, \rho_{1}, \rho_{1}^{2}, \dot{\rho}_{1}, \rho_{1} \dot{\rho}_{1}\right]^{T}$$
(A.76)

Then an estimate for  $\mathbf{u}$  can be obtained.

$$\hat{\mathbf{u}} = \mathbf{G}_{11}\bar{\boldsymbol{\rho}}_e \tag{A.77}$$

**Newton Method** The process from Eq. A.69 to Eq. A.77 represents the calculation of  $\hat{\mathbf{u}}$  when the altitude constraint is relaxed, i.e.  $\lambda_3 = 0$ . The next step is to search for the  $\lambda_3$  that satisfies Eq. A.78.

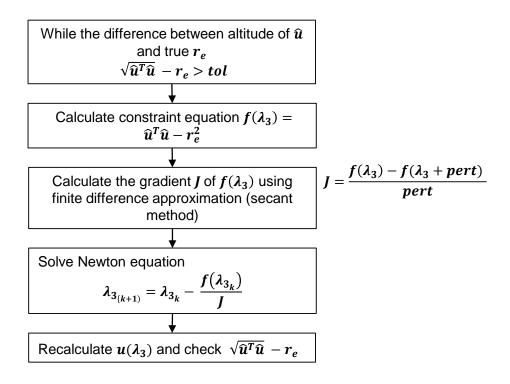


Figure 104. Solving for  $\rho_1$  using Newton Method

$$f(\lambda_3) = \mathbf{u}^T \mathbf{u} - r_e^2 = 0 \tag{A.78}$$

The correct  $\lambda_3$  is the zero of  $f(\lambda_3)$  closest to  $\lambda_3 = 0$ , or in other words, the one which utilizes the altitude constraint the least. Ho and Chan [23] suggest using Newton method to find  $\lambda_3$ . This research uses finite differences, also known as the Secant method, as a numerical approximation of the Newton method. The  $\lambda_3$  search implementation is outlined below.

The tolerance is the maximum allowable distance between the altitude of  $\hat{\mathbf{u}}$  and desired altitude  $r_e$ . The magnitude of perturbation  $\tilde{\lambda}_3$  is sensitive to the eigenvalues of  $\mathbf{W}$ .  $\tilde{\lambda}_3$  was chosen to be 100 for this research. Inappropriate scaling of  $\tilde{\lambda}_3$  relative to  $\mathbf{W}$  cause the Newton method to fail because  $f(\lambda_3)$  is dominated by the noise of numerical inprecision.

# Appendix B. Additional Methods

This appendix contains the process of importing digital terrain elevation data (DTED) for this research.

### **B.1** Importing DTED

Digital elevation data can be imported from a variety of sources, however the data utilized in this research was obtained from the US Geological Survey (USGS) Earth Explorer website. The DTED level 1 used for this research was SRTM Void Filled 3-arc second DTED. SRTM 1-arc second global DTED was used for DTED2. Information about this SRTM data can be obtained from [60]. The DTED level 0 used for altitude iteration within the ITL methods was obtained from Global Multi-resolution Terrain Elevation Data (GMTED) 2010 [63]. All data used was free, unclassified, and required the creation of an account with USGS.

### B.1.1 DTED Level 0

GMTED 2010 is an improvement to the formerly developed model GTOPO30 [63]. In Earth Explorer the GMTED 2010 data is formatted as a GeoTiff (.tif) file, which can be read into raster format using the MATLAB command geotiffread, resulting in a MxN double containing the elevation at each coordinate in meters. The mean elevation data was used for this thesis. To reduce computation time within ITL algorithms the orthometric heights H were combined with geoid heights N to produce ellipsoid heights h. These ellipsoid heights were stored in a MATLAB double.

### B.1.2 DTED Levels 1 and 2

The SRTM data used for Level 1 and 2 mentioned above can be downloaded in DTED format (.dt1 or .dt2) from Earth Explorer. The MATLAB command *dted* was

utilized to convert the DTED file to an  $M \times N$  double containing the elevation at each coordinate in meters (raster data). More info can be obtained from [60] and [63].

# Appendix C. Additional Results

This appendix contains the additional results obtained for the analysis of ITL sensitivity to SV location error, discussed in Sec. 4.6. It also contains a graph that supplements the system level performance analysis in Sec. 5.3.2.

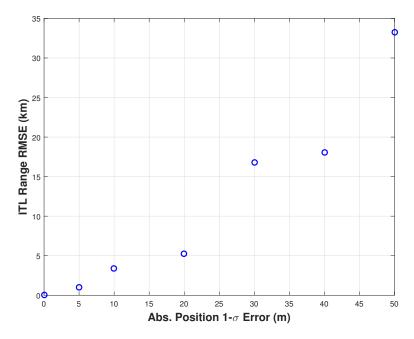


Figure 105. TDOA4 algorithm sensitivity to absolute position error (Tx 1, Pass 3, 1 collect, 10,000 trials)

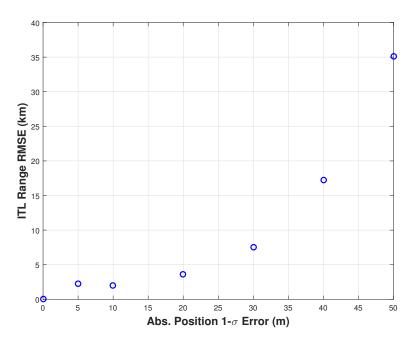


Figure 106. TFDOA2 algorithm sensitivity to absolute position error (Tx 1, Pass 3, 1 collect, 10,000 trials)

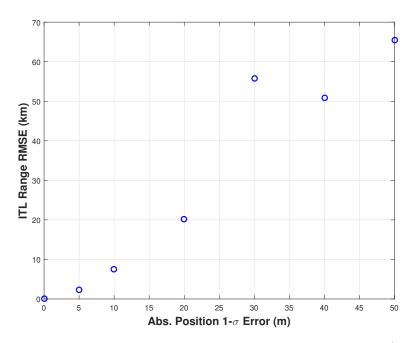


Figure 107. TFDOA3 algorithm sensitivity to absolute position error (Tx 1, Pass 3, 1 collect, 10,000 trials)

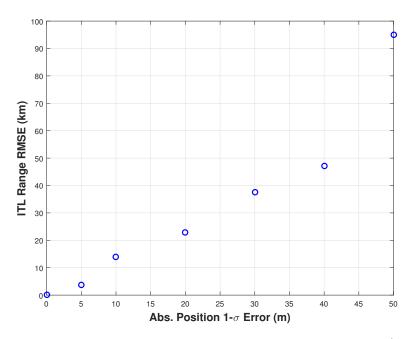


Figure 108. TFDOA4 algorithm sensitivity to absolute position error (Tx 1, Pass 3, 1 collect, 10,000 trials)

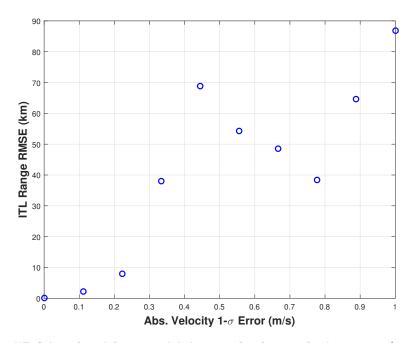


Figure 109. TFDOA2 algorithm sensitivity to absolute velocity error (Tx 1, Pass 3, 1 collect, 10,000 trials)

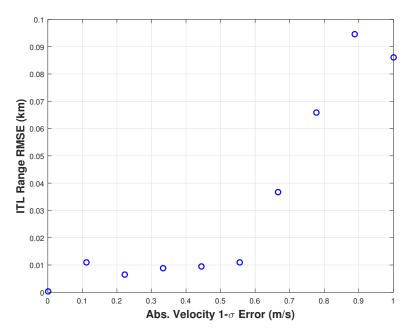


Figure 110. TFDOA3 algorithm sensitivity to absolute velocity error (Tx 1, Pass 3, 1 collect, 10,000 trials)

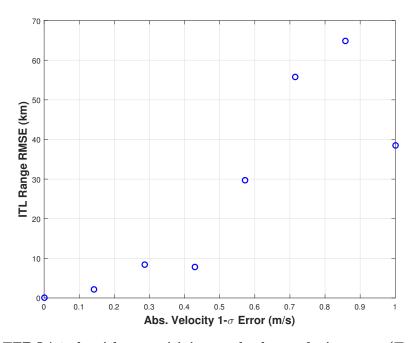


Figure 111. TFDOA4 algorithm sensitivity to absolute velocity error (Tx 1, Pass 3, 1 collect, 10,000 trials)

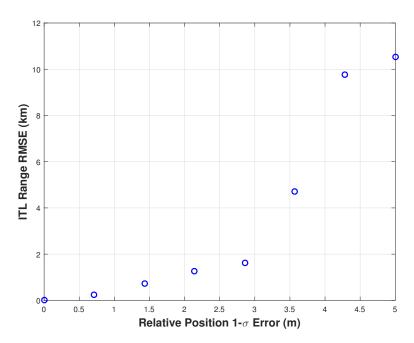


Figure 112. TDOA3 algorithm sensitivity to relative position error (Tx 1, Pass 3, 1 collect, 10,000 trials)

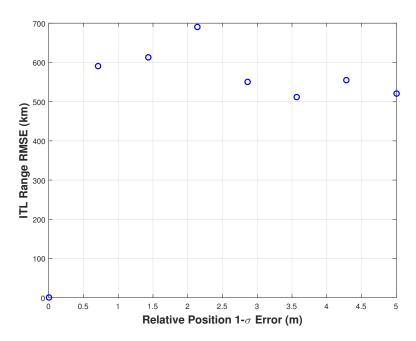


Figure 113. TDOA4 algorithm sensitivity to relative position error (Tx 1, Pass 3, 1 collect, 10,000 trials)

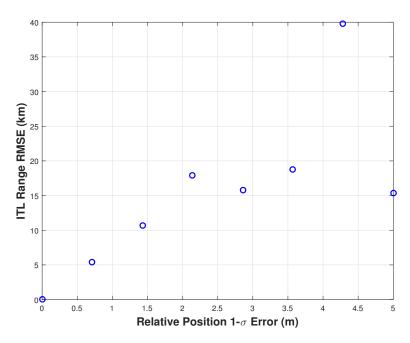


Figure 114. TFDOA2 algorithm sensitivity to relative position error (Tx 1, Pass 3, 1 collect, 10,000 trials)

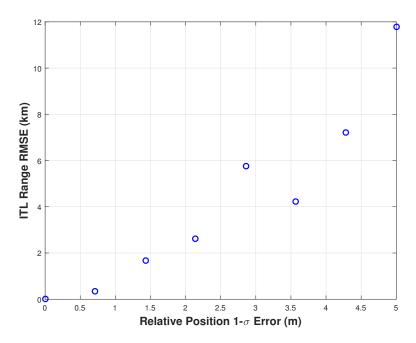


Figure 115. TFDOA3 algorithm sensitivity to relative position error (Tx 1, Pass 3, 1 collect, 10,000 trials)

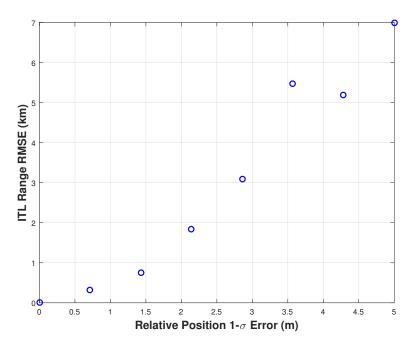


Figure 116. TFDOA4 algorithm sensitivity to relative position error (Tx 1, Pass 3, 1 collect, 10,000 trials)

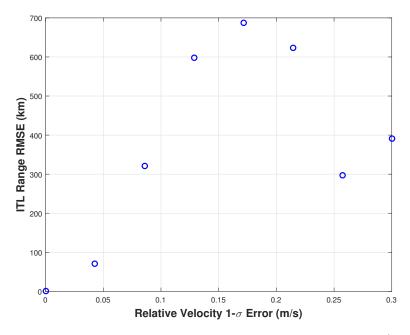


Figure 117. TFDOA2 algorithm sensitivity to relative velocity error (Tx 1, Pass 3, 1 collect, 10,000 trials)

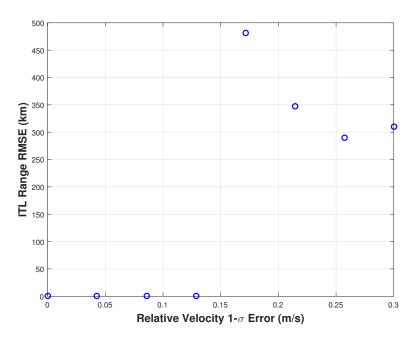


Figure 118. TFDOA3 algorithm sensitivity to relative velocity error (Tx 1, Pass 3, 1 collect, 10,000 trials)

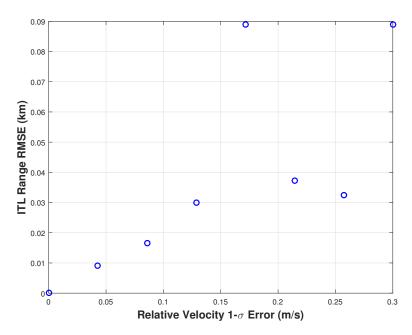


Figure 119. TFDOA4 algorithm sensitivity to relative velocity error (Tx 1, Pass 3, 1 collect, 10,000 trials)

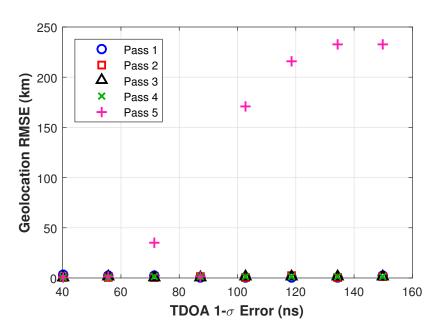


Figure 120. Effect of TDOA measurement error on TDOA4 geolocation accuracy with application of DTED1 Earth constraint (500 trials)

# **Bibliography**

- A. Marinan, "From CubeSats to Constellations: Systems Design and Performance Analysis," Master's thesis, Massachusetts Institute of Technology, 2013.
- 2. K. Alfriend et al., Spacecraft Formation Flying: Dynamics, Control, and Navigation, 1st ed. Butterworth-Heinemann, 2009.
- 3. F. Guo et al., Space Electronic Reconaissance: Localization Theories and Methods. Singapore: Wiley, 2014.
- 4. E. Bailey, "Single Platform Geolocation of Radio Frequency Emitters," Master's thesis, Air Force Institute of Technology, March 2015.
- C. L. Yatrakis, "Computing the cross-ambiguity function: A Review," Master's thesis, Binghamtom University, State University of New York, 2005.
- N. Durland, "Defining Mean Sea Level in Military Simulations with DTED," in SpringSim '09 Proceedings of the 2009 Spring Simulation Multiconference, Northtrop Grumman Corporation. Society for Computer Simulation International, 2009.
- A. Noureldin, T. B. Karamat, and J. Georgy, "Basic Navigational Mathematics, Reference Frames and the Earth's Geometry," in Fundamentals of Inertial Navigation, Satellite-based Positioning and their Integration. Springer-Verlag, 2013, pp. 21–63.
- 8. N. S. Schmidt, "Evaluation of the Military Utility of Employing an Angle of Arrival Payload Hosted on a CubeSat as an Augmentation to Existing Geolocation Systems," Master's thesis, Air Force Institute of Technology, March 2015.

- "Performance Specification Digital Terrain Elevation Data (DTED)."
   [Online]. Available: https://dds.cr.usgs.gov/srtm/version2\_1/Documentation/ MIL-PDF-89020B.pdf
- K. Roth et al., "ERIC ASYS 631 Final Report," Air Force Institute of Technology, Tech. Rep., 2016.
- 11. C. Gentile et al., Geolocation Techniques: Principles and Applications. Springer Publishing Company, Inc., 2012.
- 12. "Geolocation of RF Emitters with a Formation-Flying Cluster of Three Microsatellites," 30th Annual AIAA/USU Conference on Small Satellites, HawkEye 360, Inc, 2016.
- D. Musicki, R. Kaune, and W. Koch, "Mobile emitter geolocation and tracking using TDOA and FDOA measurements," *IEEE Transactions on Signal Process*ing, vol. 58, pp. 1863–1874, 2010.
- D. Cajacob et al., "Geolocation of RF Emitters with a Formation-Flying Cluster of Three Microsatellites," in 30th Annual AIAA/USU Conference on Small Satellites, vol. 6. HawkEye 360, Inc, 2016.
- K. Hale, "Expanding the Use of Time/Frequency Difference of Arrival Geolocation in the Department of Defense," Ph.D. dissertation, Pardee Rand Graduate School, 2012.
- "National Reconaissance Office Innovation Campaign: The CubeSat Program,"
   2013, Accessed: 8/9/2016. [Online]. Available: http://www.nro.gov/about/innovation/
- 17. M. Swartwout, "Cheaper by the dozen: The avalanche of rideshares in the 21st century," *IEEE Aerospace Conference Proceedings*, pp. 1–12, 2013.

- 18. E. Agasid *et al.*, "Small Spacecraft Technology State of the Art," Ames Research Center, National Aeronautics and Space Administration, Tech. Rep., 2015.
- S. Bandyopadhyay et al., "A Review of Impending Small Satellite Formation Flying Missions," in Proceedings of the 53rd AIAA Aerospace Sciences Meeting, 2015.
- 20. P. Gurfil, J. Herscovitz, and M. Pariente, "The SAMSON Project Cluster Flight and Geolocation with Three Autonomous Nano-satellites," in 26th Annual AIAA/USU Conference on Small Satellites, 2012. [Online]. Available: http://digitalcommons.usu.edu/smallsat/2012/all2012/56/
- 21. J. P. Basel, "Analysis of Geolocation Approaches Using Satellites," Master's thesis, Air Force Institute of Technology, March 2014.
- 22. S. D. Hartzell, "Non-Linear Optimization Applied to Angle-of-Arrival Satellite-Based Geolocation," Master's thesis, Air Force Institute of Technology, March 2014.
- 23. K. C. Ho and Y. T. Chan, "Geolocation of a known altitude object from TDOA and FDOA measurements," *IEEE Transactions on Aerospace and Electronic Systems*, vol. 33, no. 3, pp. 770–783, 1997.
- 24. S. Kulumani, "Space-based TDOA geolocation," AFRL/RVSV, Tech. Rep., 2013.
- 25. K. C. Ho, X. Lu, and L. Kovavisaruch, "Source localization using TDOA and FDOA measurements in the presence of receiver location errors: Analysis and solution," *IEEE Transactions on Signal Processing*, vol. 55, no. 2, pp. 684–696, 2007.
- S. Lee et al., "CubeSat Design Specification," California Polytechnic State University, Tech. Rep., 2015.

- E. BuPane et al., "GeoLoco ASYS 631 Final Report," Air Force Institute of Technology, Tech. Rep., 2013.
- 28. E. Bailey *et al.*, "Anubis ASYS 631 Final Report," Air Force Institute of Technology, Tech. Rep., 2014.
- 29. G. Bonin *et al.*, "CanX-4 and CanX-5 Precision Formation Flight: Mission Accomplished!" in *29th Annual AIAA/USU Conference on Small Satellites*, vol. 1, 2015.
- J. Raquet, "Part 2 System Overview," in EENG 533: Navigation Using GPS, 2016.
- 31. NASA, "CubeSat Proximity Operations Demonstration," 2016, Accessed: 1/26/2017. [Online]. Available: https://www.nasa.gov/sites/default/files/atoms/files/cpod\_fact\_sheet-7march2016.pdf
- 32. J. W. Gangestad, B. S. Hardy, and D. Hinkley, "Operations , Orbit Determination , and Formation Control of the AeroCube-4 CubeSats," in 27th Annual AIAA/USU Conference on Small Satellites. The Aerospace Corporation, 2013.
- 33. H. Curtis, Orbital Mechanics for Engineering Students. Elsevier, 2014.
- 34. Y. Albagory and A. Ashour, "MUSIC 2D-DOA Estimation using Split Vertical Linear and Circular Arrays," International Journal of Computer Network and Information Security, vol. 8, pp. 12–18, 2013.
- 35. P. Tan and P. Wang, "Study of 2D DOA Estimation for Uniform Circular Array in Wireless Location System," *Internation Journal of Computer Network and Information Security*, vol. 2, pp. 54–60, 2010.

- 36. R. Schmidt, "Multiple emitter location and signal parameter estimation," *IEEE Transactions on Antennas and Propagation*, vol. 34, no. 3, pp. 276–280, 1986.
- K. C. Ho and Y. T. Chan, "Solution and Performance Analysis of Geolocation by TDOA," *IEEE Transactions on Aerospace and Electronic Systems*, vol. 29, no. 4, pp. 1311–1322, 1993.
- 38. S. Stein, "Algorithms for ambiguity function processing," *IEEE Transactions on Acoustics, Speech, and Signal Processing*, vol. 29, pp. 588–599, 1981.
- 39. "Comparison of time-difference-of-arrival and angle-of-arrival methods of signal geolocation," International Telecommunication Union, Tech. Rep., 2011.
- 40. A. J. Sinclair, T. A. Lovell, and J. Darling, "RF localization solution using heterogeneous TDOA," in *IEEE Aerospace Conference Proceedings*, 2015, pp. 1–7.
- 41. A. J. Small, "Radio Frequency Emitter Geolocation Using Cubesats," Master's thesis, Air Force Institute of Technology, March 2014.
- 42. D. J. Torrieri, "Statistical Theory of Passive Location Systems," *IEEE Transactions on Aerospace and Electronic Systems*, vol. AES-20, no. 2, pp. 183–198, 1984.
- 43. W. H. Foy, "Position-Location Solutions By Taylor-Series Estimation." *IEEE Transactions on Aerospace and Electronic Systems*, vol. AES-12, no. 2, pp. 187–194, 1976.
- 44. K. C. Ho and W. Xu, "An accurate algebraic solution for moving source location using TDOA and FDOA measurements," *IEEE Transactions on Signal Process*ing, vol. 52, no. 9, pp. 2453–2463, 2004.

- 45. A. Amar, G. Leus, and B. Friedlander, "Emitter position and velocity estimation given time and frequency differences of arrival," in *Asilomar Conference on Signals, Systems and Computers*, 2010, pp. 589–593.
- 46. Y. Cao et al., "A new iterative algorithm for geolocating a known altitude target using TDOA and FDOA measurements in the presence of satellite location uncertainty," Chinese Journal of Aeronautics, vol. 28, no. 5, pp. 1510–1518, 2015.
- 47. H. Wu, H. Xiong, and J. Peng, "An analysis and algorithm for unknown altitude source geo-location using TDOA measurements in the presence of receiver location errors," in *International Conference on Graphic and Image Processing*, vol. 8285, 2011.
- 48. "Department of Defense World Geodetic System 1984," National Imagery and Mapping Agency, Tech. Rep., 2000, Accessed: 1/29/2017. [Online]. Available: http://earth-info.nga.mil/GandG/publications/tr8350.2/wgs84fin.pdf
- 49. N. Leiter, "Real-Time Geolocation with a Satellite Formation," in 27th Annual AIAA/USU Conference on Small Satellites, 2013, pp. 1–20.
- D. Kim, J. Ha, and K. You, "Adaptive extended Kalman filter based geolocation using TDOA/FDOA," *International Journal of Control and Automation*, vol. 4, no. 2, pp. 49–58, 2011.
- 51. W. E. Weisel, Modern Orbit Determination, 2nd ed. Aphelion Press, 2010.
- 52. Y. Zheng, Z. Chenguangl, and Z. Xiaomin, "Design and Experiment on Small Satellite Formation Flying Simulation Platform," *Institute of Electrical and Electronics Engineers*, pp. 244–247, 2005.

- 53. R. Ren, M. L. Fowler, and N. E. Wu, "Finding optimal trajectory points for TDOA/FDOA geo-location sensors," in 43rd Annual Conference on Information Sciences and Systems, CISS 2009, 2009, pp. 817–822.
- 54. S. van de Geer, "Least Squares Estimation," Encyclopedia of Statistics in Behavioral Science, vol. 2, pp. 1041–1045, 2005.
- 55. G. Strang, Linear Algebra and its Applications, 4th ed. Brooks/Cole, 2006.
- 56. M. Fowler, "Least-Squares Estimation," in EECE522 EstimationTheory, 2016, Accessed: 8/8/2016. [Online]. Available: http://www.ws.binghamton.edu/fowler/fowler%20personal%20page/ EE522\_files/EECE%20522%20Notes\_16%20Ch\_8A.pdf
- 57. L. Vandenberghe, "Nonlinear Least-Squares," in *EE 103 Applied Numerical Computing*, 2012, Accessed: 8/8/2016. [Online]. Available: http://www.seas.ucla.edu/~vandenbe/103/lectures/nlls.pdf
- 58. S. Kay, Fundamentals of Statistical Signal Processing. Prentice-Hall, 1998, vol. 1.
- 59. T. Farr *et al.*, "The shuttle radar topography mission," *Review of Geophysics*, vol. 45, no. 2005, 2007.
- 60. "Shuttle Radar Topography Mission (SRTM)," U.S. Geological Survey, January 2015, Accessed: 10/1/2016. [Online]. Available: https://lta.cr.usgs.gov/SRTM
- 61. "Guidelines for Digital Elevation Data," National Digital Elevation Program, Tech. Rep., 2004, Accessed: 10/1/2016. [Online]. Available: http://giscenter.isu.edu/pdf/NDEPElevationGuidelinesVer1.pdf
- 62. "Products," U.S. Geological Survey, January 2015, Accessed: 10/1/2016.

  [Online]. Available: https://lta.cr.usgs.gov/products\_overview

- 63. J. Danielson and D. Gesch, "Global Multi-resolution Terrain Elevation Data 2010 (GMTED2010)," U.S. Geological Survey, U.S. Department of the Interior, Tech. Rep., 2011.
- 64. J. Wertz, D. Everett, and J. Puschell, Space Mission Engineering: The New SMAD. Microcosm Press, 2011.
- 65. S. Kay, Fundamentals of Statistical Signal Processing. Prentice-Hall, 1998, vol. 2.

# REPORT DOCUMENTATION PAGE

Form Approved OMB No. 0704-0188

The public reporting burden for this collection of information is estimated to average 1 hour per response, including the time for reviewing instructions, searching existing data sources, gathering and maintaining the data needed, and completing and reviewing the collection of information. Send comments regarding this burden estimate or any other aspect of this collection of information, including suggestions for reducing this burden to Department of Defense, Washington Headquarters Services, Directorate for Information Operations and Reports (0704–0188), 1215 Jefferson Davis Highway, Suite 1204, Arlington, VA 22202–4302. Respondents should be aware that notwithstanding any other provision of law, no person shall be subject to any penalty for failing to comply with a collection of information if it does not display a currently valid OMB control number. PLEASE DO NOT RETURN YOUR FORM TO THE ABOVE ADDRESS.

1. REPORT DATE (DD-MM-YYYY) 2. REPORT TYPE			3. DATES COVERED (From — To)	
23-03-2017	Master's Thesis		September 2015 - March 2017	
4. TITLE AND SUBTITLE		5a. CONTRACT NUMBER		
An Analysis of Radio-Frequency Geolocation Techniques for Satellite Systems Design		5b. GRANT NUMBER  5c. PROGRAM ELEMENT NUMBER		
6. AUTHOR(S)			5d. PROJECT NUMBER	
Barnes, Daniel R., 2d Lt, USAF			5e. TASK NUMBER  5f. WORK UNIT NUMBER	
7. PERFORMING ORGANIZATION N	AME(S) AND ADDRESS(ES)		8. PERFORMING ORGANIZATION REPORT	
Air Force Institute of Technology Graduate School of Engineering and Management (AFIT/EN) 2950 Hobson Way WPAFB OH 45433-7765			NUMBER  AFIT-ENY-MS-17-M-241	
9. SPONSORING / MONITORING AGENCY NAME(S) AND ADDRESS(ES)			10. SPONSOR/MONITOR'S ACRONYM(S)	
AFRL Space Vehicle Directorate 3350 Aberdeen Avenue SE Kirtland AFB, NM 87117-5776			AFRL/RV  11. SPONSOR/MONITOR'S REPORT NUMBER(S)	
12. DISTRIBUTION / AVAILABILITY	STATEMENT		1	
Distribution Statement A. Approv	ed for public release: Distribution unlimite	d.		

### 13. SUPPLEMENTARY NOTES

This material is declared work of the U.S. Government and is not subject to copyright protection in the United States.

### 14. ABSTRACT

This research 1) evaluates the effectiveness of CubeSat radio-frequency geolocation and 2) analyzes the sensitivity of different RF algorithms to system parameters. A MATLAB simulation is developed to assess geolocation accuracy for variable system designs and techniques (AOA, TDOA, T/FDOA). An unconstrained maximum likelihood estimator (MLE) and three different digital elevation models (DEM) are utilized as the surface of the Earth constraint to improve geologation accuracy. The results presented show the effectiveness of the MLE and DEM techniques, the sensitivity of AOA, TDOA, and T/FDOA algorithms, and the system level performance of a CubeSat geolocation cluster in a 500km circular orbit.

### 15. SUBJECT TERMS

RF Geolocation, AOA, TDOA, FDOA, CubeSats

16. SECURITY CLASSIFICATION OF:				19a. NAME OF RESPONSIBLE PERSON	
a. REPORT	b. ABSTRACT	c. THIS PAGE	ABSTRACT	OF PAGES	Dr. Richard G. Cobb, AFIT/ENY
U	U	U	UU	224	19b. TELEPHONE NUMBER (include area code) (937)785-3636 x.4559; rich.cobb@afit.edu